

UNCLASSIFIED

**ARMED
FORCES
INFORMATION
AGENCY**

Armed Services Technical Information Agency

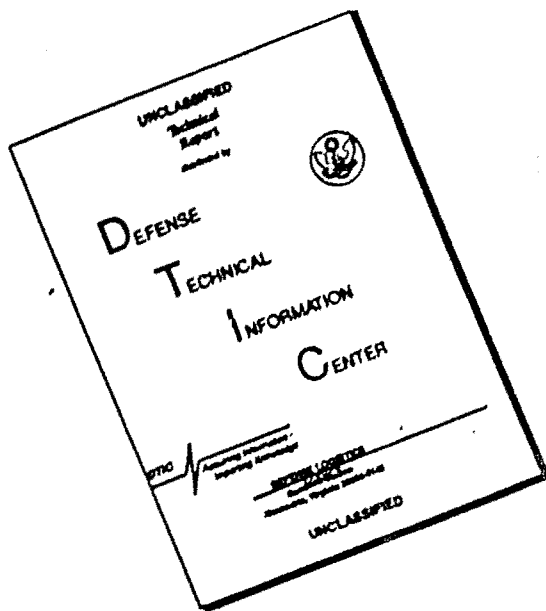
**Reproduced by
DOCUMENT SERVICE CENTER
KNOTT BUILDING, DAYTON, 2, OHIO**

This document is the property of the United States Government. It is furnished for the duration of the contract and shall be returned when no longer required, or upon recall by ASTIA to the following address: Armed Services Technical Information Agency, Document Service Center, Knott Building, Dayton 2, Ohio.

NOTICE: WHEN GOVERNMENT OR OTHER DRAWINGS, SPECIFICATIONS OR OTHER DATA ARE USED FOR ANY PURPOSE OTHER THAN IN CONNECTION WITH A DEFINITELY RELATED GOVERNMENT PROCUREMENT OPERATION, THE U. S. GOVERNMENT THEREBY INCURS NO RESPONSIBILITY, NOR ANY OBLIGATION WHATSOEVER; AND THE FACT THAT THE GOVERNMENT MAY HAVE FORMULATED, FURNISHED, OR IN ANY WAY SUPPLIED THE SAME DRAWINGS, SPECIFICATIONS, OR OTHER DATA IS NOT TO BE REGARDED BY IMPLICATION OR OTHERWISE AS IN ANY MANNER LICENSING THE HOLDER OR ANY OTHER PERSON OR CORPORATION, OR CONVEYING ANY RIGHTS OR PERMISSION TO MANUFACTURE, USE OR SELL ANY PATENTED INVENTION THAT MAY IN ANY WAY BE RELATED THERETO.

UNCLASSIFIED

DISCLAIMER NOTICE



**THIS DOCUMENT IS BEST
QUALITY AVAILABLE. THE COPY
FURNISHED TO DTIC CONTAINED
A SIGNIFICANT NUMBER OF
PAGES WHICH DO NOT
REPRODUCE LEGIBLY.**

OFFICE OF NAVAL RESEARCH
Contract N6onr-27015
Project NR 212-005
In cooperation with
Office Chief of Transportation
Department of the Army

AN AERODYNAMIC ANALYSIS OF A SINGLE-BLADED ROTOR
IN HOVERING AND LOW-SPEED FORWARD FLIGHT
AS DETERMINED FROM SMOKE STUDIES
OF THE VORTICITY DISTRIBUTION IN THE WAKE

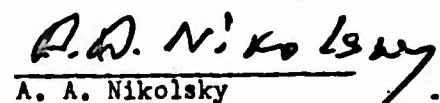
Aeronautical Engineering Department
Report No. 356

September 1956

Prepared by:


Robin B. Gray

Approved by:


A. A. Nikolsky

BIBLIOGRAPHICAL CONTROL SHEET

1. Originating agency and monitoring agency:

O.A. Princeton University, Princeton, New Jersey
M.A. Office of Naval Research, Air Branch (Code 461), Washington 25, D. C.

2. Originating agency report number: Aeronautical Engineering Department Report No. 356

3. Title and classification or title: An Aerodynamic Analysis of a Single-Bladed Rotor in Hovering and Low-Speed Forward Flight as Determined from Smoke Studies of the Vorticity Distribution in the Wake (Unclassified)

4. Personal author: Gray, Robin B.

5. Date of Report: September 1956

6. Pages: 106

7. Illustrative material: 50 figures

8. Prepared for Contract No.: N6onr-27015

9. Prepared for Project No.: NR 212-005

10. Security classification: Unclassified

11. Distribution limitation: Specified by ONR ltr (461:WGR:eew) of 2 January 1957

12. Abstract:

A semi-empirical theory is presented for determining the spanwise aerodynamic loading on a single-bladed helicopter rotor in hovering and low-speed forward flight.

Summary

A semi-empirical theory is presented for determining the spanwise aerodynamic loading on a single-bladed helicopter rotor in hovering and low-speed forward flight. The theoretical portion of the method employs the classical vortex theory for which the position in space of the tip vortex is required for analysis. It is shown that for the hovering case, the position can be theoretically determined to a good degree of accuracy and the results are compared with experiment. However, for the low-speed forward flight case, the necessary parameters for describing the position in space of the tip vortex were determined from a series of smoke studies in which smoke was introduced into this vortex and the resulting flow patterns were photographed. Charts are presented of the results of these studies and a semi-empirical method is developed for calculating the aerodynamic loading. Sample calculations of the component of the induced velocity normal to the tip path plane are made and the spanwise aerodynamic loadings are computed for the hovering flight case and for two blade azimuth positions in forward flight. It is shown that the integrated theoretical loadings in all cases are within one per cent of the measured total thrust and that the shape of the loading curve corresponds, in a general way, with the actual shape.

Introduction

There has been much effort expended on the basic problem of the determination of the variation of the inflow velocity at the blades of a lifting rotor in hovering and in forward flight. A review and discussion of most of this work except for the most recent may be found in either of references 1, 2 or 3. At present, both experimental and theoretical means are still being vigorously employed. For instance references 4 through 9 are indicative of the experimental work that is being carried out. The first four of these references are concerned with the determination of the inflow distributions from experimental blade pressure measurements, and the remaining two are devoted to the direct measurement of the flow field. The NACA works are very interesting and have done much to point out the intricacies of the flow phenomena. References 10 and 11 are indicative of the theoretical approach and they, too, have made notable contributions to the state of the art. The former of these reports adopted a rotor wake configuration in which the vortex distribution consisted of "a straight elliptic cylinder formed by a uniform distribution of an infinite number of vortex rings of infinitesimal strength, lying in planes parallel to the tip-path plane and extending down stream to infinity"; the latter, a wake distribution of concentric elliptic cylinders similarly formed. This type wake pattern should correspond most nearly to a rotor having an angular velocity of rotation and a blade loading such that the inflow velocities are very small in comparison with the blade tangential velocity.

Basically, this same classical vortex concept has been employed in this paper but at the other extreme, namely for a moderately loaded, single-bladed rotor from whose tip is shed a single vortex equal in strength but opposite in sign to the strength of the vortex sheet shed inboard along the blade. As is well known, this fundamental vortex concept of a lifting surface and its trailing wake of vorticity has been applied with varying degrees of success to the problems of the fixed wing aircraft. The primary reason for the early successes of this approach has been due to the fact that the displacement of the position in space of the trailing vortex sheet associated with the flow field induced by the passage of the lifting surface has been small. For the case of the lifting rotor in hovering flight and up to moderate rates of forward flight, this is obviously not true. Neglecting the movement of the vortex system can lead to rather serious errors in the distribution of the blade aerodynamic loading. This makes it necessary that the induced velocities of rotation, contraction, and translation of the vortex lines making up the wake be included in the theory. It is in this area that this paper presents an advancement in the aerodynamic analysis of a rotating rotor blade. Apparently, the reason why this approach has not been taken before is that, as it will be shown, the calculations are quite lengthy and laborious. However the advantages would seem to overshadow this disadvantage in that this approach yields more accurate results, automatically accounts for the tip losses, and yields a periodic flow field.

There does not appear to be much direct background material for this approach. Goldstein, in his famous paper, reference 12, found a solution to the problem of the "potential flow past a body consisting of a finite number of coaxial helicoids of infinite length but finite constant radius moving through a fluid with constant velocity". Lock, in reference 13, applied Goldstein's theory to the practical design of propellers, making also an allowance for tip loss. Reference 14 considers the motion of a helical vortex extending to infinity in both directions and the conditions under which it would be stable. Reference 15 and 16 consider a loaded propeller

with a small number of blades with helical vortices springing from the tips and forming the wake. However, the vortices are assumed to move downstream at the free-stream velocity and the movement of the vortex system due to the induced flow field is neglected. Perhaps the best source is Lamb's Hydrodynamics, reference 17, since chapter VII of this reference provides the starting point for the following analysis.

Symbols

a	local slope of lift curve, per radian
A, B, C	geometric characteristics in wake equation $w = R[A + Be^{-\lambda_1 \Omega r} + Ce^{-\lambda_2 \Omega r}]$
c	local blade chord, ft.
C_L	local blade section lift coefficient
C_T	rotor thrust coefficient, $T \div (\rho \pi \Omega^2 R^4)$
C_X	tip vortex strength coefficient, $\lambda c \div (4\pi R^2 A^2 \Omega)$
E_m	elliptic integral of the second kind
F_m	elliptic integral of the first kind
G	point at which the value of the induced velocity is desired
H	point of tangency that the circle of radius equal to the radius of curvature of the helix makes with the helix
I_1, I_2, I_3	integrals defined by eqs. A-22, A-23, and A-24
J_1, J_2, J_3	defined by eqs. P-12
k	$= 1 - \left(\frac{P_1}{P_2}\right)^2$
K_1, K_2	hovering flight coefficients in vertical displacement equation of tip vortex
K_{my}	forward flight parameters describing the displacement of the tip vortex normal to the tip path plane, (eqs. B-3 through B-9)
K_x	forward flight horizontal motion parameter defined by eq. B-2

L_1	$= K_{1,0^\circ} - K_{1,180^\circ}$
L_2	$= K_{2,0^\circ} - K_{2,180^\circ}$
L_3	$= K_{3,0^\circ} - K_{3,180^\circ}$
M	number of helical vortex filaments used to approximate the vortex sheet in hovering flight
M_1	$= K_{1,0^\circ} - K_{1,270^\circ}$
M_2	$= K_{2,0^\circ} - K_{2,270^\circ}$
M_3	$= K_{3,0^\circ} - K_{3,270^\circ}$
N	number of vortex filaments approximating vortex sheet in forward flight analysis
r	radius of helical tip vortex, ft.
r_b	radial distance from helix axis of any point at which the induced velocities are desired, ft.
r_f	radial position of vortex filaments as defined by eq. A-53, ft.
r_s	radius of point (x_s, y_s) on helix from wake axis (X_h -axis), ft.
R	radius of rotor, ft.
S_1, S_2, S_3	non-dimensional induced velocities associated with tip vortex
S_{1n}, S_{2n}, S_{3n}	non-dimensional induced velocities associated with vortex sheet in forward flight
t	time, measured from t_0 , sec.
t_s	time required for wake to reach steady configuration, sec.
T	rotor thrust, lbs.
u_f	radial velocity component associated with vortex sheet in forward flight, ft/sec.
u_l	radial induced velocity associated with lifting line, ft/sec.
u_t	radial induced velocity associated with tip vortex, ft/sec.

u_x, u_y, u_z	induced velocity components parallel to $X'Y'Z'$ -axes respectively, ft/sec.
u_t	tangential induced velocity component associated with vortex sheet in forward flight, ft/sec.
v	velocity along flight path, ft/sec.
u_r	induced velocity component along Z -axis that is associated with the vortex sheet in forward flight, ft/sec.
u_l	axial induced velocity associated with lifting line, ft/sec.
u_t	axial induced velocity associated with tip vortex, ft/sec.
\bar{x}	non-dimensional blade station, r_b/R
\bar{x}_m	non-dimensional blade station at which vortex filament is shed in hovering flight
\bar{x}_n	non-dimensional blade station at which vortex filament is shed in forward flight
x, y, z	coordinates of point, H , at which the value of the induced velocity is desired, ft.
x', y', z'	coordinates of centerline of helical tip vortex, ft.
$X'Y'Z'$	axes fixed to center of curvature of the helix: X -axis lies along the radius of curvature of the helix; Y -axis lies in plane of the circle determined by radius of curvature
X_h, Y_h, Z_h	axes fixed in space with Z_h -axis lying along the helix axis. Point (x, y, z) lies on X_h -axis
z_f	axial displacement of vortex filaments as defined by eq. A-52, ft.
z_0	axial distance of any point at which the induced velocities are desired from helix axis in hovering flight, ft.
Z	displacement of point on tip vortex normal to tip path plane, ft.
α	in hovering flight, the azimuth angle of any point at which the induced velocities are desired from the X_h -axis, radians
α	in forward flight, the angle of attack of the tip path plane, positive below tip path plane, degrees
α_s	shaft angle of attack, positive for forward flight velocity component in negative Z -direction (i.e. upward), degrees

β	$= \frac{1}{2}(\pi - \xi - \gamma)$
β_0	blade coning angle, degrees
δ	in hovering flight, the angle variable of integration measured from X -axis in plane of circle, radians
γ	in forward flight, the azimuth position of a point on the helix from downwind, positive in direction of rotation, $0 \leq \gamma \leq 2\pi$, radians
δ	the angle between X -axis and the point (x, y, z) measured about the Z -axis, radians
ϵ	radius of core of tip vortex, ft.
θ	local collective blade pitch angle, radians unless otherwise noted
θ_0	blade root collective pitch angle, radians unless otherwise noted
κ	strength of tip vortex, sq.ft./sec.
λ_1, λ_2	exponents in wake equation $r = R [A + Be^{-\lambda_1 \Omega t} + ce^{-\lambda_2 \Omega t}]$
$\bar{\lambda}_\infty$	$= \omega_{T_\infty} / \Omega R A$
μ_y	advance ratio along flight path, $V/\Omega R$
ν	in hovering flight, the angle about wake axis (X_h -axis) between X -axis and X_h -axis, radians
ψ	in forward flight, the azimuth position from the blade feathering axis of the point in space at which the value of the inflow velocity is desired, positive in direction opposite to blade rotation, radians
$\xi \eta \zeta$	axes fixed to point (x, y, z) with ξ -axis lying along X_h -axis and η -axis lying in $X_h Y_h$ -plane
ρ	mass density of air, slugs per cubic ft.
R_0	radius of curvature of helix, ft.
\bar{P}^2	$= x^2 + y^2$
\bar{P}'^2	$= x'^2 + y'^2$
P	distance between the point (x, y, z) and a general point (x', y', z') on the helical vortex, ft.

P_1	least distance from point (x, y, z) to the tangent circle, ft.
P_2	greatest distance from the point (x, y, z) to the tangent circle, ft.
ϕ	pitch angle of central curve of helical vortex, radians
χ	wake skew angle, angle lying in the longitudinal plane between the no-feathering axis and the extended trailing edge of the wake, radians
τ	azimuth position of blade feathering axis, measured in direction of rotation from downwind, $0 \leq \tau \leq 2\pi$, radians
τ'	azimuth position of a point on the helical tip vortex measured from blade feathering axis, positive in direction opposite to blade rotation, radians
ω_L	angular induced velocity associated with lifting line, radians/sec.
ω_T	angular induced velocity associated with tip vortex, radians/sec.
$\bar{\omega}_\infty$	$= \omega_{T_\infty} / \Omega$
Ω	angular velocity of blade, radians/sec.

Subscripts:

f	vortex filament
L	lifting line
T	tip vortex
∞	ultimate wake

Part A. An Isolated Rotor in Hovering Flight

Introduction

In this section a theoretical method of determining the blade spanwise aerodynamic loading of a single-bladed helicopter rotor which is based on the classical vortex theory will be developed and the results compared with the experimental data of reference 18. It was shown in that reference that the integral equations derived therein for the inflow velocities had to be evaluated by either numerical or graphical means. Since this report was published, a method has been devised for evaluating these integrals in a piece-wise manner. Then the inflow velocity at any point is the sum of these piece-wise integrals taken over the extent of the vortex.

Theoretical Analysis

As before, a single-bladed rotor will be considered in which the blade is replaced by a lifting line of the proper circulation distribution. The wake will be considered to be composed of two parts: a single vortex, shed from the blade tip, of finite size and of strength equal to the maximum value of the lifting line circulation; and a vortex sheet, shed inboard along the blade from the point of maximum lifting line circulation, and equal in strength to the change in circulation of the lifting line along the span. This wake configuration is modeled after the observed configuration as obtained from smoke studies as shown in figure 1.

In the analysis, it will be assumed that the rotor has been hovering for a sufficient length of time, t_0 , so that the wake has reached its steady state configuration. In addition, the blade will be taken to be perfectly rigid with a zero coning angle.

It will be assumed that the presence of the vortex sheet in the flow field has negligible effect on the motion of the tip vortex. Then, specifying the vortex strength coefficient, completely specifies non-dimensionally the entire flow field associated with the helical tip vortex. For according to Lamb, reference 17, the induced velocity components associated with an isolated re-entrant vortex-filament situated in an infinite mass of incompressible fluid which is at rest at infinity are

$$u_x = \frac{\alpha}{4\pi} \int \left\{ \frac{dx'}{dy} (z - z') - \frac{dz'}{dy} (y - y') \right\} \frac{dy}{P^3} \quad (A-1-a)$$

$$u_y = \frac{\alpha}{4\pi} \int \left\{ \frac{dz'}{dx} (x - x') - \frac{dx'}{dy} (z - z') \right\} \frac{dx}{P^3} \quad (A-1-b)$$

$$u_z = \frac{\alpha}{4\pi} \int \left\{ \frac{dx'}{dy} (y - y') - \frac{dy'}{dx} (x - x') \right\} \frac{dy}{P^3} \quad (A-1-c)$$

where the integration must be performed over the entire length of the vortex and $\Psi(x, y, z)$ defines the point in the flow field under consideration (points within the vortex core are excluded from the analysis unless it is stated otherwise), $\Psi(x', y', z')$, a variable point on the helix, P (rho)

the distance between the two points, and κ (kappa) the strength of the vortex. Now, in order to utilize these equations, it is necessary to know the position in space of the vortex. From some smoke studies which were discussed in reference 18, it was observed that the radius of the helical vortex as a function of its azimuth position from the blade may be closely approximated by the relationship

$$r = R [A + Be^{-\lambda_1 \Omega t} + Ce^{-\lambda_2 \Omega t}] \quad (A-2)$$

and that the tangent of the helix angle, ϕ , may also be closely approximated by

$$\tan \phi = \frac{K_1 R}{r} \quad 0 \leq \Omega t < 2\pi \quad (A-3-a)$$

$$= \frac{K_2 R}{r} \quad 2\pi < \Omega t \quad (A-3-b)$$

where A, B, C, K_1 , K_2 , λ_1 , and λ_2 are the geometric parameters to be determined.

In reference 18, the integral equations were developed for the motion of the helical vortex; for the general case of any point in the flow field; and for the special case of the feathering axis of a rigid blade with no built in coning. As pointed out before, these integrals, in the form in which they were given, could only be evaluated by numerical or graphical means. For this reason, it was not feasible to try to theoretically evaluate all the geometric parameters. It was shown that K_2 could be evaluated in the ultimate wake and that A and C could be very easily evaluated from simple momentum considerations, so that

$$A = .707 + \frac{\epsilon}{R} \quad (A-4)$$

$$C = .293 - \frac{\epsilon}{R} \quad (A-5)$$

where ϵ is the radius of the cross-section of the tip vortex. The remaining parameters were determined from a series of smoke studies. The result was a semi-empirical theory for calculating the spanwise aerodynamic loading of a single-bladed rotor.

However, if the helix is considered to be made up of circular arcs of radius equal to the radius of curvature of the helix and lying in the plane defined by the tangent line and the principal normal to a point on the helix, then the resulting integral equations may be integrated over an interval $\pm A\gamma$ and then summed over the entire length of the helix.

In figure 2, the x_h , y_h , z_h axes are fixed in space with the z_h axis lying along the helix axis. The $\xi\eta\zeta$ axes are fixed to the point under consideration, S , with the ξ axis lying along the x_h axis, and the η axis lying in the $x_h y_h$ plane. The $x y z$ axes are fixed to the dashed circle which is tangent to the helix at the point H . The radius of this circle is equal to the radius of curvature of the helix at that point. The x axis intersects the z_h axis and intersects the circle and helix at the point of tangency, and is

parallel to the $x_1 y_1$ plane. The z_1 axis makes an angle ϕ (the helix pitch angle) with the x_1^2 plane. The angle ν is measured from the x_1 axis to the projection of the X axis in the $x_1 y_1$ plane. The angle γ is measured from the X axis in the plane of the circle.

Then the coordinates of the point G in the Xy^2 coordinates are, for r and γ_0 measured from the helix axis,

$$x = r \tan^2 \phi + r_0 \cos \nu \quad (A-6-a)$$

$$y = -Z \sin \phi - r_0 \cos \phi \sin \nu \quad (A-6-b)$$

$$z = -Z \cos \phi + r_0 \sin \phi \sin \nu \quad (A-6-c)$$

WHERE $r = R [A + B e^{-\lambda_1(\nu+\Omega t)} \sin(\nu+\Omega t) + C e^{-\lambda_2(\nu+\Omega t)}]$ $(A-7)$

$$r_0 = R [A + B e^{-\lambda_1 \Omega t} \sin \Omega t + C e^{-\lambda_2 \Omega t}] \quad (A-8)$$

$$Z = K_1 R \nu \quad 0 \leq \nu + \Omega t < 2\pi; \Omega t < 2\pi \quad (A-9-a)$$

$$= K_1 R (2\pi - \Omega t) + K_1 R (\nu - 2\pi + \Omega t) \quad \nu + \Omega t > 2\pi; \Omega t < 2\pi \quad (A-9-b)$$

$$= K_2 R \nu \quad \nu + \Omega t > 2\pi; \Omega t > 2\pi \quad (A-9-c)$$

$$= K_2 R (2\pi - \Omega t) + K_2 R (\nu - 2\pi + \Omega t) \quad 0 \leq \nu + \Omega t < 2\pi; \Omega t > 2\pi \quad (A-9-d)$$

The coordinates of the segment of the helical vortex, now considered to be a circular arc are

$$x' = r \sec^2 \phi \cos \gamma \quad (A-10-a)$$

$$y' = r \sec^2 \phi \sin \gamma \quad (A-10-b)$$

$$z' = 0 \quad (A-10-c)$$

In these latter equations, terms of second order in λ_1 AND λ_2 have been neglected so that the radius of curvature, ρ_0 , of the helix is given approximately by

$$\rho_0 \approx r \sec^2 \phi \quad (A-11)$$

For $r = \text{constant}$, this relationship is exact.

The other terms in equations (A-1) are as follows,

$$\frac{dx'}{ds} = -r \sec^2 \phi \sin \gamma + \left(\frac{dr}{ds} \sec^2 \phi + 2r \tan \phi \sec^2 \phi \frac{d\phi}{ds} \right) \cos \gamma \quad (A-12-a)$$

$$\frac{dy'}{ds} = r \sec^2 \phi \cos \gamma + \left(\frac{dr}{ds} \sec^2 \phi + 2r \tan \phi \sec^2 \phi \frac{d\phi}{ds} \right) \sin \gamma \quad (A-12-b)$$

$$\frac{dz'}{ds} = 0 \quad (A-12-c)$$

$$(x-x') = r \tan^2 \phi + r_0 \cos \nu - r \sec^2 \phi \cos \gamma \quad (A-13-a)$$

$$(y-y') = -Z \sin \phi - r_0 \cos \phi \sin \nu - r \sec^2 \phi \sin \gamma \quad (A-13-b)$$

$$(z-z') = -Z \cos \phi + r_0 \sin \phi \sin \nu \quad (A-13-c)$$

$$P^2 = (x-x')^2 + (y-y')^2 + (z-z')^2 + \epsilon^2$$

Let $\bar{\rho}^2 = x^2 + y^2$

$$\bar{\rho}'^2 = x'^2 + y'^2$$

then $P^2 = (z-z')^2 + \bar{\rho}^2 + \bar{\rho}'^2 - 2 \bar{\rho} \bar{\rho}' \cos(\delta + \gamma) + \epsilon^2$

where

$$\delta = \arctan \left[\frac{Z \sin \phi + r_0 \cos \phi \sin \nu}{r \tan^2 \phi + r_0 \cos \nu} \right]$$

For $\gamma = -\delta$

$$P_1^2 = (z - z')^2 + (\bar{e} - \bar{e}')^2 + \epsilon^2$$

which is the least distance from the point G to the circle H , and for

$$\gamma = \pi - \delta$$

$$P_2^2 = (z - z')^2 + (\bar{e} + \bar{e}')^2 + \epsilon^2$$

which is the greatest distance from the point G to the circle H .
In terms of P_1 and P_2 ,

$$P^2 = \frac{1}{2}(P_1^2 + P_2^2) - \frac{1}{2}(P_1^2 - P_2^2) \cos(\delta + \gamma)$$

Let $\delta + \gamma = \pi - 2\beta$

then $\cos(\delta + \gamma) = 2 \sin^2 \beta - 1$

and $P^2 = P_2^2 (1 - k^2 \sin^2 \beta)$

where $k^2 = 1 - (P_1^2/P_2^2)$ (A-14)

Hence $P^3 = P_2^3 (1 - k^2 \sin^2 \beta)^{\frac{3}{2}}$ (A-15)

and

$$\begin{aligned} P_1^2 &= r^2 + r_o^2 + Z^2 + 2r^2 \tan^2 \phi \sec^2 \phi (1 - \cos \nu) \\ &\quad + 2rr_o [\tan^2 \phi \cos \nu - \sec \phi (\sin^2 \nu + \sec \phi \cos^2 \nu)] \\ &\quad - 2rZ \tan \phi \sec \phi \sin \nu + \epsilon^2 \end{aligned} \quad (A-16)$$

$$\begin{aligned} P_2^2 &= r^2 + r_o^2 + Z^2 + 2r^2 \tan^2 \phi \sec^2 \phi (1 + \cos \nu) \\ &\quad + 2rr_o [\tan^2 \phi \cos \nu + \sec \phi (\sin^2 \nu + \sec \phi \cos^2 \nu)] \\ &\quad + 2rZ \tan \phi \sec \phi \sin \nu + \epsilon^2 \end{aligned} \quad (A-17)$$

The incremental velocity components at the point G associated with the circular arc vortex segment are found by substituting the above expressions into equations (A-1).

$$\Delta u_x = \frac{x}{4\pi} \int_{\gamma_1}^{\gamma_2} \left\{ \left[r \sec^2 \varphi \cos \delta + \left(\frac{dr}{d\delta} \sec^2 \varphi + 2r \tan \varphi \sec^2 \varphi \frac{d\varphi}{d\delta} \right) \sin \delta \right] \left[-\frac{r}{2} \cos \varphi + r_0 \sin \varphi \sin \nu \right] \right\} \frac{d\delta}{P^2} \quad (A-18-a)$$

$$\Delta u_y = \frac{x}{4\pi} \int_{\gamma_1}^{\gamma_2} \left\{ \left[r \sec^2 \varphi \cos \delta - \left(\frac{dr}{d\delta} \sec^2 \varphi + 2r \tan \varphi \sec^2 \varphi \frac{d\varphi}{d\delta} \right) \cos \delta \right] \left[-\frac{r}{2} \cos \varphi + r_0 \sin \varphi \sin \nu \right] \right\} \frac{d\delta}{P^2} \quad (A-18-b)$$

$$\begin{aligned} \Delta u_z &= \frac{x}{4\pi} \int_{\gamma_1}^{\gamma_2} \left\{ \left[r \sec^2 \varphi \cos \delta - \left(\frac{dr}{d\delta} \sec^2 \varphi + 2r \tan \varphi \sec^2 \varphi \frac{d\varphi}{d\delta} \right) \sin \delta \right] \left[r \tan^2 \varphi + r_0 \cos \nu \right. \right. \\ &\quad \left. \left. - r \sec^2 \varphi \cos \delta \right] + \left[r \sec^2 \varphi \sin \delta - \left(\frac{dr}{d\delta} \sec^2 \varphi + 2r \tan \varphi \sec^2 \varphi \frac{d\varphi}{d\delta} \right) \cos \delta \right] \left[\frac{r}{2} \sin \varphi \right. \\ &\quad \left. \left. + r_0 \cos \varphi \sin \nu + r \sec^2 \varphi \sin \delta \right] \right\} \frac{d\delta}{P^2} \end{aligned} \quad (A-18-c)$$

The expressions for the incremental radial velocity, Δu_r , rotational velocity, $\Delta \omega_r$, and axial velocity, Δu_θ , are

$$\Delta u_r = \Delta u_x \cos \nu + (\Delta u_y \sin \varphi - \Delta u_z \cos \varphi) \sin \nu \quad (A-19-a)$$

$$r_0 \Delta \omega_r = (\Delta u_y \cos \varphi - \Delta u_z \sin \varphi) \cos \nu + \Delta u_x \sin \nu \quad (A-19-b)$$

$$\Delta u_\theta = \Delta u_x \cos \varphi + \Delta u_y \sin \varphi \quad (A-19-c)$$

Substituting equations (A-18) into (A-19) yields

$$\begin{aligned} \Delta u_r &= \frac{x}{2\pi} \int_{\gamma_1}^{\gamma_2} \left\{ \left[r_0 \left[\sec \varphi \cos \nu \cos \delta + (1 + \tan^2 \varphi) \sin \nu \sin \delta \right] + \frac{r}{2} \cos^2 \varphi dR \left[(1 + \tan^2 \varphi) \sin \nu \cos \delta \right. \right. \right. \\ &\quad \left. \left. - \sec \varphi \cos \nu \sin \delta \right] + r^2 \tan^3 \varphi \sec \varphi \sin \nu \cos \delta - r dR \tan \varphi \sec \varphi \sin \delta \right] \left[2 \sin^2 \beta - 1 \right] \\ &\quad + \left\{ r_0 \left[-(1 + \tan^2 \varphi) \sin \nu \cos \delta + \sec \varphi \cos \nu \sin \delta \right] \right. \\ &\quad \left. + \frac{r}{2} dR \cos^2 \varphi \left[(1 + \tan^2 \varphi) \sin \nu \sin \delta + \sec \varphi \cos \nu \cos \delta \right] + r^2 \sec \varphi \tan^3 \varphi \sin \nu \sin \delta \right. \\ &\quad \left. + r dR \sin \tan^3 \varphi \sin \nu \cos \delta \right] \cdot 2 \sin \beta \cos \beta - r^2 \tan \varphi \sec^3 \varphi \sin \nu \right\} \frac{d\delta}{(1 - k^2 \sin^2 \beta)^{3/2}} \quad (A-20-a) \end{aligned}$$

$$\begin{aligned}
 r_0 \Delta \omega_T = & \frac{x}{2\pi} \int_{\beta_1}^{\beta_2} \left\{ r \left[\sec \varphi \sin v \cos \delta - (1 + \tan^2 \varphi) \cos v \sin \delta \right] - Z \cos^2 \varphi dR \right\} \sec \varphi \sin v \sin \delta \\
 & + (1 + \tan^2 \varphi) \cos v \cos \delta \Big] - rr_0 \tan \varphi \sec \varphi \cos \delta + r dR \sec \varphi \tan^2 \varphi \cos v \cos \delta \\
 & + r_0 dR \sin \varphi \sin \delta - r^2 \sec \varphi \tan^3 \varphi \cos v \cos \delta \Big\} [2 \sin^2 \beta - 1] \\
 & + \left\{ r \left[\sec \varphi \sin v \sin \delta + (1 + \tan^2 \varphi) \cos v \cos \delta \right] + Z \cos^2 \varphi dR \right\} \sec \varphi \sin v \cos \delta \\
 & - (1 + \tan^2 \varphi) \cos v \sin \delta \Big] - rr_0 \tan \varphi \sec \varphi \sin \delta - r dR \sec \varphi \tan^3 \varphi \cos v \cos \delta \\
 & - r_0 dR \sin \varphi \cos \delta - r^2 \sec \varphi \tan^3 \varphi \cos v \sin \delta \Big\} \cdot 2 \sin \beta \cos \beta \\
 & + r^2 \sec^2 \varphi \tan \varphi \cos v \Bigg| \frac{d\beta}{P_2^3 (1 - k^2 \sin^2 \beta)^{3/2}} \quad (A-20-b)
 \end{aligned}$$

$$\begin{aligned}
 \Delta \omega_T = & \frac{x}{2\pi} \int_{\beta_1}^{\beta_2} \left\{ rr_0 \left[\sec \varphi \cos v \cos \delta + (1 + \tan^2 \varphi) \sin v \sin \delta \right] \right. \\
 & \left. + r_0 \cos^2 \varphi dR \sin v \cos \delta (\sec \varphi - \sec \varphi \cos \delta) + r^2 \sec \varphi \tan^2 \varphi \cos \delta - r dR \sec \varphi \tan^3 \varphi \sin \delta \right\} [2 \sin^2 \beta - 1] \\
 & + \left\{ rr_0 \left[\sec \varphi \cos v \sin \delta - (1 + \tan^2 \varphi) \sin v \cos \delta \right] \right. \\
 & \left. + r_0 dR \cos^2 \varphi [(\sec \varphi - \sec \varphi \cos \delta) \sin v \cos \delta + \sec \varphi \cos v \cos \delta] + r^2 \sec \varphi \tan^2 \varphi \sin \delta \right. \\
 & \left. + r dR \cos \varphi \tan^3 \varphi \cos \delta \right\} \cdot 2 \sin \beta \cos \beta - r^2 \sec^2 \varphi \Bigg| \frac{d\beta}{P_2^3 (1 - k^2 \sin^2 \beta)^{3/2}} \quad (A-20-c)
 \end{aligned}$$

where $dR = -2 \left(\frac{dr}{d\beta} \sec^2 \varphi + r \tan \varphi \sec^2 \varphi \frac{d\varphi}{d\beta} \right)$

these last three equations are still rigorously correct for graphical integration.

Considering the ultimate wake; $\frac{dr}{d\beta} = \frac{d\varphi}{d\beta} = 0$; $Z = RA \sin \beta$; and $r = r_0 = RA$.
The expressions for the velocity components become

$$\begin{aligned}
 \Delta u_T = & \frac{x}{2\pi} \cdot \frac{R^2 A^2}{P_2^3} \tan \varphi \int_{\beta_1}^{\beta_2} \left\{ v \left[\sec \varphi \cos v \cos \delta + (1 + \tan^2 \varphi) \sin v \sin \delta \right] \right. \\
 & \left. + \sec \varphi \tan^2 \varphi \sin v \cos \delta \right\} [2 \sin^2 \beta - 1] \\
 & + 2 \left\{ v \left[(1 + \tan^2 \varphi) \sin v \cos \delta + \sec \varphi \cos v \sin \delta \right] \right. \\
 & \left. + \sec \varphi \tan^2 \varphi \sin v \sin \delta \right\} \sin \beta \cos \beta - \sec^2 \varphi \sin v \Bigg| \frac{d\beta}{(1 - k^2 \sin^2 \beta)^{3/2}} \quad (A-21-a)
 \end{aligned}$$

$$\Delta\omega_r = \frac{x}{2\pi} \cdot \frac{RA}{P^2} \tan\phi \int_{\beta_1}^{\beta_2} \left[\begin{aligned} & \left\{ 2 \left[\sec\phi \sin\psi \cos\delta - (1 + \tan^2\phi) \cos\psi \sin\delta - \sec\phi \cos\delta \right. \right. \\ & \left. \left. - \sec\phi \tan^2\phi \cos\psi \cos\delta \right] \right\} [2 \sin^2\beta - 1] \\ & + 2 \left\{ 2 \left[\sec\phi \sin\psi \sin\delta + (1 + \tan^2\phi) \cos\psi \cos\delta \right] - \sec\phi \sin\delta \right. \\ & \left. - \sec\phi \tan^2\phi \cos\psi \sin\delta \right\} \sin\beta \cos\beta + \sec^2\phi \cos\psi \end{aligned} \right] \frac{d\beta}{(1 - k_m^2 \sin^2\beta)^{3/2}} \quad (A-21-b)$$

$$\Delta\omega_r = \frac{x}{2\pi} \cdot \frac{R^2 A^2}{P^2} \int_{\beta_1}^{\beta_2} \left[\begin{aligned} & \left\{ \sec\phi \cos\psi \cos\delta + (1 + \tan^2\phi) \sin\psi \sin\delta \right. \\ & \left. + \sec\phi \tan^2\phi \cos\delta \right\} [2 \sin^2\beta - 1] \\ & + 2 \left\{ \sec\phi \cos\psi \sin\delta - (1 + \tan^2\phi) \sin\psi \cos\delta + \sec\phi \tan^2\phi \sin\delta \right\} \sin\beta \cos\beta \\ & - \sec^3\phi \end{aligned} \right] \frac{d\beta}{(1 - k_m^2 \sin^2\beta)^{3/2}} \quad (A-21-c)$$

Integrating the three kinds of integrals appearing in the above equations yields

$$I_{1m} = \int_{\beta_{1m}}^{\beta_{2m}} \frac{d\beta_m}{[1 - k_m^2 \sin^2\beta_m]^{3/2}} = \frac{1}{1 - k_m^2} \left\{ E_m - k_m^2 \left[\frac{\sin\beta_{2m} \cos\beta_{2m}}{(1 - k_m^2 \sin^2\beta_{2m})^{1/2}} - \frac{\sin\beta_{1m} \cos\beta_{1m}}{(1 - k_m^2 \sin^2\beta_{1m})^{1/2}} \right] \right\} \quad (A-22)$$

$$I_{2m} = \int_{\beta_{1m}}^{\beta_{2m}} \frac{\sin^2\beta_m d\beta_m}{[1 - k_m^2 \sin^2\beta_m]^{3/2}} = \frac{1}{k_m^2} \left\{ I_{1m} - F_m \right\} \quad (A-23)$$

$$I_{3m} = \int_{\beta_{1m}}^{\beta_{2m}} \frac{\sin\beta_m \cos\beta_m d\beta_m}{[1 - k_m^2 \sin^2\beta_m]^{3/2}} = \frac{1}{k_m^2} \left\{ \frac{1}{(1 - k_m^2 \sin^2\beta_{2m})^{1/2}} - \frac{1}{(1 - k_m^2 \sin^2\beta_{1m})^{1/2}} \right\} \quad (A-24)$$

where $F_m = F(k_m, \beta_{2m}) - F(k_m, \beta_{1m})$

$$E_m = E(k_m, \beta_{2m}) - E(k_m, \beta_{1m})$$

and are the elliptic integrals of the first and second kinds respectively.

Taking $\nu = 0; \pm \frac{\pi}{2}; \pm \pi; \pm \frac{3\pi}{2}; \dots; \pm \frac{(2m-1)\pi}{2}; \dots$

and $\gamma_2 = \arctan \frac{\frac{\pi}{2} \tan \varphi + \cos \varphi}{\tan^2 \varphi + \cos^2 \frac{\pi}{2}}$; $\gamma_1 = \arctan \frac{-\frac{\pi}{2} \tan \varphi + \cos \varphi}{\tan^2 \varphi + \cos^2 \frac{\pi}{2}}$

or $\beta_{2m} = \frac{1}{2}(\pi - \delta_m - \gamma_2) \quad ; \quad \beta_{1m} = \frac{1}{2}(\pi - \delta_m - \gamma_1)$

the induced velocity components at the point on the helix under consideration in the ultimate wake may be expressed as

$$\begin{aligned} \frac{4\pi RA U_{\infty}}{x} &= 2 \tan \varphi \sum_{n=0}^{\infty} \left(\frac{RA}{P_{2m}} \right)^3 \left[\left\{ \frac{n\pi}{2} \left[\sec \varphi \cos \frac{n\pi}{2} \cos \delta_m + (1 + \tan^2 \varphi) \sin \frac{n\pi}{2} \sin \delta_m \right] \right. \right. \\ &\quad \left. \left. + \sec \varphi \tan^2 \varphi \sin \frac{n\pi}{2} \cos \delta_m \right\} [2I_{2m} - I_{1m}] \right. \\ &\quad + 2 \left\{ \frac{n\pi}{2} \left[(1 + \tan^2 \varphi) \sin \frac{n\pi}{2} \cos \delta_m + \sec \varphi \cos \frac{n\pi}{2} \sin \delta_m \right] \right. \\ &\quad \left. \left. + \sec \varphi \tan^2 \varphi \sin \frac{n\pi}{2} \sin \delta_m \right\} \cdot I_{3m} \right. \\ &\quad \left. - \sec^3 \varphi \sin \frac{n\pi}{2} \cdot I_{1m} \right] \end{aligned} \quad (A-25-a)$$

which equals zero by inspection since

$$\Delta U_{m\infty} = -\Delta U_{-m\infty} \quad \text{AND} \quad \Delta U_{0\infty} = 0$$

$$\begin{aligned}
 S_1 = \frac{4\pi R^2 A^2 \omega_{T\infty}}{\chi} &= 2 \tan \varphi \sum_{m=0}^{\infty} \left(\frac{RA}{P_2} \right)^3 \left[\left\{ \frac{m\pi}{2} \left[\sec \varphi \sin \frac{m\pi}{2} \cos \delta_m - (1 + \tan^2 \varphi) \cos \frac{m\pi}{2} \sin \delta_m \right] \right. \right. \\
 &\quad - \sec \varphi \cos \delta_m - \sec \varphi \tan^2 \varphi \cos \frac{m\pi}{2} \cos \delta_m \Big] [2I_{2m} - I_{1m}] \\
 &\quad + 2 \left\{ \frac{m\pi}{2} \left[\sec \varphi \sin \frac{m\pi}{2} \sin \delta_m + (1 + \tan^2 \varphi) \cos \frac{m\pi}{2} \cos \delta_m \right] \right. \\
 &\quad - \sec \varphi \sin \delta_m - \sec \varphi \tan^2 \varphi \cos \frac{m\pi}{2} \sin \delta_m \Big\} I_{3m} \\
 &\quad \left. \left. + \sec^3 \varphi \cos \frac{m\pi}{2} \cdot I_{1m} \right] \right] \quad (A-25-b)
 \end{aligned}$$

$$\begin{aligned}
 S_2 = \frac{4\pi RA \omega_{T\infty}}{\chi} &= 2 \sum_{m=0}^{\infty} \left(\frac{RA}{P_2} \right)^3 \left[\left\{ \sec \varphi \cos \frac{m\pi}{2} \cos \delta_m \right. \right. \\
 &\quad + (1 + \tan^2 \varphi) \sin \frac{m\pi}{2} \sin \delta_m + \sec \varphi \tan^2 \varphi \cos \delta_m \Big] [2I_{2m} - I_{1m}] \\
 &\quad + 2 \left\{ + \sec \varphi \cos \frac{m\pi}{2} \sin \delta_m - (1 + \tan^2 \varphi) \sin \frac{m\pi}{2} \cos \delta_m \right. \\
 &\quad \left. \left. + \sec \varphi \tan^2 \varphi \sin \delta_m \right\} I_{3m} - \sec^3 \varphi \cdot I_{1m} \right] \quad (A-25-c)
 \end{aligned}$$

where $P_{I_0}^2 = \epsilon^2$

$$P_{I_0}^2 = 4R^2 A^2 \sec^4 \varphi$$

However $\tan \varphi = \frac{K_2}{A} = \frac{\omega_{T\infty}}{RA(\omega_{\infty} + \Omega)} = \frac{\bar{\lambda}_{\infty}}{1 + \bar{\omega}_{\infty}}$

where $\bar{\lambda}_{\infty} = \frac{M_{T\infty}}{\Omega RA}$ AND $\bar{\omega}_{T\infty} = \frac{\omega_{T\infty}}{\Omega}$

Then $S_1 = \frac{4\pi R^2 A^2 \Omega \bar{\omega}_{T\infty}}{\chi}$

$$S_2 = \frac{4\pi R^2 A^2 \Omega \bar{\lambda}_{\infty}}{\chi}$$

Let $C_x = \frac{\chi}{4\pi R^2 A^2 \Omega}$

$$\text{Then } \frac{1}{C_x} = \left(\frac{A}{K_2}\right) S_2 - S_1, \quad (A-26)$$

$$\bar{\lambda}_\infty = C_x S_2 = \frac{S_2}{\left(\frac{A}{K_2}\right) S_2 - S_1} \quad (A-27)$$

$$\bar{\omega}_{T_\infty} = C_x S_1 = \frac{S_1}{\left(\frac{A}{K_2}\right) S_2 - S_1} \quad (A-28)$$

Of the seven geometric parameters, A , B , C , λ_1 , λ_2 , K_1 and K_2 , three have now been determined; i.e. A , C , and K_2 . In order to determine the others, it is necessary to make the assumption that

$$\frac{dr}{d\gamma} = \frac{d\phi}{d\gamma} = 0$$

(which is acceptable for helicopter rotors because ϕ is usually small), since it is required that P_{sum} be independent of γ in order that the integration over the arc may be performed. Then for the same intervals of ν and δ as before, the incremental induced velocity equations become as follows

$$\begin{aligned} \Delta u_T &= \frac{x}{2\pi} \int_{\beta_1}^{\beta_2} \left\{ r_L^2 [\sec \phi \cos \nu \cos \delta + \sec^2 \phi \sin \nu \cos \delta] + r^2 \sec \phi \tan^2 \phi \sin \nu \cos \delta \right\} [2 \sin^2 \beta - 1] \\ &\quad + \left\{ r_L^2 [\sec \phi \cos \nu \cos \delta - \sec^2 \phi \sin \nu \cos \delta] + r^2 \sec \phi \tan^2 \phi \sin \nu \cos \delta \right\} 2 \sin \beta \cos \beta \\ &\quad - r^2 \sec^2 \phi \tan \phi \sin \nu \left[1 - k^2 \sin^2 \beta \right]^{-\frac{3}{2}} \frac{d\beta}{P_i^2} \end{aligned} \quad (A-29-a)$$

$$\begin{aligned} r_0 \Delta u_T &= \frac{x}{2\pi} \int_{\beta_1}^{\beta_2} \left\{ r_L^2 [-\sec \nu \cos \delta - \sec^2 \phi \cos \nu \cos \delta] - r r_0 \tan \phi \sec \phi \cos \delta \right. \\ &\quad \left. - r^2 \sec \phi \tan^2 \phi \cos \nu \cos \delta \right\} [2 \sin^2 \beta - 1] + \left\{ r_L^2 [\sec \phi \cos \nu \cos \delta + \sec^2 \phi \cos \nu \cos \delta] \right. \\ &\quad \left. - r r_0 \sec \phi \tan \phi \cos \delta - r^2 \sec \phi \tan^2 \phi \cos \nu \cos \delta \right\} 2 \sin \beta \cos \beta \\ &\quad + r^2 \sec^2 \phi \tan \phi \cos \nu \left[1 - k^2 \sin^2 \beta \right]^{-\frac{3}{2}} \frac{d\beta}{P_i^2} \end{aligned} \quad (A-29-b)$$

$$\begin{aligned} \Delta u_T &= \frac{x}{2\pi} \int_{\beta_1}^{\beta_2} \left\{ r r_0 [\sec \phi \cos \nu \cos \delta + \sec^2 \phi \sin \nu \cos \delta] + r^2 \sec \phi \tan^2 \phi \cos \delta \right\} [2 \sin^2 \beta - 1] \\ &\quad + \left\{ r r_0 [\sec \phi \cos \nu \cos \delta - \sec^2 \phi \sin \nu \cos \delta] + r^2 \sec \phi \tan^2 \phi \sin \delta \right\} 2 \sin \beta \cos \beta \\ &\quad - r^2 \sec^2 \phi \left[1 - k^2 \sin^2 \beta \right]^{-\frac{3}{2}} \frac{d\beta}{P_i^2} \end{aligned} \quad (A-29-c)$$

The calculated contribution of the lifting line on the motion of the tip vortex must now be included. The accuracy of the distribution of the circulation along the blade span should not be too critical, so that in this instance, it will be assumed to be triangular, i.e. $\Delta x_x = -\bar{x} x$. Then in a similar manner as before

$$x_L = r \cos \psi$$

$$y_L = r \sin \psi$$

$$z_L = z$$

$$x'_L = r'$$

$$y'_L = 0$$

$$z'_L = 0$$

$$\frac{dx'_L}{dr'} = 1$$

$$P_i^2 = r^2 + z^2 + \epsilon^2 - 2rr' \cos \psi + r'^2$$

$$u_L = - \frac{x \sin \psi}{4\pi R} \cdot z \cdot \int_0^R \frac{r' dr'}{P_i^3}$$

$$rw_L = - \frac{x \cos \psi}{4\pi R} \cdot z \cdot \int_0^R \frac{r' dr'}{P_i^3}$$

$$w_L = \frac{x r \sin \psi}{4\pi R} \int_0^R \frac{r' dr'}{P_i^3}$$

Performing the integrations yields the velocity component expression as follows

$$u_L = - \frac{x \sin \psi}{4\pi R} \cdot z \cdot I_L \quad (A-30-a)$$

$$rw_L = - \frac{x \cos \psi}{4\pi R} \cdot z \cdot I_L \quad (A-30-b)$$

$$w_L = \frac{x r \sin \psi}{4\pi R} \cdot I_L \quad (A-30-c)$$

where

$$I_1 = \frac{(r^2 + Z^2 + \epsilon^2)^{\frac{1}{2}}}{[r^2 \sin^2 \nu + Z^2 + \epsilon^2]} + \frac{\tau R \cos \nu - [r^2 + Z^2 + \epsilon^2]}{[r^2 + Z^2 + \epsilon^2][r^2 + R^2 + Z^2 - 2\tau R \cos \nu + \epsilon^2]^{\frac{1}{2}}}$$

However, the smoke studies show that

$$u = \dot{r}_o = -\Omega R [B e^{-\lambda_1 \Omega t} (\lambda_1 \sin \Omega t - \cos \Omega t) + C \lambda_2 e^{-\lambda_2 \Omega t}] \quad (A-31-a)$$

$$\omega = \omega \quad (A-31-b)$$

$$\mu r = (\Omega + \omega_m) R K_1 \quad \Omega t < 2\pi \quad (A-31-c)$$

$$= (\Omega + \omega_m) R K_2 \quad \Omega t > 2\pi \quad (A-31-d)$$

Now, since equations (A-31) include the effects associated with both the lifting line and the tip vortex itself,

$$u = \sum \Delta u_T + u_L \quad (A-32-a)$$

$$\omega = \sum \Delta \omega_T + \omega_L \quad (A-32-b)$$

$$\mu r = \sum \Delta \mu_T + \mu_L \quad (A-32-c)$$

Substituting equations (A-29), (A-30), and (A-31) into the preceding expressions, yields three equations in the four unknowns B , λ_1 , λ_2 , and K_1 . Remembering that

$$\tan \phi_o = \frac{K_1 R}{r_o} = \frac{\mu r}{r_o(\Omega + \omega)} \quad (A-33)$$

yields the required fourth expression. Theoretically, these four expressions may

be solved simultaneously for the four remaining geometric parameters, but practically it is quite impossible, at least by ordinary computation procedure, i.e. desk calculators. However, by making some additional assumptions, it is possible to determine reasonably accurately, two of the remaining four parameters.

Since the smoke studies indicate that θ is of the order of 5% and λ_1 of the order of 1, the term $Be^{-\lambda_1 \Omega t} \sin 2t$ may be neglected, certainly for $\Omega t > 3\pi/2$. Thus, it will be assumed that

$$r = R [A + Ce^{-\lambda_2(v+\Omega t)}] \quad (A-34)$$

and

$$u = -\Omega RC\lambda_2 e^{-\lambda_2(v+\Omega t)} \quad (A-35)$$

It is obvious from the radial velocity equation, that a radial velocity arises at a point on the helix entirely according to the proximity of that point to the end of the helix. It is also obvious that, in general, the further away the point under consideration is from a particular vortex segment the less is the latter's associated incremental velocity. Thus, if the point under consideration is taken to be about one rotor radius beneath the rotor, then any reasonable variation of the position in space of the first coil under the rotor from its actual position should cause small error in the calculation. From the smoke studies, it appears that a reasonable approximation is to take

$$K_1 = \frac{1}{2} K_2 \quad (A-36)$$

Now it becomes feasible to determine the exponent λ_2 by considering the radial velocity equation at a point on the helix at a distance of approximately one rotor radius below the rotor and an azimuth angle from the blade of some multiple of 2π , the latter depending upon the value of K_2 , so that

$$\Omega t = 2\pi n$$

where n is the nearest whole number to $(\frac{1}{2\pi K_2} + \frac{1}{2})$.

From equations (A-29-a) and (A-35)

$$\begin{aligned} -\frac{1}{2C_x} \cdot \frac{C}{A} \lambda_2 e^{-2\pi n \lambda_2} &= \sum_{m=1}^{\infty} \left(\frac{RA}{R_m} \right)^3 \left\{ \left[\frac{r^2}{R_m^2} \cdot \frac{m\pi}{2} \tan(\sec \varphi \cos \frac{m\pi}{2} \omega s_m + \sec^2 \varphi \sin \frac{m\pi}{2} \omega s_m) \right. \right. \\ &\quad \left. \left. + \left(\frac{r}{RA} \right)^2 \sec^2 \varphi \sin \frac{m\pi}{2} \omega s_m \right] (2J_{2m} - J_{1m}) \right\} \end{aligned}$$

$$\begin{aligned}
& + 2 \left[\frac{(r)}{(RA)} \right]^2 \frac{\pi}{2} \tan \varphi (\sec \varphi \cos \frac{\pi}{2} \sin \delta_n - \sec^2 \varphi \sin \frac{\pi}{2} \cos \delta_n) \\
& + \left(\frac{r}{RA} \right)^2 \sec \varphi \tan^3 \varphi \sin \frac{\pi}{2} \sin \delta_n \left[I_{3,n} - \left(\frac{r}{RA} \right)^2 \sec^3 \varphi \tan \varphi \sin \frac{\pi}{2} \cdot I_{1,n} \right] \\
& + \sum_{-4a+1}^{-4a+3} \left(\frac{RA}{P_{2,-4}} \right)^3 \left[\frac{(r)}{(RA)} \right]^2 \pi \left(1-a + \frac{n}{4} \right) \tan \varphi (\sec \varphi \cos \frac{\pi}{2} \cos \delta_n + \sec^2 \varphi \sin \frac{\pi}{2} \sin \delta_n) \\
& + \left(\frac{r}{RA} \right)^2 \sec \varphi \tan^3 \varphi \sin \frac{\pi}{2} \cos \delta_n \left[(2I_{2,n} - I_{1,n}) \right] \\
& + 2 \left[\frac{(r)}{(RA)} \right]^2 \pi \left(1-a + \frac{n}{4} \right) \tan \varphi (\sec \varphi \cos \frac{\pi}{2} \sin \delta_n - \sec^2 \varphi \sin \frac{\pi}{2} \cos \delta_n) \\
& + \left(\frac{r}{RA} \right)^2 \sec \varphi \tan^3 \varphi \sin \frac{\pi}{2} \sin \delta_n \left[I_{3,n} - \left(\frac{r}{RA} \right)^2 \sec^3 \varphi \tan \varphi \sin \frac{\pi}{2} \cdot I_{1,n} \right] \\
& + \left(\frac{RA}{P_{2,-4(a-1)}} \right)^3 \left\{ \left(\frac{r}{RA} \right)^2 \cdot 2\pi (1-a) \tan \varphi \sec \varphi \cos \delta_{-4(a-1)}^+ \cdot (2I_{2,-4(a-1)}^+ - I_{1,-4(a-1)}^+) \right. \\
& \quad \left. + \left(\frac{r}{RA} \right)^2 \cdot 2\pi (1-a) \tan \varphi \sec \varphi \sin \delta_{-4(a-1)}^+ \cdot 2I_{3,-4(a-1)}^+ \right\} \\
& + \left(\frac{RA}{P_{2,-4(a-1)}} \right)^3 \left\{ \left(\frac{r}{RA} \right)^2 \cdot 2\pi (1-a) \tan \varphi \sec \varphi \cos \delta_{-4(a-1)}^- \cdot (2I_{2,-4(a-1)}^- - I_{1,-4(a-1)}^-) \right. \\
& \quad \left. + \left(\frac{r}{RA} \right)^2 \cdot 2\pi (1-a) \tan \varphi \sec \varphi \sin \delta_{-4(a-1)}^- \cdot 2I_{3,-4(a-1)}^- \right\} \\
& + \left(\frac{RA}{P_{2,-4a}} \right)^3 \left\{ \left(\frac{r}{RA} \right)^2 \cdot \pi (1-2a) \tan \varphi \sec \varphi \cos \delta_{-4a}^- \cdot (2I_{2,-4a}^- - I_{1,-4a}^-) \right. \\
& \quad \left. + \left(\frac{r}{RA} \right)^2 \pi (1-2a) \tan \varphi \sec \varphi \sin \delta_{-4a}^- \cdot 2I_{3,-4a}^- \right\} \tag{A-37}
\end{aligned}$$

where the subscripts define the limits of integration as follows

$$-4(a-1)^+ : \quad \beta_2 = \frac{1}{2} [\pi - \delta - \gamma_2] ; \quad \beta_1 = \frac{1}{2} (\pi - \delta)$$

$$-4(a-1)^- : \quad \beta_2 = \frac{1}{2} (\pi - \delta) ; \quad \beta_1 = \frac{1}{2} (\pi - \delta - \gamma_1)$$

$$-4a : \quad \beta_2 = \frac{1}{2} (\pi - \delta - \gamma_2) ; \quad \beta_1 = \frac{1}{2} (\pi - \delta)$$

$$\gamma_2 = \arctan \frac{\frac{\pi}{4} \tan \varphi \sin \varphi + \cos \varphi \sin \frac{\pi}{4}}{\tan^2 \varphi + \cos^2 \frac{\pi}{4}}$$

$$\gamma_1 = \arctan \frac{-\frac{\pi}{4} \tan \varphi \sin \varphi + \cos \varphi \sin \frac{\pi}{4}}{\tan^2 \varphi + \cos^2 \frac{\pi}{4}}$$

and where it must be remembered that

$$r_0 = R \left[A + C e^{-2\pi \lambda_2} \right]$$

$$r = R \left[A + C e^{-2\pi \lambda_2 \left(\frac{\pi}{T} + a \right)} \right]$$

$$\tan \varphi = \frac{K_1 R}{r} \approx \frac{K_1 R}{2r}$$

$$= \frac{K_1 R}{r}$$

$$-4(a-1) > m > -4a$$

$$\infty > n > -4(a-1)$$

$$Z = \left(1 - a + \frac{m}{q} \right) \pi K_1 R \quad 1 > a + \frac{m}{q} > 0$$

$$= \frac{m\pi}{2} K_1 R \quad a + \frac{m}{q} > 1$$

and k , P_{1m} , and P_{2m} are defined by equations (A-14), (A-16) and (A-17 respectively. This equation must now be solved by assuming various values of λ_2 until the left side of the equation equals the right side.

Once λ_2 has been determined, it is possible to obtain a similar solution for K_1 . Again neglecting the $B e^{-\lambda_2 (y+2\pi)}$ term, and for $\Delta t = \pi$, equations (A-31-c) and A-29-c) yield

$$\begin{aligned} \frac{1+\bar{\omega}_m}{2C_x} \cdot \frac{K_1}{A} = & \left(\frac{RA}{P_{2m}} \right)^3 \left\{ \left[\frac{r}{RA} \cdot \frac{r_0}{RA} \sec \varphi_i \cos \delta_{2-} - \left(\frac{r}{RA} \right)^2 \sec \varphi_i \tan^2 \varphi_i \cos \delta_{2-} \right] (2I_{2-} - I_{1-}) \right. \\ & \left. + 2 \left[\frac{rr_0}{(RA)^2} \sec \varphi_i \sin \delta_{2-} - \left(\frac{r}{RA} \right)^2 \sec \varphi_i \tan^2 \varphi_i \sin \delta_{2-} \right] \cdot I_{3-} + \left(\frac{r}{RA} \right)^3 \sec^3 \varphi_i I_{1-} \right\} \\ & + \sum_{n=1}^l \left(\frac{RA}{P_{2m}} \right)^3 \left\{ \left[\frac{rr_0}{(RA)^2} \left(\sec \varphi_i \cos \frac{m\pi}{2} \cos \delta_m + \sec^2 \varphi_i \sin \frac{m\pi}{2} \sin \delta_m \right) \right. \right. \\ & \left. + \left(\frac{r}{RA} \right)^2 \sec \varphi_i \tan^2 \varphi_i \cos \delta_m \right] (2I_{2n} - I_{1n}) + 2 \left[\frac{rr_0}{(RA)^2} \left(\sec \varphi_i \cos \frac{m\pi}{2} \sin \delta_m \right. \right. \\ & \left. - \sec^2 \varphi_i \sin \frac{m\pi}{2} \cos \delta_m \right) + \left(\frac{r}{RA} \right)^2 \sec \varphi_i \tan^2 \varphi_i \sin \delta_m \left. \right] I_{3m} - \left(\frac{r}{RA} \right)^3 \sec^3 \varphi_i I_{1m} \right\} \\ & + \left(\frac{RA}{P_{2m}} \right)^3 \left\{ \left[\frac{-rr_0}{(RA)^2} \sec \varphi_i \cos \delta_{2+} + \left(\frac{r}{RA} \right)^2 \sec \varphi_i \tan^2 \varphi_i \cos \delta_{2+} \right] (2I_{2+} - I_{1+}) \right. \\ & \left. + 2 \left[\frac{rr_0}{(RA)^2} \sec \varphi_i \sin \delta_{2+} + \left(\frac{r}{RA} \right)^2 \sec \varphi_i \tan^2 \varphi_i \sin \delta_{2+} \right] \cdot I_{3+} - \left(\frac{r}{RA} \right)^3 \sec^3 \varphi_i I_{1+} \right\} \\ & + \left(\frac{RA}{P_{2m}} \right)^3 \left\{ \left[\frac{-rr_0}{(RA)^2} \sec \varphi_i \cos \delta_{2+} + \left(\frac{r}{RA} \right)^2 \sec \varphi_i \tan^2 \varphi_i \cos \delta_{2+} \right] (2I_{2+} - I_{1+}) \right. \\ & \left. + 2 \left[\frac{-rr_0}{(RA)^2} \sec \varphi_i \sin \delta_{2+} + \left(\frac{r}{RA} \right)^2 \sec \varphi_i \tan^2 \varphi_i \sin \delta_{2+} \right] \cdot I_{3+} - \left(\frac{r}{RA} \right)^3 \sec^3 \varphi_i I_{1+} \right\} \end{aligned}$$

$$\begin{aligned}
 & + \sum_{n=1}^{\infty} \left(\frac{RA}{P_{2n}} \right)^3 \left\{ \left[\frac{rr_0}{(RA)^2} \left(\sec \varphi_2 \cos \frac{m\pi}{2} \cos \delta_n + \sec^2 \varphi_2 \sin \frac{m\pi}{2} \sin \delta_n \right) \right. \right. \\
 & \quad + \left(\frac{r}{RA} \right)^2 \sec \varphi_2 \tan^2 \varphi_2 \cos \delta_n \Big] (2I_{2n} - I_{1n}) + 2 \left[\frac{rr_0}{(RA)^2} \left(\sec \varphi_2 \cos \frac{m\pi}{2} \sin \delta_n \right. \right. \\
 & \quad - \left. \sec^2 \varphi_2 \sin \frac{m\pi}{2} \cos \delta_n \right) + \left(\frac{r}{RA} \right)^2 \sec \varphi_2 \tan^2 \varphi_2 \sin \delta_n \Big] \cdot I_{3n} \\
 & \quad \left. \left. - \left(\frac{r}{RA} \right)^2 \sec^3 \varphi_2 \cdot I_{1n} \right] \right\} \quad (A-38)
 \end{aligned}$$

and from equation (A-29-b)

$$\begin{aligned}
& \frac{\bar{\omega}}{2C_{x_2}} \cdot \frac{T_0}{RA} = \left(\frac{RA}{P_{x_2}} \right)^3 \left\{ \left[\left(\frac{r}{RA} \right)^2 \cdot \pi \sec^2 \varphi_i \tan \varphi_i \sin \delta_2 - \frac{r^2 T_0}{(RA)^2} \tan \varphi_i \sec \varphi_i \cos \delta_2 \right. \right. \\
& + \left(\frac{r}{RA} \right)^2 \sec \varphi_i \tan^3 \varphi_i \cos \delta_2 \Big] (2I_{2_{-2}} - I_{1_{-2}}) + \left[\left(\frac{r}{RA} \right)^2 \pi \sec^2 \varphi_i \tan \varphi_i \cos \delta_2 \right. \\
& - \left. \left. \frac{r^2 T_0}{(RA)^2} \sec \varphi_i \tan \varphi_i \sin \delta_2 + \left(\frac{r}{RA} \right)^2 \sec \varphi_i \tan^3 \varphi_i \sin \delta_2 \right] \cdot 2I_{2_2} - \left(\frac{r}{RA} \right)^2 \sec^2 \varphi_i \tan \varphi_i \cdot I_{1_{-2}} \Big\} \\
& + \sum_{n=1}^1 \left(\frac{RA}{P_{x_2}} \right)^3 \left\{ \left(\frac{r}{RA} \right)^2 \cdot \frac{\pi^2}{2} \tan \varphi_i (\sec \varphi_i \sin \frac{n\pi}{2} \cos \delta_n - \sec^2 \varphi_i \cos \frac{n\pi}{2} \sin \delta_n) - \frac{r^2 T_0}{(RA)^2} \tan \varphi_i \sec \varphi_i \cos \delta_n \right. \\
& - \left(\frac{r}{RA} \right)^2 \sec \varphi_i \tan^3 \varphi_i \cos \frac{n\pi}{2} \cos \delta_n \Big] (2I_{2_n} - I_{1_n}) + 2 \left[\left(\frac{r}{RA} \right)^2 \cdot \frac{\pi^2}{2} \tan \varphi_i (\sec \varphi_i \sin \frac{n\pi}{2} \sin \delta_n \right. \\
& + \sec^2 \varphi_i \cos \frac{n\pi}{2} \cos \delta_n) - \frac{r^2 T_0}{(RA)^2} \sec \varphi_i \tan \varphi_i \sin \delta_n - \left(\frac{r}{RA} \right)^2 \sec \varphi_i \tan^3 \varphi_i \cos \frac{n\pi}{2} \sin \delta_n \Big] \cdot I_{1_n} \\
& + \left. \left(\frac{r}{RA} \right)^2 \sec^2 \varphi_i \tan \varphi_i \cos \frac{n\pi}{2} \cdot I_{1_n} \right\} \\
& + \left(\frac{RA}{P_{x_2}} \right)^3 \left\{ \left(\frac{r}{RA} \right)^2 \cdot \pi \sec^2 \varphi_i \tan \varphi_i \sin \delta_2 - \frac{r^2 T_0}{(RA)^2} \tan \varphi_i \sec \varphi_i \cos \delta_2 - \right. \\
& + \left(\frac{r}{RA} \right)^2 \sec \varphi_i \tan^3 \varphi_i \cos \delta_2 \Big] (2I_{2_{-2}} - I_{1_{-2}}) + \left[- \left(\frac{r}{RA} \right)^2 \cdot \pi \sec^2 \varphi_i \tan \varphi_i \cos \delta_2 - \right. \\
& - \left. \left. \frac{r^2 T_0}{(RA)^2} \sec \varphi_i \tan \varphi_i \sin \delta_2 + \left(\frac{r}{RA} \right)^2 \sec \varphi_i \tan^3 \varphi_i \sin \delta_2 \right] \cdot 2I_{2_2} - \left(\frac{r}{RA} \right)^2 \sec^2 \varphi_i \tan \varphi_i \cdot I_{1_{-2}} \right\} \\
& + \left(\frac{RA}{P_{x_2}} \right)^3 \left\{ \left[\left(\frac{r}{RA} \right)^2 \cdot \pi \sec^2 \varphi_i \tan \varphi_i \sin \delta_{2_0} - \frac{r^2 T_0}{(RA)^2} \sec \varphi_i \tan \varphi_i \cos \delta_{2_0} \right. \right. \\
& + \left(\frac{r}{RA} \right)^2 \sec \varphi_i \tan^3 \varphi_i \cos \delta_{2_0} \Big] (2I_{2_{-2}} - I_{1_{-2}}) + 2 \left[\left(\frac{r}{RA} \right)^2 \cdot \pi \sec^2 \varphi_i \tan \varphi_i \cos \delta_{2_0} + \right. \\
& - \left. \left. \frac{r^2 T_0}{(RA)^2} \sec \varphi_i \tan \varphi_i \sin \delta_{2_0} + \left(\frac{r}{RA} \right)^2 \sec \varphi_i \tan^3 \varphi_i \sin \delta_{2_0} \right] \cdot I_{2_2} - \left(\frac{r}{RA} \right)^2 \sec^2 \varphi_i \tan \varphi_i \cdot I_{1_{-2}} \right\} \\
& + \sum_{n=1}^{\infty} \left(\frac{RA}{P_{x_2}} \right)^3 \left\{ \left[\left(\frac{r}{RA} \right)^2 \cdot \pi \left(\tan \varphi_i + \frac{n-2}{2} \tan \varphi_i \right) (\sec \varphi_i \sin \frac{n\pi}{2} \cos \delta_n - \sec^2 \varphi_i \cos \frac{n\pi}{2} \sin \delta_n) \right. \right. \\
& - \left. \left. \frac{r^2 T_0}{(RA)^2} \sec \varphi_i \tan \varphi_i \cos \delta_n - \left(\frac{r}{RA} \right)^2 \sec \varphi_i \tan^3 \varphi_i \cos \frac{n\pi}{2} \cos \delta_n \right] (2I_{2_n} - I_{1_n}) \right. \\
& + \left[\left(\frac{r}{RA} \right)^2 \cdot \pi \left(\tan \varphi_i + \frac{n-2}{2} \tan \varphi_i \right) (\sec \varphi_i \sin \frac{n\pi}{2} \sin \delta_n + \sec^2 \varphi_i \cos \frac{n\pi}{2} \cos \delta_n) \right. \\
& - \left. \left. \frac{r^2 T_0}{(RA)^2} \sec^2 \varphi_i \tan \varphi_i \sin \delta_n - \left(\frac{r}{RA} \right)^2 \sec \varphi_i \tan^3 \varphi_i \cos \frac{n\pi}{2} \sin \delta_n \right] \cdot 2I_{2_2} \right. \\
& + \left. \left. \left(\frac{r}{RA} \right)^2 \sec^2 \varphi_i \tan \varphi_i \cos \frac{n\pi}{2} \cdot I_{1_n} \right\} \right. \quad (A-39)
\end{aligned}$$

where the subscripts define the limits of integration as follows

$$-2 : \quad \beta_2 = \frac{1}{2}(\pi - \delta - \gamma_2) \quad ; \quad \beta_1 = \frac{1}{2}(\pi - \delta)$$

$$2^- : \quad \beta_2 = \frac{1}{2}(\pi - \delta) \quad ; \quad \beta_1 = \frac{1}{2}(\pi - \delta - \gamma_1)$$

$$2^+ : \quad \beta_2 = \frac{1}{2}(\pi - \delta - \gamma_2) \quad ; \quad \beta_1 = \frac{1}{2}(\pi - \delta)$$

and where

$$r_0 = R [A + C e^{-\pi \lambda_2}]$$

$$r = R [A + C e^{-\pi \lambda_2 (\frac{m}{2} + 1)}]$$

$$\tan \varphi_1 = \frac{K_1 R}{r} \quad 2 > m \geq -2$$

$$\tan \varphi_2 = \frac{K_2 R}{r} \quad \infty > m > 2$$

$$Z = \frac{m\pi}{2} K_1 R \quad 2 > m \geq -2$$

$$= \pi K_1 R + \pi K_2 R (\frac{m}{2} - \pi) \quad \infty > m > 2$$

and k , P_{1m} , and P_{2m} are as before. Solving equation (A-38) by trial and error yields the desired value of K_1 . Thus it has been shown that by neglecting the $\delta e^{-\lambda_2(m+1)}$ term, it is possible to evaluate the remaining geometric parameters. Now the equations will be developed for the inflow velocity associated with the tip vortex and the lifting line at any point in the flow field.

Using the same coordinate system as before, it will be assumed that the x_h axis, ξ axis and blade feathering axis (or lifting line) are coincident. Let r be the radial distance from the helix axis; α , the azimuth angle from the x_h axis; and z_e , the axial distance from the $x_h y_h$ plane of the point under consideration. Then the coordinates of the point with respect to the XYE axes are

$$x = r \tan^2 \varphi + r_b \cos(\nu - \alpha) \quad (A-40-a)$$

$$\gamma = -Z_0 \sin \varphi - r_b \cos \varphi \sin(\nu - \alpha) \quad (A-40-b)$$

$$z = -Z_0 \cos \varphi + r_b \sin \varphi \sin(\nu - \alpha) \quad (A-40-c)$$

where

$$r = R [A + C e^{-\lambda_2 \nu}] \quad (A-41)$$

$$Z_0 = K_1 R \nu - z_0 \quad 0 \leq \nu < 2\pi \quad (A-42-a)$$

$$= 2\pi K_1 R + K_2 R (\nu - 2\pi) - z_0 \quad 2\pi < \nu < \infty \quad (A-42-b)$$

As before the coordinates of the circular arc segment of the helical vortex are

$$x' = r \sec^2 \varphi \cos \gamma \quad (A-43-a)$$

$$y' = r \sec^2 \varphi \sin \gamma \quad (A-43-b)$$

$$z' = 0 \quad (A-43-c)$$

Following the same procedure as before yields the incremental inflow velocity equations.

$$\begin{aligned} \Delta U_T = \frac{x}{2\pi} \int_{\rho_1}^{\rho_2} & \left\{ \left[r^2 Z_0^2 [\sec \varphi \cos(\nu - \alpha) \cos \delta + \sec^2 \varphi \sin(\nu - \alpha) \sin \delta] + r^2 \sec \varphi \tan^2 \varphi \sin(\nu - \alpha) \cos \delta \right] [2 \sin^2 \beta - 1] \right. \\ & + \left. \left[r^2 Z_0^2 [\sec \varphi \cos(\nu - \alpha) \sin \delta - \sec^2 \varphi \sin(\nu - \alpha) \cos \delta] + r^2 \sec \varphi \tan^2 \varphi \sin(\nu - \alpha) \sin \delta \right] \cdot 2 \sin \beta \cos \beta \right. \\ & \left. - r^2 \sec^3 \varphi \tan \varphi \sin(\nu - \alpha) \right] (1 - k^2 \sin^2 \beta)^{-\frac{1}{2}} \cdot \frac{d\beta}{P_s^3} \quad (A-44-a) \right. \end{aligned}$$

$$r_b \Delta \omega_r = \frac{x}{2\pi} \int_{\beta_1}^{\beta_2} \left[r^2 L_0 [\sec \varphi \sin(\nu - \alpha) \cos \delta - \sec^2 \varphi \cos(\nu - \alpha) \sin \delta] - r r_b \tan \varphi \sec \varphi \cos \delta \right. \\ \left. - r^2 \sec \varphi \tan^3 \varphi \cos(\nu - \alpha) \cos \delta \right] (2 \sin^2 \beta - 1) + \left[r^2 L_0 [\sec \varphi \sin(\nu - \alpha) \cos \delta + \sec^2 \varphi \cos(\nu - \alpha) \sin \delta] \right. \\ \left. - r r_b \sec \varphi \tan \varphi \sin \delta - r^2 \sec \varphi \tan^3 \varphi \cos(\nu - \alpha) \cos \delta \right] \cdot 2 \sin \beta \cos \beta \\ + r^2 \sec^3 \varphi \tan \varphi \cos(\nu - \alpha) \left(1 - k^2 \sin^2 \beta \right)^{-\frac{1}{2}} \cdot \frac{d\beta}{P_1^3} \quad (A-44-b)$$

$$\Delta \mu_r = \frac{x}{2\pi} \int_{\beta_1}^{\beta_2} \left\{ r r_b [\sec \varphi \cos(\nu - \alpha) \cos \delta + \sec^2 \varphi \sin(\nu - \alpha) \cos \delta] + r^2 \sec \varphi \tan^2 \varphi \cos \delta \right\} (2 \sin^2 \beta - 1) \\ + \left\{ r r_b [\sec \varphi \cos(\nu - \alpha) \sin \delta - \sec^2 \varphi \sin(\nu - \alpha) \cos \delta] + r^2 \sec \varphi \tan^2 \varphi \sin \delta \right\} \cdot 2 \sin \beta \cos \beta \\ - r^2 \sec^3 \varphi \left(1 - k^2 \sin^2 \beta \right)^{-\frac{1}{2}} \cdot \frac{d\beta}{P_2^3} \quad (A-44-c)$$

where $\beta_2 = \frac{1}{2}(\pi - \delta - \gamma_2) \quad ; \quad \beta_1 = \frac{1}{2}(\pi - \delta - \gamma_1) \quad (A-45-a)$

$$\delta = \arctan \frac{Z_0 \sin \varphi + r_b \cos \varphi \sin(\nu - \alpha)}{r \tan^2 \varphi + r_b \cos(\nu - \alpha)} \quad (A-45-b)$$

$$P_1^2 = r^2 + r_b^2 + L_0^2 + 2r^2 \tan^2 \varphi \sec^2 \varphi [1 - \cos(\nu - \alpha)] \\ + 2r r_b \left\{ \tan^2 \varphi \cos(\nu - \alpha) - \sec \varphi [\sin^2(\nu - \alpha) + \sec \varphi \cos^2(\nu - \alpha)] \right\} \\ - 2r L_0 \tan \varphi \sec \varphi \sin(\nu - \alpha) + \epsilon^2 \quad (A-46)$$

$$P_2^2 = r^2 + r_b^2 + L_0^2 + 2r^2 \tan^2 \varphi \sec^2 \varphi [1 + \cos(\nu - \alpha)] \\ + 2r r_b \left\{ \tan^2 \varphi \cos(\nu - \alpha) + \sec \varphi [\sin^2(\nu - \alpha) + \sec \varphi \cos^2(\nu - \alpha)] \right\} \\ + 2r L_0 \tan \varphi \sec \varphi \sin(\nu - \alpha) + \epsilon^2 \quad (A-47)$$

and the remaining terms are as defined previously. It should be noted that in some cases it is possible for P_1 to be larger than P_2 . In these cases, the analysis leading up to equation (A-14) must be done over so that the condition $0 \leq k^2 \leq 1$ remains true. The procedure is obvious and therefore will be omitted here. Performing the integrations over the same intervals as before yields

$$\begin{aligned}
\frac{u_T}{2C_x} = & \left(\frac{RA}{P_{2_0}}\right)^3 \left\{ -\frac{rz_0}{(RA)^2} [\sec \varphi_i \cos \alpha \cos \delta_0 - \sec^2 \varphi_i \sin \alpha \sin \delta_0] - \left(\frac{r}{RA}\right)^2 \sec \varphi_i \tan^3 \varphi_i \sin \alpha \cos \delta_0 \right\} (2I_{2_0} - I_{1_0}) \\
& + 2 \left\{ -\frac{rz_0}{(RA)^2} [\sec \varphi_i \cos \alpha \sin \delta_0 + \sec^2 \varphi_i \sin \alpha \cos \delta_0] - \left(\frac{r}{RA}\right)^2 \sec \varphi_i \tan^3 \varphi_i \sin \alpha \sin \delta_0 \right\} \cdot I_{3_0} \\
& + \left(\frac{r}{RA}\right)^2 \sec^3 \varphi_i \tan \varphi_i \sin \alpha \cdot I_{1_0} \\
& + \sum_{n=1}^{\infty} \left(\frac{RA}{P_{2_m}}\right)^3 \left[\frac{r}{RA} \left[\frac{K_1}{A} \cdot \frac{m\pi}{2} - \frac{z_0}{RA} \right] \left[\sec \varphi_i \cos \left(\frac{m\pi}{2} - \alpha\right) \cos \delta_m + \sec^2 \varphi_i \sin \left(\frac{m\pi}{2} - \alpha\right) \sin \delta_m \right] \right. \\
& \quad \left. + \left(\frac{r}{RA}\right)^2 \sec \varphi_i \tan^3 \varphi_i \sin \left(\frac{m\pi}{2} - \alpha\right) \cos \delta_m \right\} (2I_{2_m} - I_{1_m}) \\
& + 2 \left\{ \frac{r}{RA} \left[\frac{K_1}{A} \cdot \frac{m\pi}{2} - \frac{z_0}{RA} \right] \left[\sec \varphi_i \cos \left(\frac{m\pi}{2} - \alpha\right) \sin \delta_m - \sec^2 \varphi_i \sin \left(\frac{m\pi}{2} - \alpha\right) \cos \delta_m \right] \right. \\
& \quad \left. + \left(\frac{r}{RA}\right)^2 \sec \varphi_i \tan^3 \varphi_i \sin \left(\frac{m\pi}{2} - \alpha\right) \sin \delta_m \right\} \cdot I_{3_m} \\
& - \left(\frac{r}{RA}\right)^2 \sec^3 \varphi_i \tan \varphi_i \sin \left(\frac{m\pi}{2} - \alpha\right) \cdot I_{1_m} \\
& + \left(\frac{RA}{P_{2_{4^-}}}\right)^3 \left[\frac{r}{RA} \left[\frac{K_1}{A} \cdot 2\pi - \frac{z_0}{RA} \right] \left[\sec \varphi_i \cos \alpha \cos \delta_{4^-} - \sec^2 \varphi_i \sin \alpha \sin \delta_{4^-} \right] \right. \\
& \quad \left. - \left(\frac{r}{RA}\right)^2 \sec \varphi_i \tan^3 \varphi_i \sin \alpha \cos \delta_{4^-} \right\} (2I_{2_{4^-}} - I_{1_{4^-}}) \\
& + 2 \left\{ \frac{r}{RA} \left[\frac{K_1}{A} \cdot 2\pi - \frac{z_0}{RA} \right] \left[\sec \varphi_i \cos \alpha \sin \delta_{4^-} + \sec^2 \varphi_i \sin \alpha \cos \delta_{4^-} \right] \right. \\
& \quad \left. - \left(\frac{r}{RA}\right)^2 \sec \varphi_i \tan^3 \varphi_i \sin \alpha \sin \delta_{4^-} \right\} \cdot I_{3_{4^-}} + \left(\frac{r}{RA}\right)^2 \sec^3 \varphi_i \tan \varphi_i \sin \alpha \cdot I_{1_{4^-}} \\
& + \left(\frac{RA}{P_{2_{4^+}}}\right)^3 \left[\frac{r}{RA} \left[\frac{K_1}{A} \cdot 2\pi - \frac{z_0}{RA} \right] \left[\sec \varphi_i \cos \alpha \cos \delta_{4^+} - \sec^2 \varphi_i \sin \alpha \sin \delta_{4^+} \right] \right. \\
& \quad \left. - \left(\frac{r}{RA}\right)^2 \sec \varphi_i \tan^3 \varphi_i \sin \alpha \cos \delta_{4^+} \right\} (2I_{2_{4^+}} - I_{1_{4^+}}) \\
& + 2 \left\{ \frac{r}{RA} \left[\frac{K_1}{A} \cdot 2\pi - \frac{z_0}{RA} \right] \left[\sec \varphi_i \cos \alpha \sin \delta_{4^+} + \sec^2 \varphi_i \sin \alpha \cos \delta_{4^+} \right] \right. \\
& \quad \left. - \left(\frac{r}{RA}\right)^2 \sec \varphi_i \tan^3 \varphi_i \sin \alpha \sin \delta_{4^+} \right\} \cdot I_{3_{4^+}} + \left(\frac{r}{RA}\right)^2 \sec^3 \varphi_i \tan \varphi_i \sin \alpha \cdot I_{1_{4^+}} \\
& + \sum_{n=1}^{\infty} \left(\frac{RA}{P_{2_m}}\right)^2 \left[\frac{r}{RA} \left[2\pi \frac{K_1}{A} + \frac{K_2}{A} \left(\frac{m\pi}{2} - 2\pi \right) - \frac{z_0}{RA} \right] \left[\sec \varphi_i \cos \left(\frac{m\pi}{2} - \alpha\right) \cos \delta_m + \sec^2 \varphi_i \sin \left(\frac{m\pi}{2} - \alpha\right) \sin \delta_m \right] \right. \\
& \quad \left. + \left(\frac{r}{RA}\right)^2 \sec \varphi_i \tan^3 \varphi_i \sin \left(\frac{m\pi}{2} - \alpha\right) \sin \delta_m \right\} (2I_{2_m} - I_{1_m}) \\
& + 2 \left\{ \frac{r}{RA} \left[2\pi \frac{K_1}{A} + \frac{K_2}{A} \left(\frac{m\pi}{2} - 2\pi \right) - \frac{z_0}{RA} \right] \left[\sec \varphi_i \cos \left(\frac{m\pi}{2} - \alpha\right) \sin \delta_m - \sec^2 \varphi_i \sin \left(\frac{m\pi}{2} - \alpha\right) \cos \delta_m \right] \right. \\
& \quad \left. + \left(\frac{r}{RA}\right)^2 \sec \varphi_i \tan^3 \varphi_i \sin \left(\frac{m\pi}{2} - \alpha\right) \sin \delta_m \right\} \cdot I_{3_m} \\
& - \left(\frac{r}{RA}\right)^2 \sec^3 \varphi_i \tan \varphi_i \sin \left(\frac{m\pi}{2} - \alpha\right) \cdot I_{1_m} \quad (A-48-a)
\end{aligned}$$

$$\begin{aligned}
\frac{T_b}{RA} \cdot \frac{\omega_r}{2C_{20}} &= \left(\frac{RA}{P_{20}}\right)^3 \left[\left\{ + \frac{r z_0}{(RA)^2} [\sec \varphi_i \sin \alpha \cos \delta_0 + \sec^2 \varphi_i \cos \alpha \sin \delta_0] - \frac{r T_b}{(RA)^2} \tan \varphi_i \sec \varphi_i \cos \delta_0 \right. \right. \\
&\quad - \left(\frac{r}{RA} \right)^2 \sec \varphi_i \tan^2 \varphi_i \cos \alpha \cos \delta_0 \} (2I_{20} - I_{10}) + 2 \left\{ \frac{r z_0}{(RA)^2} [\sec \varphi_i \sin \alpha \cos \delta_0 \right. \\
&\quad - \left. \sec^2 \varphi_i \cos \alpha \cos \delta_0] - \frac{r T_b}{(RA)^2} \sec \varphi_i \tan \varphi_i \cos \delta_0 - \left(\frac{r}{RA} \right)^2 \sec \varphi_i \tan^2 \varphi_i \cos \alpha \cos \delta_0 \} \cdot I_{30} \\
&\quad \left. + \left(\frac{r}{RA} \right)^2 \sec^2 \varphi_i \tan \varphi_i \cos \alpha \cdot I_{10} \right] \\
&+ \sum_{l=1}^3 \left(\frac{RA}{P_{2l}} \right)^3 \left[\left\{ \frac{r}{RA} \left(\frac{k_1}{A} \cdot \frac{n\pi}{2} - \frac{z_0}{RA} \right) [\sec \varphi_i \sin \left(\frac{n\pi}{2} - \alpha \right) \cos \delta_n - \sec^2 \varphi_i \cos \left(\frac{n\pi}{2} - \alpha \right) \sin \delta_n] \right. \right. \\
&\quad - \left(\frac{r}{RA} \right)^2 \tan \varphi_i \sec \varphi_i \cos \delta_n - \left(\frac{r}{RA} \right)^2 \sec \varphi_i \tan^2 \varphi_i \cos \left(\frac{n\pi}{2} - \alpha \right) \cos \delta_n \} (2I_{2n} - I_{1n}) \\
&\quad + 2 \left\{ \left(\frac{r}{RA} \right) \left[\frac{k_1}{A} \cdot \frac{n\pi}{2} - \frac{z_0}{RA} \right] [\sec \varphi_i \sin \left(\frac{n\pi}{2} - \alpha \right) \cos \delta_n + \sec^2 \varphi_i \cos \left(\frac{n\pi}{2} - \alpha \right) \cos \delta_n] \right\} \\
&\quad - \frac{r T_b}{(RA)^2} \sec \varphi_i \tan \varphi_i \cos \delta_n - \left(\frac{r}{RA} \right)^2 \sec \varphi_i \tan^2 \varphi_i \cos \left(\frac{n\pi}{2} - \alpha \right) \cos \delta_n \} \cdot I_{3n} \\
&\quad \left. + \left(\frac{r}{RA} \right)^2 \sec^2 \varphi_i \tan \varphi_i \cos \left(\frac{n\pi}{2} - \alpha \right) \cdot I_{1n} \right] \\
&+ \left(\frac{RA}{P_{2n}} \right)^3 \left[\left\{ \frac{r}{RA} \left[2\pi \frac{k_1}{A} - \frac{z_0}{RA} \right] [-\sec \varphi_i \sin \alpha \cos \delta_n - \sec^2 \varphi_i \cos \alpha \cos \delta_n] - \frac{r T_b}{(RA)^2} \tan \varphi_i \sec \varphi_i \cos \delta_n \right. \right. \\
&\quad - \left(\frac{r}{RA} \right)^2 \sec \varphi_i \tan^2 \varphi_i \cos \alpha \cos \delta_n \} (2I_{2n} - I_{1n}) + 2 \left\{ \frac{r}{RA} \left[2\pi \frac{k_1}{A} - \frac{z_0}{RA} \right] [-\sec \varphi_i \sin \alpha \cos \delta_n \right. \\
&\quad + \sec^2 \varphi_i \cos \alpha \cos \delta_n] - \frac{r T_b}{(RA)^2} \sec \varphi_i \tan \varphi_i \cos \delta_n - \left(\frac{r}{RA} \right)^2 \sec \varphi_i \tan^2 \varphi_i \cos \alpha \cos \delta_n \} \cdot I_{3n} \\
&\quad \left. + \left(\frac{r}{RA} \right)^2 \sec^2 \varphi_i \tan \varphi_i \cos \alpha \cdot I_{1n} \right] \\
&+ \left(\frac{RA}{P_{2n+1}} \right)^3 \left[\left\{ \frac{r}{RA} \left[2\pi \frac{k_1}{A} - \frac{z_0}{RA} \right] [-\sec \varphi_i \sin \alpha \cos \delta_n - \sec^2 \varphi_i \cos \alpha \cos \delta_n] - \frac{r T_b}{(RA)^2} \tan \varphi_i \sec \varphi_i \cos \delta_n \right. \right. \\
&\quad - \left(\frac{r}{RA} \right)^2 \sec \varphi_i \tan^2 \varphi_i \cos \alpha \cos \delta_n \} (2I_{2n+1} - I_{1n}) + 2 \left\{ \frac{r}{RA} \left[2\pi \frac{k_1}{A} - \frac{z_0}{RA} \right] [\sec \varphi_i \sin \alpha \cos \delta_n \right. \\
&\quad + \sec^2 \varphi_i \cos \alpha \cos \delta_n] - \frac{r T_b}{(RA)^2} \sec \varphi_i \tan \varphi_i \cos \delta_n - \left(\frac{r}{RA} \right)^2 \sec \varphi_i \tan^2 \varphi_i \cos \alpha \cos \delta_n \} \cdot I_{3n} \\
&\quad \left. + \left(\frac{r}{RA} \right)^2 \sec^2 \varphi_i \tan \varphi_i \cos \alpha \cdot I_{1n} \right] \\
&+ \sum_{l=1}^{\infty} \left(\frac{RA}{P_{2n+1}} \right)^3 \left[\left\{ \frac{r}{RA} \left[2\pi \frac{k_1}{A} + \left(\frac{n\pi}{2} - 2\pi \right) \frac{k_1}{A} - \frac{z_0}{RA} \right] [\sec \varphi_i \sin \left(\frac{n\pi}{2} - \alpha \right) \cos \delta_n - \sec^2 \varphi_i \cos \left(\frac{n\pi}{2} - \alpha \right) \sin \delta_n] \right. \right. \\
&\quad - \left(\frac{r}{RA} \right)^2 \tan \varphi_i \sec \varphi_i \cos \delta_n - \left(\frac{r}{RA} \right)^2 \sec \varphi_i \tan^2 \varphi_i \cos \left(\frac{n\pi}{2} - \alpha \right) \cos \delta_n \} (2I_{2n+1} - I_{1n}) \\
&\quad + 2 \left\{ \frac{r}{RA} \left[2\pi \frac{k_1}{A} + \left(\frac{n\pi}{2} - 2\pi \right) \frac{k_1}{A} - \frac{z_0}{RA} \right] [\sec \varphi_i \sin \left(\frac{n\pi}{2} - \alpha \right) \cos \delta_n + \sec^2 \varphi_i \cos \left(\frac{n\pi}{2} - \alpha \right) \cos \delta_n] \right\} \\
&\quad - \frac{r T_b}{(RA)^2} \sec \varphi_i \tan \varphi_i \cos \delta_n - \left(\frac{r}{RA} \right)^2 \sec \varphi_i \tan^2 \varphi_i \cos \left(\frac{n\pi}{2} - \alpha \right) \cos \delta_n \} \cdot I_{3n} \\
&\quad \left. + \left(\frac{r}{RA} \right)^2 \sec^2 \varphi_i \tan \varphi_i \cos \left(\frac{n\pi}{2} - \alpha \right) \cdot I_{1n} \right] \tag{A-4B-b}
\end{aligned}$$

$$\begin{aligned}
\frac{\bar{\lambda}_T}{2C_x} = & \left(\frac{RA}{P_{i_0}}\right)^3 \left[\left\{ \frac{rr_0}{(RA)^2} [\sec \varphi_i \cos \alpha \cos \delta_0 - \sec^2 \varphi_i \sin \alpha \sin \delta_0] + \left(\frac{r}{RA}\right)^2 \sec \varphi_i \tan^2 \varphi_i \cos \delta_0 \right\} (2I_{20} - I_{10}) \right. \\
& + \left. \left\{ \frac{rr_0}{(RA)^2} [\sec \varphi_i \cos \alpha \sin \delta_0 + \sec^2 \varphi_i \sin \alpha \cos \delta_0] + \left(\frac{r}{RA}\right)^2 \sec \varphi_i \tan^2 \varphi_i \sin \delta_0 \right\} \cdot I_{30} - \right. \\
& \left. - \left(\frac{r}{RA}\right)^2 \sec^3 \varphi_i \cdot I_{10} \right] \\
& + \sum_{n=1}^3 \left(\frac{RA}{P_{i_n}} \right)^3 \left[\left\{ \frac{rr_0}{(RA)^2} [\sec \varphi_i \cos(\frac{n\pi}{2} - \alpha) \cos \delta_n + \sec^2 \varphi_i \sin(\frac{n\pi}{2} - \alpha) \sin \delta_n] \right. \right. \\
& \left. \left. + \left(\frac{r}{RA}\right)^2 \sec \varphi_i \tan^2 \varphi_i \cos \delta_n \right\} (2I_{2n} - I_{1n}) \right. \\
& \left. + 2 \left\{ \frac{rr_0}{(RA)^2} [\sec \varphi_i \cos(\frac{n\pi}{2} - \alpha) \sin \delta_n - \sec^2 \varphi_i \sin(\frac{n\pi}{2} - \alpha) \cos \delta_n] \right. \right. \\
& \left. \left. + \left(\frac{r}{RA}\right)^2 \sec \varphi_i \tan^2 \varphi_i \sin \delta_n \right\} \cdot I_{3n} - \left(\frac{r}{RA}\right)^2 \sec^3 \varphi_i \cdot I_{1n} \right] \\
& + \left(\frac{RA}{P_{i_y^-}} \right)^3 \left[\left\{ \frac{rr_0}{(RA)^2} [\sec \varphi_i \cos \alpha \cos \delta_{y^-} - \sec^2 \varphi_i \sin \alpha \sin \delta_{y^-}] + \left(\frac{r}{RA}\right)^2 \sec \varphi_i \tan^2 \varphi_i \cos \delta_{y^-} \right\} (2I_{2y^-} - I_{1y^-}) \right. \\
& \left. + 2 \left\{ \frac{rr_0}{(RA)^2} [\sec \varphi_i \cos \alpha \sin \delta_{y^-} + \sec^2 \varphi_i \sin \alpha \cos \delta_{y^-}] + \left(\frac{r}{RA}\right)^2 \sec \varphi_i \tan^2 \varphi_i \sin \delta_{y^-} \right\} \cdot I_{3y^-} \right. \\
& \left. - \left(\frac{r}{RA}\right)^2 \sec^3 \varphi_i \cdot I_{1y^-} \right] \\
& + \left(\frac{RA}{P_{i_y^+}} \right)^3 \left[\left\{ \frac{rr_0}{(RA)^2} [\sec \varphi_i \cos \alpha \cos \delta_{y^+} - \sec^2 \varphi_i \sin \alpha \sin \delta_{y^+}] + \left(\frac{r}{RA}\right)^2 \sec \varphi_i \tan^2 \varphi_i \cos \delta_{y^+} \right\} (2I_{2y^+} - I_{1y^+}) \right. \\
& \left. + 2 \left\{ \frac{rr_0}{(RA)^2} [\sec \varphi_i \cos \alpha \sin \delta_{y^+} + \sec^2 \varphi_i \sin \alpha \cos \delta_{y^+}] + \left(\frac{r}{RA}\right)^2 \sec \varphi_i \tan^2 \varphi_i \sin \delta_{y^+} \right\} \cdot I_{3y^+} \right. \\
& \left. - \left(\frac{r}{RA}\right)^2 \sec^3 \varphi_i \cdot I_{1y^+} \right] \\
& + \sum_{m=1}^{\infty} \left(\frac{RA}{P_{i_m}} \right)^3 \left[\left\{ \frac{rr_0}{(RA)^2} [\sec \varphi_i \cos(\frac{m\pi}{2} - \alpha) \cos \delta_m + \sec^2 \varphi_i \sin(\frac{m\pi}{2} - \alpha) \sin \delta_m] \right. \right. \\
& \left. \left. + \left(\frac{r}{RA}\right)^2 \sec \varphi_i \tan^2 \varphi_i \cos \delta_m \right\} (2I_{2m} - I_{1m}) \right. \\
& \left. + 2 \left\{ \frac{rr_0}{(RA)^2} [\sec \varphi_i \cos(\frac{m\pi}{2} - \alpha) \sin \delta_m - \sec^2 \varphi_i \sin(\frac{m\pi}{2} - \alpha) \cos \delta_m] \right. \right. \\
& \left. \left. + \left(\frac{r}{RA}\right)^2 \sec \varphi_i \tan^2 \varphi_i \sin \delta_m \right\} \cdot I_{3m} \right. \\
& \left. - \left(\frac{r}{RA}\right)^2 \sec^3 \varphi_i \cdot I_{1m} \right]
\end{aligned}$$

(A-48-c)

where the subscripts define the limits of integration as follows, for $\nu = \frac{m\pi}{2}$

$$\begin{aligned} 0 &: \beta_2 = \frac{1}{2}(\pi - \delta_0 - \gamma_2) & ; \quad \beta_1 = \frac{1}{2}(\pi - \delta_0) \\ q^- &: \beta_2 = \frac{1}{2}(\pi - \delta_{q^-}) & ; \quad \beta_1 = \frac{1}{2}(\pi - \delta_{q^-} - \gamma_1) \\ q^+ &: \beta_2 = \frac{1}{2}(\pi - \delta_{q^+} - \gamma_2) & ; \quad \beta_1 = \frac{1}{2}(\pi - \delta_{q^+}) \\ m &: \beta_2 = \frac{1}{2}(\pi - \delta_m - \gamma_2) & ; \quad \beta_1 = \frac{1}{2}(\pi - \delta_m) \end{aligned}$$

$$\gamma_2 = \arctan \frac{\frac{T}{q} \tan \varphi + \cos \varphi \sin \frac{\pi}{q}}{\tan^2 \varphi + \cos^2 \frac{\pi}{q}} \quad ; \quad \gamma_1 = \arctan \frac{-\frac{T}{q} \tan \varphi - \cos \varphi \sin \frac{\pi}{q}}{\tan^2 \varphi + \cos^2 \frac{\pi}{q}}$$

and

$$\tan \varphi_0, \dots, \varphi_q^- = \frac{K_1 R}{r}$$

$$\tan \varphi_{q^+}, \dots, \varphi_m = \frac{K_2 R}{r}$$

Substituting $\alpha = 0$ in the preceding equations and for $0 \leq r_b \leq R$ yields the inflow velocity components at the blade feathering axis.

With the same assumptions of the circulation distribution along the blade feathering axis as before, the velocity components associated with the lifting line become

$$u_L = - \frac{\kappa \sin \alpha}{4\pi R} \cdot z_0 \cdot I_L \quad (A-49-a)$$

$$r_b w_L = - \frac{\kappa \cos \alpha}{4\pi R} \cdot z_0 \cdot I_L \quad (A-49-b)$$

$$w_L = \frac{r_b \kappa \sin \alpha}{4\pi R} \cdot I_L \quad (A-49-c)$$

where

$$I_L = \frac{[r_b^2 + z_0^2 + \varepsilon^2]^{\frac{1}{2}}}{[r_b^2 \sin^2 \alpha + z_0^2 + \varepsilon^2]} + \frac{r_b R \cos \alpha - [r_b^2 + z_0^2 + \varepsilon^2]}{[r_b^2 \sin^2 \alpha + z_0^2 + \varepsilon^2][r_b^2 + R^2 + z_0^2 - 2r_b R \cos \alpha + \varepsilon^2]^{\frac{1}{2}}}$$

The inflow velocity at any point is then

$$u = u_T + u_L$$

$$w = w_T + w_L$$

$$\nu = \nu_T + \nu_L$$

Having determined the entire flow field associated with the tip vortex and the lifting line, it is now possible to determine the flow field associated with the vortex sheet and hence the aerodynamic spanwise loading of the blade. The method is, by necessity, a step by step process starting at the blade tip and working inboard. The sheet will then be approximated by M helical vortex filaments of strength equal to one- M th the strength of the tip vortex and of appropriate spacing along the blade feathering axis. Assuming that the velocity components associated with a given helical vortex filament are negligible for points of equal or greater radial distance from the wake axis allows the spanwise location of the separation of the first vortex filament inboard of the tip vortex to be calculated from the equation

$$\left(\frac{M-1}{M}\right) C_x = \frac{\alpha c \bar{x}}{\delta \eta R A^2} (1 + \bar{\omega}_T) \left[\Theta - \frac{\nu_T}{\Omega R \bar{x} (1 + \bar{\omega}_T)} \right] \quad (A-50)$$

where α is the local lift curve slope; c , the local blade chord; $\bar{x} = \frac{r_b}{R}$, the non-dimensional blade station; and Θ , the local collective blade pitch angle.

Since the entire flow field associated with the tip vortex and lifting line has been determined, it is possible within the assumptions to calculate to a good degree of accuracy the position in space of the helical vortex filament under consideration. Then the associated velocity components of this helical vortex may be determined in a manner similar to that of the tip vortex. These results may be added to the flow field of the tip vortex for the calculation of the spanwise position of separation of the second vortex from the tip. The foregoing method is repeated until the blade root is reached, at which point, the remaining circulation is assumed to separate.

These calculations yield the inflow velocities along the blade span so that from the blade element theory, the spanwise aerodynamic loading becomes,

$$\frac{dT}{dr} = \frac{1}{2} \rho c \Omega^2 (1 + \bar{\omega})^2 R^2 \bar{x}^2 a \left[\Theta - \frac{\nu}{\Omega R \bar{x} (1 + \bar{\omega})} \right] \quad (A-51)$$

These calculations should be performed only at the points of separation, otherwise an appreciable error in local blade loadings will result.

The preceding outlined analysis is quite long and laborious. By making a few reasonable assumptions, it is possible to eliminate a great many of the calculations and still maintain acceptable accuracy in the results. In this case, it is necessary to calculate only the axial velocity components at the blade feathering axis and along a radius in the ultimate wake. (For normally loaded helicopter rotors the rotational component is negligible) Assuming that the vortex filament shed at a given blade radius maintains its relative position with respect to the wake boundary makes the calculation of the radial velocity components unnecessary. In addition, neglecting the lifting line increment and assuming that the mass flow is constant through an annulus at the tip path plane and an annulus at the same relative radius in the wake yields a reasonable approximation to the actual position in space of the particular vortex filament under consideration. For example, these assumptions give

$$z_f \approx \mu_{m_\infty} \left\{ \frac{v}{\Omega} + \frac{1}{\lambda_2 \Omega} \left[\ln \left(1 + 2 \frac{c}{A} e^{-\lambda_2 v} \right) - \frac{1}{16} \ln \left(1 + 4 \frac{c}{A} e^{-\lambda_2 v} \right) + \frac{1}{4} \frac{c}{A} e^{-\lambda_2 v} \right. \right. \\ \left. \left. - \ln \left(1 + 2 \frac{c}{A} \right) + \frac{1}{16} \ln \left(1 + 4 \frac{c}{A} \right) - \frac{1}{4} \frac{c}{A} \right] \right\} \quad (A-52)$$

$$r_f = \bar{x}_m \cdot RA \left[1 + \frac{c}{A} e^{-\lambda_2 v} \right] \quad (A-53)$$

where \bar{x}_m is the blade station at which the vortex filament is shed and $\mu_{m_\infty} = \mu_{T_\infty} + \sum \mu_{m_\infty}$ is the axial velocity of the flow at the corresponding point in the ultimate wake.

As before, the vortex sheet will be assumed to be approximated by M vortex filaments of strength v/M (except for the one shed at the blade root). Then having calculated the axial velocity components associated with the tip vortex along the blade feathering axis and along a radius in the ultimate wake and having neglected the rotational components, the point at which the first vortex filament inboard of the tip is shed may be calculated from the equation

$$\left(\frac{M-1}{M} \right) C_x = \frac{\alpha \bar{x}_1}{8\pi RA^2} \left[\theta_m - \frac{\mu_T}{\Omega R \bar{x}_1} \right] \quad (A-54)$$

or for the general case (except for the root)

$$\left(\frac{M-m}{M} \right) C_x = \frac{\alpha \bar{x}_m}{8\pi RA^2} \left\{ \theta_m - \frac{1}{\Omega R \bar{x}_m} \left[\mu_T + \sum_{i=1}^{m-1} \mu_{m_i} \right] \right\} \quad (A-55)$$

Following the previous procedure for the velocity components associated with a helical vortex yields the axial component at the point \bar{x} on the blade feathering axis inboard of and associated with the m th vortex filament.

$$\begin{aligned} \frac{M}{2C_x} \cdot \bar{\lambda}_m &= \left(\frac{RA}{P_{2m}} \right)^3 \left[\left\{ \bar{x}_m \left(1 + \frac{c}{A}\right) \cdot \frac{\bar{x}}{A} \sec \varphi_0 \cos \delta_0 + \bar{x}_m^2 \left(1 + \frac{c}{A}\right)^2 \sec \varphi_0 \tan^2 \varphi_0 \cos \delta_0 \right\} (2I_{2m} - I_{1m}) \right. \\ &\quad + \left\{ \bar{x}_m \left(1 + \frac{c}{A}\right) \cdot \frac{\bar{x}}{A} \sec \varphi_0 \sin \delta_0 + \bar{x}_m^2 \left(1 + \frac{c}{A}\right)^2 \sec \varphi_0 \tan^2 \varphi_0 \sin \delta_0 \right\} \cdot 2I_{3m} \\ &\quad \left. - \bar{x}_m^2 \left(1 + \frac{c}{A}\right)^2 \sec^3 \varphi_0 \cdot I_{1m} \right] \\ &\quad + \sum_{n=1}^{\infty} \left(\frac{RA}{P_{2mn}} \right)^3 \left[\left\{ \bar{x}_m \left(1 + \frac{c}{A} e^{-\frac{n\pi}{2}\lambda_2}\right) \cdot \frac{\bar{x}}{A} \left[\sec \varphi \cos \frac{n\pi}{2} \cos \delta_n + \sec \varphi \sin \frac{n\pi}{2} \sin \delta_n \right] \right. \right. \\ &\quad + \bar{x}_m^2 \left(1 + \frac{c}{A} e^{-\frac{n\pi}{2}\lambda_2}\right)^2 \sec \varphi \tan^2 \varphi \cos \delta_n \left. \right\} (2I_{2mn} - I_{1mn}) \\ &\quad + 2 \left\{ \bar{x}_m \left(1 + \frac{c}{A} e^{-\frac{n\pi}{2}\lambda_2}\right) \frac{\bar{x}}{A} \left[\sec \varphi \cos \frac{n\pi}{2} \sin \delta_n - \sec^3 \varphi \sin \frac{n\pi}{2} \cos \delta_n \right] \right. \\ &\quad + \bar{x}_m^2 \left(1 + \frac{c}{A} e^{-\frac{n\pi}{2}\lambda_2}\right)^2 \sec \varphi \tan^2 \varphi \sin \delta_n \left. \right\} \cdot I_{3mn} \\ &\quad \left. - \bar{x}_m^2 \left(1 + \frac{c}{A} e^{-\frac{n\pi}{2}\lambda_2}\right)^2 \sec^3 \varphi \cdot I_{1mn} \right] \quad (A-56) \end{aligned}$$

where $\bar{x} = \frac{r_f}{R}$

$$\bar{\lambda}_m = \frac{w_m}{\Omega RA}$$

$$\tan \varphi_m = \bar{\lambda}_{m\infty} \left(1 + \frac{c}{A} e^{-\frac{n\pi}{2}\lambda_2}\right)^{-3}$$

$$\delta_m = \arctan \frac{r_f \sin \varphi + R \bar{x} \cos \varphi \sin \frac{n\pi}{2}}{r_f \tan^2 \varphi + R F \cos \frac{n\pi}{2}}$$

$$\begin{aligned}
 P_{\text{in}}^2 = & (RA)^2 \left[\bar{x}_m^2 \left(1 + \frac{\epsilon}{A} e^{-\frac{n\pi}{2}\lambda_1} \right)^2 + \left(\frac{\bar{x}}{A} \right)^2 + \left(\frac{\bar{z}_e}{RA} \right)^2 \right. \\
 & + 2 \bar{x}_m^2 \left(1 + \frac{\epsilon}{A} e^{-\frac{n\pi}{2}\lambda_1} \right)^2 \tan^2 \varphi \sec^2 \varphi \left(1 - \cos \frac{n\pi}{2} \right) \\
 & + 2 \bar{x}_m \left(1 + \frac{\epsilon}{A} e^{-\frac{n\pi}{2}\lambda_1} \right) \cdot \frac{\bar{x}}{A} \left\{ \tan^2 \varphi \cos \frac{n\pi}{2} \right. \\
 & \quad \left. - \sec \varphi \left[\sin^2 \frac{n\pi}{2} + \sec \varphi \cos^2 \frac{n\pi}{2} \right] \right\} \\
 & \left. - 2 \bar{x}_m \left(1 + \frac{\epsilon}{A} e^{-\frac{n\pi}{2}\lambda_1} \right) \cdot \frac{\bar{z}_e}{RA} \tan \varphi \sec \varphi \sin \frac{n\pi}{2} + \left(\frac{\epsilon}{RA} \right)^2 \right]
 \end{aligned}$$

$$\begin{aligned}
 P_{\text{out}}^2 = & (RA)^2 \left[\bar{x}_m^2 \left(1 + \frac{\epsilon}{A} e^{-\frac{n\pi}{2}\lambda_1} \right)^2 + \left(\frac{\bar{x}}{A} \right)^2 + \left(\frac{\bar{z}_e}{RA} \right)^2 \right. \\
 & + 2 \bar{x}_m^2 \left(1 + \frac{\epsilon}{A} e^{-\frac{n\pi}{2}\lambda_1} \right)^2 \tan^2 \varphi \sec^2 \varphi \left(1 + \cos \frac{n\pi}{2} \right) \\
 & + 2 \bar{x}_m \left(1 + \frac{\epsilon}{A} e^{-\frac{n\pi}{2}\lambda_1} \right) \cdot \frac{\bar{x}}{A} \left\{ \tan^2 \varphi \cos \frac{n\pi}{2} \right. \\
 & \quad \left. + \sec \varphi \left[\sin^2 \frac{n\pi}{2} + \sec \varphi \cos^2 \frac{n\pi}{2} \right] \right\} \\
 & \left. + 2 \bar{x}_m \left(1 + \frac{\epsilon}{A} e^{-\frac{n\pi}{2}\lambda_1} \right) \frac{\bar{z}_e}{RA} \tan \varphi \sec \varphi \sin \frac{n\pi}{2} + \left(\frac{\epsilon}{RA} \right)^2 \right]
 \end{aligned}$$

and the subscripts define the limits of integration as follows

$$o : \beta_2 = \frac{1}{2}(\pi - \delta_o - \gamma_2) ; \beta_1 = \frac{1}{2}(\pi - \delta_o)$$

$$n : \beta_2 = \frac{1}{2}(\pi - \delta_n - \gamma_2) ; \beta_1 = \frac{1}{2}(\pi - \delta_o - \gamma_1)$$

For the ultimate wake the axial component at the radial station \bar{x} inboard of and associated with the m th vortex filament is

$$\frac{M}{2C_x} \cdot \bar{I}_{m\infty} = \left(\frac{RA}{P_{\text{out}}^2} \right)^3 \left[\left\{ \bar{x}_m \cdot \frac{\bar{x}}{A} \sec \varphi_\infty \cos \delta_\infty + \bar{x}_m^2 \sec \varphi_\infty \tan^2 \varphi_\infty \cos \delta_\infty \right\} (I_{2,o} - I_{1,o}) \right]$$

$$\begin{aligned}
& + \sum_{m=1}^{\infty} 2 \left(\frac{RA}{P_m} \right)^3 \left[\bar{x}_m \cdot \frac{\bar{x}}{A} \left[\sec \varphi_m \cos \frac{n\pi}{2} \cos \delta_m + \sec^2 \varphi_m \sin \frac{n\pi}{2} \sin \delta_m \right] \right. \\
& \quad \left. + \bar{x}_m^2 \sec \varphi_m \tan^2 \varphi_m \cos \delta_m \right] (2I_{z_m} - I_{l_m}) \\
& + 2 \left[\bar{x}_m \cdot \frac{\bar{x}}{A} \left[\sec \varphi_m \cos \frac{n\pi}{2} \sin \delta_m - \sec^2 \varphi_m \sin \frac{n\pi}{2} \cos \delta_m \right] \right. \\
& \quad \left. + \bar{x}_m^2 \sec \varphi_m \tan^2 \varphi_m \sin \delta_m \right] I_{z_m} - \bar{x}_m^2 \sec^3 \varphi_m \cdot I_{l_m} \]
\end{aligned} \tag{A-57}$$

where the limits of integration are

$$\beta_2 = \frac{1}{2}(\pi - \delta_m - \gamma_2) \quad ; \quad \beta_1 = \frac{1}{2}(\pi - \delta_\infty - \gamma_1)$$

Now calculating equations (A-55), (A-56), and A-57) in turn yields the axial component of the inflow velocity along the blade feathering axis and hence the blade spanwise aerodynamic loading becomes

$$\left(\frac{dT}{dr} \right)_m = \frac{1}{2} \rho \times \Omega^2 R^2 \bar{x}_m^2 a \left[\theta - \frac{1}{\Omega R \bar{x}_m} \left(w_T + \sum_{m=1}^{m-1} w_m \right) \right] \tag{A-58}$$

This is, of course, the desired result of the analysis.

Calculations and Discussion

Since the calculations are very time consuming, it was not feasible to determine the theoretical variations of all the various tip vortex geometric parameters with vortex strength coefficient. However, in order to check the approach, the variations of λ_x and K_x were determined. To make these computations, it was necessary to determine the radius of the vortex core, which is very difficult to do theoretically. The smoke pictures showed, qualitatively, that the radius of the core increased with vortex strength coefficient and with azimuth position from the blade. It was found that if the core radius at the blade tip was taken to be

$$\left(\frac{E}{RA} \right)_0 = 10 C_x$$

and if the variation with azimuth position from the blade was taken to be

$$\left(\frac{\epsilon}{RA}\right) = \left(\frac{\epsilon}{RA_0}\right) \left[A + Be^{-\lambda_1 \Omega t} + Ce^{\lambda_2 \Omega t} \right]^{-\frac{1}{2}}$$

then the agreement of the theoretical values of λ_2 and K_2 with experimental values was very good. In addition, these values of vortex core radius compared in a qualitative manner with the experimental evidence. The core diameter could not be determined from the smoke pictures because it was not possible to distinguish the rotational part of the vortex from the irrotational part.

The wake contraction exponent, λ_2 , was determined from equation A-37 and is plotted in figure 3. The ultimate wake helix pitch angle parameter, K_2 , was determined from equations A-26, A-27, and A-28 and is plotted in figure 4. As can be seen from these figures, the agreement between theoretical and experimental values is quite good.

The method of computing K_2 given in this paper was compared with the numerical integration method of reference 18 by comparing the values obtained from the calculations. It was found that the values were identical to three significant figures. This shows that the replacement of a quadrant of the helix with a circular arc yields a good approximation over the interval of integration.

The theoretical variation of vortex strength coefficient with thrust coefficient is given in figure 5. This curve was determined by calculating the strength of the bound vortex at the 90 percent blade radius and then making the assumption that this entire circulation was shed at the blade tip, thereby forming the tip vortex.

It was stated in reference 18 that the blade collective pitch angles appeared to be about one-half degree too large but that it was not possible to determine the source of this error. Subsequent to the publication of this reference, the source of the error was found so that the axial induced velocity distribution and aerodynamic loading along the blade feathering axis have been recalculated and are presented in figures 6 and 7. Since the original results were obtained by a numerical integration, this same method was used to recalculate the axial components of induced velocity. In this case, it was assumed that the strength of the blade bound vortex varied in a linear manner from a maximum at the blade tip to zero at the axis of rotation. The resulting vortex sheet was replaced by finite helical vortex filaments starting at the 0.90 blade station and at intervals of 0.10 until the blade root was reached at the 0.22 blade station at which point the remaining strength was shed. The motion of the vortex filament from the 0.90 blade station was determined approximately and its associated velocity field was determined non-dimensionally by numerical integration. It was assumed that the remaining inboard vortex filaments had the same relative motion and hence the same non-dimensional velocity field as this filament. The axial induced velocities could then be found along the blade feathering axis by adding the contributions from the whole vortex system. The axial induced velocities are plotted in figure 6 and compared with the values obtained by the method of Goldstein and Lock and from simple momentum considerations. The aerodynamic loadings were calculated for the induced velocities of

this paper and that of Goldstein and Lock and are presented in figure 7. As can be seen, the method of this paper yields an integrated thrust which is very close to the experimental value whereas the method of Goldstein and Lock is about ten percent low. There are no experimental pressure distributions for a single-bladed rotor available so that a comparison of loadings is not possible.

The method presented in this paper was used to calculate the velocity associated with the tip vortex at a point on the blade feathering axis and the result was compared with the value obtained by numerical integration. It was found, as was expected, that the replacement of the helix with quadrants of a circle (except for the first segment starting from the blade tip which was replaced by a 45° arc) resulted in an error of over ten percent. By replacing only the first segment with 10° arcs (except for the segment starting from the blade tip which was replaced by a 5° arc) the error was reduced to a few percent. Further reduction in size of the arcs will, of course, decrease the error. In all cases, $\frac{d\gamma}{dy} = \frac{de}{y} = 0$. A sample calculation for small arcs showed this to result in negligible error.

Part B. An Isolated Rotor in Forward Flight

Introduction

The forward flight case presents many more difficulties than did the hovering flight case. In the latter, the flow field was steady with respect to the blade whereas in forward flight, the flow varies periodically and the helix pitch angle varies quite radically with azimuth position, particularly for the higher advance ratios. For these reasons, a theoretical solution similar to that in Part A does not appear to be feasible. Therefore, the analysis of the blade spanwise aerodynamic loading becomes, of necessity, a semi-empirical process in which the geometric parameters must be determined from and the required simplifying assumptions based on a series of smoke studies. These smoke studies and their results will be discussed in the following sections.

Description of Apparatus and Testing Procedures

The model rotor and thrust stand were the same as those used in reference 18. The single, counter-balanced blade had the following characteristics.

Radius -----	4 feet
Chord -----	0.5 feet (Constant)
Airfoil section (no twist or taper) -----	NACA 0015
Rotor solidity ratio -----	0.040
Blade flapping moment of inertia -----	0.67 slugs- ft ²

The blade collective pitch angle could be pre-set manually at any desired angle between zero and fifteen degrees. The blade was allowed to flap about a zero offset axis in order to eliminate the thrust moment about the hub. The blade tip shape was obtained by rotating the airfoil section about the chord line.

The model rotor and thrust stand were mounted on a built-up platform anchored to the bed of a three-quarter ton pick-up truck as shown in figure 8. This placed the rotor disk plane about fifteen feet above the pavement and about ten feet above the truck cab roof. The rotor was, in effect, mounted in an inverted position so that the wake passed upward into an air space relatively undisturbed by the passage of the various struts and braces.

Two remotely controlled gun cameras were mounted on outriggers as shown, one at the side and one at the front. The cameras were so placed that their optical axes were normal to and intersected the no-feathering axis.(in this case, the shaft axis) at the latter's blade flapping axis intersection. Illumination was provided for the side camera by a row of twenty-seven 100-watt aircraft landing lamps mounted in the longitudinal plane about seven feet below and approximately parallel to the

rotor and so shielded as to produce an upwardly directed rectangular beam of light four inches thick and twelve feet long. Thus the pictures taken from the side were of a longitudinal cross-section of the wake. Illumination for the front camera was provided by four RFL-2 reflector flood lamps and the front pictures yielded an overall view of the flow field. A 1/2 - inch f 1.5 lens was installed in each camera. This allowed the side camera to cover a field at the shaft axis of about eight by eleven feet from a distance of fifteen feet and the front camera about seven by nine feet from a distance of about twelve feet. Both camera speeds were set at 64 - frames per second.

Blade azimuth position indicators were mounted in the camera field of view on the vertical drive shaft housing and were photographed along with the smoke flow. These indicators were merely a graduated face and a pointer driven by a selsyn motor whose generator was geared to the drive shaft.

The space beneath the platform was divided into two compartments. The aft compartment contained the oscillograph recorder, a four-channel carrier amplifier, a band-pass filter, and various other electrical signal filters and junction boxes.

Installed in the forward compartment was a gasoline engine, two 24-volt 200-ampere aircraft generators, four 6-volt storage batteries in series and parallel to the load as line voltage stabilizers, a 400-cycle inverter, and a fifty gallon barrel of water for cooling the gasoline engine. The gear driven generator supplied a constant 24-volt source for the inverter, the lighting system, some of the instrumentation components and the cameras. The output of the belt driven generator was connected directly to the rotor drive motor. The output of this generator and hence the rotor RPM was controlled by varying the voltage supplied to the generator's field.

The method of producing smoke was both simple and effective. A reservoir for the titanium tetrachloride was mounted on top of the rotor hub on the axis of rotation. A short piece of plastic tubing conducted the liquid into a one-eighth inch O.D. stainless steel tube buried in the wooden blade. This tube emptied into a reservoir stuffed with cotton and open to the air at the blade tip. Exposure of the titanium tetrachloride to the air produced a thick white smoke which remained within the core of the tip vortex and clearly showed its position in space. The amount of liquid pumped to the blade tip could be adequately controlled after a little experimentation by constricting the plastic tube.

In addition to the recording on film of the position in space of the tip vortex with the blade azimuth position, the steady state thrust component, the forward speed, and the rotor RPM were recorded by an oscillograph recorder. The steady state thrust was measured by a strain-gage beam. The forward speed was determined by counting the recorded revolutions of an autosyn which was driven by a fifth wheel. The RPM was determined in a similar manner from an autosyn geared to the rotor drive shaft. An attempt was also made to measure the first and second harmonic thrust variations by including a properly tuned band-pass filter in the strain gage circuit but the variations were of the same level as the thrust components of the truck bounce so that no reliable data could be obtained.

The tests were conducted within a completely enclosed space thirty feet wide, twenty-six feet high at the eaves, and four-hundred and fifty feet long, of which about two-hundred and seventy feet were available for the truck movements. The minimum blade clearance occurred at the tip of the advancing blade which passed within about six feet of the side of the building. This was a necessary compromise with the positioning on the opposite side of the truck of the side camera so that its field of view would be great enough.

A typical test run began with the truck at one end of the building with the rotor hovering. The truck was accelerated until a steady forward speed was reached at which point the data was recorded. The truck, and then the rotor was stopped. The necessary controls were so arranged that the testing could be accomplished by one man.

Discussion and Results of the Smoke Studies

It should first, perhaps, be pointed out that the flow visualization studies to be discussed were instituted primarily as exploratory research into the basic problem of the variation of the inflow velocity at the blades of a helicopter rotor in hovering and in forward flight. The main efforts were directed toward proving the validity of the approach and the setting-up of a semi-empirical theory rather than the development of charts and tables which could be used for design purposes. The theory, having been carried as far as possible without the support of the experimental data, seemed to indicate that if the assumption were made that the presence of the helical sheet of vorticity in the wake had no effect on the motion of the helical vortex shed from the tip, then specifying the tip vortex strength coefficient, the angle of attack of the tip path plane, and the advance ratio along the flight path would specify all the geometric parameters required to give the position of the vortex in space. However due to the fact that the project was committed to a very limited budget, it became necessary to design the test program around the available equipment. For this reason the independent variables were taken to be the blade collective pitch angle, the angle of attack of the axis of no-feathering, and the advance ratio along the flight path, i.e. parallel to the ground. The values chosen for these parameters were as follows.

Blade collective pitch angle, θ_0 -----	$8^\circ, 9^\circ, 10^\circ$
Shaft angle of attack, α_s -----	$-0.5^\circ; -4.5^\circ; -8.5^\circ$
Advance ratio along flight path, M_y -----	0 to 0.15

The limitation on the advance ratio was established by the truck performance in the available space and the fact that slowing up the rotor so decreased the strength of the tip vortex that it became difficult to photograph the flow. Experimental thrust coefficients versus advance ratio are given in figures 9, 10 and 11 for various values of blade collective pitch angle and shaft angle of attack.

Typical side views of the tip vortex are shown in figure 12. As can be seen, the motion of the vortex appears to be quite complex and the distortion which occurs over the trailing half of the wake is very clear. There is no indication from any of the pictures taken that this distortion ceases before the wake is dissipated. In effect, this means that the vortex motion is not steady with respect to any system of axes as was to be expected. Fortunately, however, it is periodic with respect to blade axes and can be approximated rather easily, as will be shown later.

A totally unexpected phenomenon was observed in the front views of the wake for the shaft inclinations of -0.5° and -4.5° . This phenomenon occurred for the former case, whenever the forward speed became large enough so that the leading edge of the wake was swept back under the center of the rotor, and in addition for the latter case whenever the combination of the blade coning and blade flapping angles become great enough so that the blade axis in the forward position lay parallel to the flight velocity vector. Then approximately $\frac{1}{12}$ seconds after the vortex was shed from the tip of the blade as the blade passed through the forward longitudinal plane, this section of the vortex would appear to be literally split and thereafter to separate at the longitudinal plane. Succeeding frames would show both ends of the divided vortex quickly disappearing to the sides and downstream. It is known that the fluid in this region, in addition to its radial and axial movement, has a tangential (or at this point, a lateral) velocity component away from the longitudinal plane of the wake on both sides of this plane. Qualitatively therefore, it can be seen that this would tend to separate the fluid elements at this plane. A sequence of photographs retouched to make the phenomenon reproducible, is given in figure 13. The longitudinal point of separation in all cases observed was very close to the center of the rotor. The phenomenon was not observed with the shaft inclination set at -8.5° . It is presumed that the reason for this was that the forward speeds attained during the tests were not sufficient to cause the advancing blade to flap to a high enough angle so that the blade feathering axis in the forward position lay parallel to the flight path.

In the hovering flight case, it was only necessary to know the contraction of the wake boundaries and the vertical displacement along the boundaries as a function of the azimuth position from the blade in order to determine the position in space of the tip vortex. In the forward flight case, an additional parameter comes into being. This is the displacement of the wake centerline in the downwind direction and parallel to the tip path plane. To define these parameters, it would be best to orient the coordinate system so that the XY plane coincides with the tip path plane and the X axis intersects the blade feathering axis at the blade tip, with the positive Z direction being opposite to the component of the rotor force perpendicular to the tip path plane. However, for the same reasons previously noted, it was necessary to orient the coordinate system so that the Z axis lay along the no-feathering axis and the Y-axis coincided with the blade flapping axis. No attempt was made to correct the data to the tip path plane reference system because the measurement of the flapping angle from the photographs was not sufficiently accurate and it was also felt that the available flapping theory was not accurate enough to warrant the additional labor. This latter view is supported by the theoretical and experimental comparisons in references 6 and 19.

The position of the tip vortex in space was determined from a frame-by-frame study of the motion pictures. The side view study was relatively easy since the photographs showed a longitudinal cross-section of the flow. The front view, however, required extra care since the flow was moving away from the camera and hence the measurements had to be corrected for this movement by correlation with the longitudinal pictures. Only the longitudinal and lateral points of the vortex were considered. Thus by tracing out the movement of these segments of the tip vortex during a number of revolutions of the blade, it was possible to determine the longitudinal and lateral wake boundaries. Then the problem arose as to the shape of the wake boundary in the quadrants between these points. Further consideration of the data showed that if the wake boundaries for the four positions were plotted as a function of their individual azimuth positions from the blade, then the four points determined, within experimental error a circular cross-section of the wake. It was therefore assumed that through each point on the wake centerline, it was possible to pass a plane whose intersection with the wake boundary was a circle. These circular cross-sections necessarily become tilted both laterally and longitudinally with respect to the tip path plane as they progress down the centerline of the wake. This tilt back was predicted in reference 10 and, as pointed out in that reference, will affect the theoretical calculation of the wake angle. A typical example of the longitudinal tilt of the planes of the circles is shown in figure 14. The intersections of these planes with the longitudinal plane are indicated at intervals of $\frac{\pi}{2n}$ seconds or 90° of blade rotation.

Further consideration of the flow pictures brought out the possibility that these circular cross-sections of the wake would be a convenient means of describing the position in space of the wake boundary. Investigation of the data with this in mind showed that a very real advantage would be obtained by such a representation for then the radius of a point on the central curve of the tip vortex as measured from the centerline of the wake and in the plane of these circles become a function only of the azimuth position, φ , of the point from the blade feathering axis and hence independent of the azimuth position, φ' , of the blade itself. Thus, as for the hovering case but neglecting the heavily convergent term,

$$r = R[A + Ce^{-\lambda_2 \varphi'}] \quad (B-1)$$

where $A + C = 1$ and the experimentally measured values of A and λ_2 are shown in figures 15 and 16. As may be seen from these figures, it was not possible to determine a variation in these two parameters with either collective pitch or shaft inclination. It is believed that over the normal range of blade collective pitch angles and shaft inclination for low speed flight close to the horizontal, this variation would be small and hence the use of the average values shown should introduce negligibly small errors in the results.

Now it is necessary to determine the locus of the centers of the circular cross-section of the wake. It was observed that the lateral tilt seemed to occur about the longitudinal diameter of the circle while the longitudinal tilt appeared to occur about the trailing edge of the wake. Since there was no observable lateral movement of the wake, the lateral position of the centers posed no problem as they remained in the longitudinal plane of the rotor. However, the downwind movement of

the center in the longitudinal plane and parallel to the tip path plane appeared to be made up of two components; one, a translation due to the component of the flight velocity parallel to the tip path plane and the other, a component due to the rotation of the centers about the trailing edge of the wake. The sum of these two motions may be approximated by the expression

$$K_x R \psi' = M_y R \psi' \sin \alpha + r - \frac{1}{2} [4r^2 - \Delta K^2 R^2 \psi'^2]^{\frac{1}{2}} \quad (B-2)$$

where ΔK is the difference between the Z motion parameter at the trailing edge and that at the leading edge of the wake and α is the angle of attack of the tip path plane. Experimental values of the parameter K_x are plotted versus the advance ratio in figure 17 for $\psi' > 4\pi$. Note that the contribution of the tilt-back of the circular cross-sections accounts for about 10% of this parameter.

The wake skew angle, χ , is given as a matter of interest in figure 18. Due to the aforementioned motions of the tip vortex, it was necessary to reference this angle as lying in the longitudinal plane between the no-feathering axis and the extended trailing edge of the wake as shown.

The parameters remaining to be determined are those describing the displacement of the tip vortex normal to the tip path plane. Again it is necessary for the reason as stated before to present instead, the experimentally determined parameters which describe the displacement parallel to the axis of no-feathering. Plotting this displacement versus the azimuth position for the four points about the periphery of the wake showed that there were three distinct sections of the tip vortex, in each of which the rate of change of the displacement parallel to the no-feathering axis with respect to azimuth position was a constant. A typical plot is shown in figure 19. As may be seen, the Z -coordinates of the tip vortex may be expressed very simply. For instance for $M_y < 0.06$ approximately

$$z' = -M_y R \psi' \sin \alpha_s + K_1 R \psi' \quad 0 \leq \psi' < 2\pi \quad (B-3)$$

$$z' = -M_y R \psi' \sin \alpha_s + 2\pi R K_1 + K_2 R (\psi' - 2\pi) \quad 2\pi < \psi' < 3\pi \quad (B-4)$$

$$z' = -M_y R \psi' \sin \alpha_s + 2\pi K_1 R + \pi K_2 R + K_3 R (\psi' - 3\pi) \quad 3\pi < \psi' < \infty \quad (B-5)$$

where the K 's are now a function of the azimuth angle, ψ' , of the point on the helix from the longitudinal plane. For $M_y > 0.06$ the limits of equations B-4 and B-5 change and the expressions become

$$z' = -M_y R \psi' \sin \alpha_s + 2\pi K_1 R + K_2 R (\psi' - 2\pi) \quad 2\pi < \psi' < 4\pi \quad (B-6)$$

$$z' = -M_y R \psi' \sin \alpha_s + 2\pi K_1 R + 2\pi K_2 R + K_3 R (\psi' - 4\pi) \quad 4\pi < \psi' < \infty \quad (B-7)$$

The advance ratio at which the change occurs was not well defined so that M_y of 0.06 was arbitrarily chosen as being about the midpoint of the scatter. The measured

values of K_1 , K_2 , and K_3 are given in figures 20, 21, and 22.

In order to describe these parameters more simply over the quadrants between the four measured points, it was decided to consider the trailing two quadrants and the leading two quadrants separately and to assume a variation which would match at the lateral positions. An expression was chosen which seemed to approximate the variation but it was not possible to verify the expression from the experimental measurements. Therefore it was assumed that for the trailing two quadrants of the wake

$$K_{m_y} = \frac{1}{2} K_{m_0} + \frac{1}{4} (K_{m_{180}} + K_{m_{270}}) + \frac{1}{2} (K_{m_{90}} - K_{m_{270}}) \sin \gamma \\ + \frac{1}{2} [K_{m_0} - \frac{1}{2} (K_{m_{90}} + K_{m_{270}})] \cos 2\gamma \quad (B-8)$$

and for the leading two quadrants of the wake

$$K_{m_y} = \frac{1}{2} K_{m_{180}} + \frac{1}{4} (K_{m_{90}} + K_{m_{270}}) + \frac{1}{2} (K_{m_{90}} - K_{m_{180}}) \sin \gamma \\ + \frac{1}{2} [K_{m_{180}} - \frac{1}{2} (K_{m_{90}} + K_{m_{270}})] \cos 2\gamma \quad (B-9)$$

where $m = 1, 2, 3$; the K 's are read from figures 20, 21, and 22 as required; and the angle γ , like ψ , is measured in the direction of rotation of the blade and ranges from 0 to 2π .

The only parameters which showed a detectable variation with blade collective pitch angle and shaft angle of attack were the K_{m_y} . This may be seen by comparing figures 20, 21, and 22. In order to show this variation more clearly, these parameters are plotted again in figures 23 through 30 as a function of advance ratio and blade collective pitch angle for constant shaft angle of attack. In general, the effect of increasing blade collective pitch angle is to increase the magnitude of K_{m_y} , while tilting the shaft axis in the direction of motion decreases the magnitude.

All of the recorded data are given in Tables I and II. Table I presents the data which were used to construct figures 9, 10, 11, and 15 through 30. Table II presents the remaining unreduced and duplicate data.

Semi-empirical Analysis for Inflow Velocities Associated with the Tip Vortex

Having determined the position in space of the tip vortex, the calculation of the flow field associated with this vortex becomes a fairly straightforward process. It is necessary, however, to make a simplifying assumption as to the distribution of

vorticity in the rotor wake. It will be assumed that the strength of the tip vortex is constant with azimuth position. This assumption also implies that there is no azimuthal variation in the strength of the vortex sheet which is shed inboard along the blade. Then the expressions in article 149 of reference 17 may be used to calculate the entire flow field due to the tip vortex, these expressions are

$$u_x = \frac{\chi}{4\pi} \int \left\{ \frac{dy'}{dt'}(z-z') - \frac{dz'}{dt'}(y-y') \right\} \frac{dt'}{P^3} \quad (B-10-a)$$

$$u_y = \frac{\chi}{4\pi} \int \left\{ \frac{dx'}{dt'}(x-x') - \frac{dz'}{dt'}(z-z') \right\} \frac{dt'}{P^3} \quad (B-10-b)$$

$$u_z = \frac{\chi}{4\pi} \int \left\{ \frac{dx'}{dt'}(y-y') - \frac{dy'}{dt'}(x-x') \right\} \frac{dt'}{P^3} \quad (B-10-c)$$

$$P^2 = (x-x')^2 + (y-y')^2 + (z-z')^2 + \epsilon^2 \quad (B-11)$$

where (x, y, z) are the coordinates of the point under consideration; $\psi'(x', y', z')$ define the position in space of the central curve of the tip vortex, P , the distance between (x, y, z) and $\psi'(x', y', z')$; and χ the strength of the tip vortex. The coordinate system is given in figure 31 where it will be noticed that the tip path plane is being used as the plane of reference in this analysis.

In order to simplify the analysis, the core of the vortex (i.e. that part which rotates as a solid body) will be excluded from the analysis. Then for any other point in space, the expression for the velocity components associated with the tip vortex are readily determinable as will be shown below.

It will be more convenient to split each of equations B-10 into three intervals of integration. For shortness of notation, let

$$J_x = \left\{ \frac{dy'}{dt'}(z-z') - \frac{dz'}{dt'}(y-y') \right\} \frac{1}{P^3} \quad (B-12-a)$$

$$J_y = \left\{ \frac{dx'}{dt'}(x-x') - \frac{dz'}{dt'}(z-z') \right\} \frac{1}{P^3} \quad (B-12-b)$$

$$J_z = \left\{ \frac{dx'}{dt'}(y-y') - \frac{dy'}{dt'}(x-x') \right\} \frac{1}{P^3} \quad (B-12-c)$$

Then

$$u_x = \frac{\chi}{4\pi} \int_0^{2\pi} J_{x_1} dt' + \frac{\chi}{4\pi} \int_{2\pi}^{3\pi} J_{x_2} dt' + \frac{\chi}{4\pi} \int_{3\pi}^{\infty} J_{x_3} dt' \quad (B-13-a)$$

For $\mu_y < 0.06$

And

$$u_x = \frac{\chi}{4\pi} \int_0^{2\pi} J_{x_1} dt' + \frac{\chi}{4\pi} \int_{2\pi}^{4\pi} J_{x_2} dt' + \frac{\chi}{4\pi} \int_{4\pi}^{\infty} J_{x_3} dt' \quad (B-14-a)$$

For

$$\mu_y > 0.06$$

with similar expressions for u_y and u_z . These equations must be evaluated by graphical or numerical means. Hence the expressions we are interested in are the following

$$\frac{4\pi}{x} \frac{du_x}{d\psi'} = J_{x_1}, \quad 0 \leq \psi' < 2\pi \quad (B-15-a)$$

$$= J_{x_2} \quad 2\pi < \psi' < 3\pi ; M_y < 0.06 \quad (B-16-a)$$

$$2\pi < \psi' < 4\pi ; M_y > 0.06 \quad (B-17-a)$$

$$= J_{x_3} \quad 3\pi < \psi' < \infty ; M_y < 0.06 \quad (B-18-a)$$

$$4\pi < \psi' < \infty ; M_y > 0.06 \quad (B-19-a)$$

with again similar expressions for $\frac{4\pi}{x} \frac{du_y}{d\psi'}$ and $\frac{4\pi}{x} \frac{du_z}{d\psi'}$.

From the preceding section which describes the results of the smoke studies, we get the coordinates of the central curve of the helix with respect to the blade axes. For the interval $0 \leq \psi' < 2\pi$

$$x'_1 = \frac{1}{2} \left[4r^2 - L_1 R^2 \psi'^2 \cos^2 \psi' - M_1^2 R^2 \psi'^2 \sin^2 \psi' \right]^{\frac{1}{2}} \cos \psi' \\ + \left[M_y R \psi' \cos \alpha + r - \frac{1}{2} (4r^2 - L_1^2 R^2 \psi'^2)^{\frac{1}{2}} \right] \cos \psi' \quad (B-20)$$

$$y'_1 = \frac{1}{2} \left[4r^2 - L_1^2 R^2 \psi'^2 \cos^2 \psi' - M_1^2 R^2 \psi'^2 \sin^2 \psi' \right]^{\frac{1}{2}} \sin \psi' \\ + \left[M_y R \psi' \cos \alpha + r - \frac{1}{2} (4r^2 - L_1^2 R^2 \psi'^2)^{\frac{1}{2}} \right] \sin \psi' \quad (B-21)$$

$$z'_1 = -M_y R \psi' \sin \alpha + K_{1y} R \psi' \quad (B-22)$$

where $L_1 = K_{1x} - K_{1y}$; $M_1 = K_{1xy} - K_{1zz}$; K_{1y} is determined from equations B-8 and B-9 as appropriate, and $r = R[A + C e^{-\lambda \psi'}]$. Equations B-20, B-21 and B-22 may be easily differentiated with respect to ψ' (remembering that $d\psi'/d\psi' = -1$). For given C_x , M_y , α , and ψ' (or for this paper θ_0 , M_y , α_s , and ψ') the quantities x'_1 , y'_1 , z'_1 , $\frac{dx'_1}{d\psi'}$, $\frac{dy'_1}{d\psi'}$, $(x'_1 - z'_1)$, $(y'_1 - z'_1)$, and $(x'_1 - y'_1)$ may be calculated, hence the J_{x_1} , J_{y_1} , and J_{z_1} for a sufficient number of points ψ' within the interval to allow the curves to be plotted. The areas under these curves multiplied by the graphs' scale factor and $\frac{4\pi}{x}$ are the inflow velocities at the point x , y , z associated with the first turn of the tip vortex.

For the interval

$$2\pi < \psi' < 3\pi ; M_y < 0.06 ; \text{ and } 2\pi < \psi' < 4\pi ; M_y > 0.06$$

$$x_2' = \frac{1}{2} \left\{ 4r^2 - [4\pi^2 L_1^2 + L_2^2 (\gamma' - 2\pi)^2] R^2 \cos^2 \gamma - [4\pi^2 M_1^2 + M_2^2 (\gamma' - 2\pi)^2] R^2 \sin^2 \gamma \right\}^{\frac{1}{2}} \cos \gamma' \\ + \left\{ \mu_y R \gamma' \cos \alpha + r - \frac{1}{2} [4r^2 - 4\pi^2 L_1^2 R^2 - L_2^2 (\gamma' - 2\pi)^2] \right\}^{\frac{1}{2}} \cos \gamma \quad (B-23)$$

$$y_2' = \frac{1}{2} \left\{ 4r^2 - [4\pi^2 L_1^2 + L_2^2 (\gamma' - 2\pi)^2] R^2 \cos^2 \gamma - [4\pi^2 M_1^2 + M_2^2 (\gamma' - 2\pi)^2] R^2 \sin^2 \gamma \right\}^{\frac{1}{2}} \sin \gamma' \\ + \left\{ \mu_y R \gamma' \cos \alpha + r - \frac{1}{2} [4r^2 - 4\pi^2 L_1^2 R^2 - L_2^2 (\gamma' - 2\pi)^2 R^2] \right\}^{\frac{1}{2}} \sin \gamma \quad (B-24)$$

$$z_2' = -\mu_y R \gamma' \sin \alpha + 2\pi K_{1y} R + K_{2y} R (\gamma' - 2\pi) \quad (B-25)$$

where $L_2 = K_{1y} - K_{2y}$; $M_2 = K_{2y}$; and the remaining terms and the contribution associated with this segment of the vortex is as calculated before.

For the interval $3\pi < \gamma' < \infty$; $\mu_y < 0.06$

$$x_3' = \frac{1}{2} \left\{ 4r^2 - [4\pi^2 L_1^2 + \pi^2 L_2^2 + L_3^2 (\gamma' - 3\pi)^2] R^2 \cos^2 \gamma - [4\pi^2 M_1^2 + \pi^2 M_2^2 + M_3^2 (\gamma' - 3\pi)^2] R^2 \sin^2 \gamma \right\}^{\frac{1}{2}} \cos \gamma' \\ + \left\{ \mu_y R \gamma' \cos \alpha + r - \frac{1}{2} [4r^2 - 4\pi^2 L_1^2 R^2 - \pi^2 L_2^2 R^2 - L_3^2 R^2 (\gamma' - 3\pi)^2] \right\}^{\frac{1}{2}} \cos \gamma \quad (B-26)$$

$$y_3' = \frac{1}{2} \left\{ 4r^2 - [4\pi^2 L_1^2 + \pi^2 L_2^2 + L_3^2 (\gamma' - 3\pi)^2] R^2 \cos^2 \gamma - [4\pi^2 M_1^2 + \pi^2 M_2^2 + M_3^2 (\gamma' - 3\pi)^2] R^2 \sin^2 \gamma \right\}^{\frac{1}{2}} \sin \gamma' \\ + \left\{ \mu_y R \gamma' \cos \alpha + r - \frac{1}{2} [4r^2 - 4\pi^2 L_1^2 R^2 - \pi^2 L_2^2 R^2 - L_3^2 R^2 (\gamma' - 3\pi)^2] \right\}^{\frac{1}{2}} \sin \gamma \quad (B-27)$$

$$z_3' = -\mu_y R \gamma' \sin \alpha + 2\pi K_{1y} R + \pi K_{2y} R + K_{3y} R (\gamma' - 3\pi) \quad (B-28)$$

For $\mu_y > 0.06$, the interval becomes $4\pi < \gamma' < \infty$ and

$$x_3' = \frac{1}{2} \left\{ 4r^2 - [4\pi^2 (L_1^2 + L_2^2) + L_3^2 (\gamma' - 4\pi)^2] R^2 \cos^2 \gamma - [4\pi^2 (M_1^2 + M_2^2) + M_3^2 (\gamma' - 4\pi)^2] R^2 \sin^2 \gamma \right\}^{\frac{1}{2}} \cos \gamma' \\ + \left\{ \mu_y R \gamma' \cos \alpha + r - \frac{1}{2} [4r^2 - 4\pi^2 R^2 (L_1^2 + L_2^2) - L_3^2 R^2 (\gamma' - 4\pi)^2] \right\}^{\frac{1}{2}} \cos \gamma \quad (B-29)$$

$$\begin{aligned} M_3' = & \frac{1}{2} \left\{ 4r^2 - [4\pi^2(L_1^2 + L_2^2) + L_3^2(\gamma' - 4\pi)^2]R^2 \cos^2 \gamma' \right. \\ & \left. - [4\pi^2(M_1^2 + M_2^2) + M_3^2(\gamma' - 4\pi)^2]R^2 \sin^2 \gamma' \right\}^{\frac{1}{2}} \sin \gamma' \\ & + \left\{ M_y R \gamma' \cos \alpha + r - \frac{1}{2} [4r^2 - 4\pi^2 R^2(L_1^2 + L_2^2) - L_3^2 R^2(\gamma' - 4\pi)^2]^{\frac{1}{2}} \right\} \sin \gamma' \quad (B-30) \end{aligned}$$

$$z_3' = -M_y R \gamma' \sin \alpha + 2\pi R (K_{1y} + K_{2y}) + K_{3y} R (\gamma' - 4\pi) \quad (B-31)$$

where $L_3 = K_{3y} - K_{3yy}$; $M_3 = K_{3yy} - K_{3zz}$, and the remaining terms and the contribution associated with this remaining portion of the vortex is as calculated before.

The velocity components thus determined are parallel to the XYZ axes. It is usually more convenient to express these components as radial, tangential, and axial velocities, thus

$$u_r = u_x \cos \nu + u_y \sin \nu \quad (B-32)$$

$$v_r = -u_x \sin \nu + \cos \nu = (x^2 + y^2)^{\frac{1}{2}} \cdot \omega_r \quad (B-33)$$

$$w_r = u_z \quad (B-34)$$

For the blade feathering axis, $x = \bar{x}R$ for $0 \leq \bar{x} \leq 1.0$, $y = 0$, $z = (1-\bar{x})R \sin \beta_0$, and the x' , y' , and z' equations are as before. Since $\nu = 0$; $u_x = u_r$; $u_y = \bar{x}R \omega_r$; $u_z = w_r$; and the calculation of the flow field associated with the tip vortex becomes a straightforward, though laborious process. It is somewhat more convenient to make the J's non-dimensional by multiplying both sides of the equations B-10 by R . Thus the graphical integrations will yield $\frac{4\pi R}{x} u_r$, $\frac{4\pi R}{x} v_r$, and $\frac{4\pi R}{x} w_r$. The reason for this will become evident in the succeeding section.

The preceding equations hold equally well for hovering flight as for forward flight.

Approximate Analysis for Contributions Associated with the Vortex Sheet

The motion of the vortex sheet is not known as this aspect of the flow was not investigated. However, since the experimental results already include the effects of the presence of the vortex sheet on the motion of the tip vortex, it is now possible to determine the effect on the vortex sheet that is associated with the tip

vortex and the sheet itself. In this instance, the hovering flight assumption that the position of the outer vortex filaments are independent of the positions of those vortex filaments lying inboard of them but not vice versa is not valid. It is quite apparent that due to the asymmetry of the distribution of vorticity in the wake such an assumption would not be reasonable. It is still possible, however, to calculate the circulation distribution and hence the entire flow field by working inboard along the span in a station-by-station process, and adjusting the outboard stations with each step inboard. About the only reasonable assumption would be to take the stations close enough together so that the strength of the vortex filament shed between stations would be small enough so that the self-associated motion could be neglected. Such an approach should yield reasonably accurate aerodynamic loadings but to attempt to make these calculations without the aid of an electronic computer would be extremely arduous and time consuming.

Qualitatively, it is believed that the sheet shed over the trailing half of the disk, for the most part, moves rapidly down the wake somewhat in the same manner as in the hovering flight case. However, in certain regions of the leading half and trailing half of the disk, it is believed that the sheet moves upward initially and then coming into the flow field associated with the trailing half, passes through the rotor disk plane and then also moves rapidly down the wake. If this flow picture is true, then even an empirical approach to determining the sheet's position will become difficult. In addition, it would seem that a further consequence of this type flow picture would be that in certain areas of the disk, the inplane induced velocities normal to the blade feathering axis would become extremely important. For instance, the measured aerodynamic loadings of references 4 and 6 give no indication of a reversed flow region on the retreating blade. An inplane induced velocity could, among other things, explain the failure of this region to be in evidence.

In view of the preceding short discussion, it is rather obvious that to take the vortex sheet into account in a reasonably accurate manner would present many difficulties and in the end, might not be worth the effort. To include its associated effects in an easy to handle, approximate manner, however, might be well worthwhile. One fairly simple way would be to consider the sheet to be replaced by a series of concentric cylinders of uniform vorticity and to use the method of reference 11. A second way would be to assume that the blade circulation distribution inboard of the maximum point is triangular in form, falling to zero at the blade root. Then assuming that each vortex filament shed from a blade station maintains the same relative position with respect to that station as the tip vortex does with the blade tip, we may use the equations developed for the tip vortex, properly interpreted, to determine the flow field associated with each filament. It is this latter approach that will be dealt with in the following paragraphs. It should be noted that neither of these approximations bear much resemblance with the physical picture, though it is felt that the latter is considerably closer than the former.

Using this latter assumption, once the integrals $\frac{4\pi R}{x} u_T$, $\frac{4\pi R}{x} M_T$, and $\frac{4\pi R}{x} M_T$ have been evaluated and plotted over the entire flow field of the tip vortex, these numerical solutions may be related to each vortex filament in the following manner.

Consider a point $(\frac{x}{R}, \frac{y}{R}, \frac{z}{R})$ in the flow field. Then the contribution associated with the tip vortex may be read directly from the graph or chart. For instance let

$$\frac{4\pi R}{x} u_T = S_1$$

$$\frac{4\pi R}{x} v_T = S_2$$

$$\frac{4\pi R}{x} w_T = S_3$$

For each vortex filament shed at blade station \bar{x}_m , the contributions are read at the point $(\frac{x}{R\bar{x}_m}, \frac{y}{R\bar{x}_m}, \frac{z}{R\bar{x}_m})$ on the same graph but with the opposite sign. For instance let

$$\frac{4\pi R \bar{x}_m N}{x} u_f = -S_{1m}$$

$$\frac{4\pi R \bar{x}_m N}{x} v_f = -S_{2m}$$

$$\frac{4\pi R \bar{x}_m N}{x} w_f = -S_{3m}$$

where $\frac{x}{N}$ is the strength of the filament, assuming that the sheet is approximated by N vortex filaments. The velocity components at the point (x, y, z) for the assumed vorticity distribution are then

$$u = \frac{\sigma c}{4\pi R} \left[S_1 + \frac{1}{N} \sum_i \frac{S_{im}}{\bar{x}_m} \right] \quad (B-35)$$

$$v = \frac{\sigma c}{4\pi R} \left[S_2 + \frac{1}{N} \sum_i \frac{S_{2m}}{\bar{x}_m} \right] \quad (B-36)$$

$$w = \frac{\sigma c}{4\pi R} \left[S_3 + \frac{1}{N} \sum_i \frac{S_{3m}}{\bar{x}_m} \right] \quad (B-37)$$

There still remains the problem of determining the strength of the tip vortex. In the general case, the determination becomes a trial and error process in that it will usually be necessary to assume a value of σc in order to determine the parameters and then to compute σc as a check on this assumed value, ultimately by the equation.

$$\sigma c_m = \frac{1}{2} c \Omega R \left[\bar{x} \left(1 + \frac{\omega}{\Omega} \right) + \mu \cos \gamma \right] c_2 \quad (B-38)$$

Where σc is the maximum value over the blade span if this maximum occurs close to the blade tip. Actually the value of σc_{max} will vary with azimuth position but such a variation is outside the scope of this paper. A good approximation, at least for low values of the advance ratio, would be to determine the steady thrust coefficient and then to read the value of the vortex strength coefficient from figure 5. Remembering that these C_x 's contain the hovering flight parameter A^2 .

Now it is possible to determine the blade spanwise aerodynamic loading by means of the blade element theory. Thus

$$\frac{dT}{dr} = \frac{1}{2} \rho c \Omega^2 R^2 \left[\bar{x} \left(1 + \frac{\omega}{\Omega} \right) + \mu \cos \gamma \right]^2 c_1 \quad (\beta-39)$$

where the inplane component of induced velocity, $\omega R \bar{x}$, has been included for the reason mentioned before, and $c_1 = \alpha_0 - \mu + \Omega R \left[\left(1 + \frac{\omega}{\Omega} \right) + \mu \cos \gamma \right]$ below the stall and c_1 above the stall must be determined from wind tunnel data at the proper Reynold's Number.

Sample Calculation and Discussion

In order to illustrate the results which may be obtained from this semi-empirical approach, the blade spanwise aerodynamic loadings were calculated for the test rotor with the blade in the upwind and downwind positions. The test conditions were as follows: $\theta = 10^\circ$; $\mu_r = 0.05$; $\alpha_s = -4.5^\circ$; the measured wake angle was 45° ; and the measured steady component of the thrust coefficient was 0.00378. The various parameters were measured from the pictures of the flow and the x' , y' , z' , \dot{x}'/dt' , \dot{y}'/dt' , \dot{z}'/dt' , and J 's were calculated in the indicated straightforward manner. However, only the normal component of induced velocity was calculated at the blade feathering axis position across the longitudinal diameter of the tip path plane by means of equation B-10-c. The tip vortex strength coefficient was determined from figure 5 as 0.00600 so that the non-dimensionalizing factor $\frac{R^2}{\Omega t}$ was 2.00. A typical evaluation of the integral for the non-dimensional normal component of induced velocity is given in figure 32 for the center of the disk with the rotor blade in both the upwind and downwind positions. For the upwind position the area under the curve (including an estimate for $\gamma > 1800^\circ$) gave an induced velocity at the center of 6.98 ft/sec; in the downwind position, 7.76 ft/sec, thus showing the periodicity of the flow. (Glauert's value of the induced velocity for this condition is 6.95 ft/sec.) This figure also shows very clearly the contributions to the induced velocity associated with each segment of the tip vortex. The peaks result from the rotor moving forward over the segment of the tip vortex shed over the upwind quadrant of the disk. As the directly upwind segment passes under the center, its contribution of course becomes negative.

Figures 33 and 34 give respectively, the non-dimensional normal component of induced velocity across the longitudinal diameter of the tip path plane when the single blade is in the downwind position and in the upwind position. A comparison is also made with the calculated results of reference 10.

Figure 35 shows the non-dimensional normal component of induced velocity at the blade feathering axis in both the upwind and downwind positions taking into account the contribution associated with the vortex sheet as well as the tip vortex. It will be remembered that the assumption was made that the motion of the vortex filaments with respect to the point at which they were shed was identical, relatively, to the motion of the tip vortex with respect to the blade tip. It is obvious from the calculated results that this, as was noted before, was a poor assumption when viewed from the physical viewpoint, for no allowance was made for negative velocities over the inboard portions of the blade or for the higher positive velocities over the outer portions. About the best that can be said at this point is that this

method of taking the vortex sheet into account is better than none at all.

Figures 36 and 37 show respectively, the calculated blade spanwise aerodynamic loadings of a single blade in the downwind and upwind positions using three different induced velocity distributions. In order to make these calculations, it is necessary to take into account the lateral blade flapping. Since it was not possible to measure any flapping components, nor to predict a sufficiently accurate value, it was decided to calculate the lateral flapping angle which would make the first harmonic thrust moment about the flapping axis zero. It was found that a flapping angle of about one-eighth of a degree would fulfill this requirement.

Since there are no measured pressure distributions for a single-bladed rotor available at these low advance ratios, it is not possible to evaluate the accuracy of the calculated distributions. It will be noted that the three distributions compare in a general way over the upwind blade, but that there is a vast difference over the span of the downwind blade. However, integrating these curves to find the blade thrust shows that the method of this paper, i.e. taking into account both tip vortex and vortex sheet, yields answers that are remarkably close to the measured steady component in both positions while yielding distributions in loading that are appreciably different from each other. The measured steady component of the thrust for this case was 12.1 pounds whereas integration of the downwind calculated loading gives 12.38 pounds and integration of the upwind loading, 11.74 pounds. It would seem that this agreement gives an indication of the validity of the present approach. A more exact determination of the error involved would require pressure distribution measurements over this range of advance ratios.

There are several approximations which may affect the accuracy of the analysis. One of these is the assumption that the strength of the tip vortex is constant with respect to azimuth position in forward flight when it is obvious from the calculated loadings that it is not. This simplification was made in order to limit the scope of the investigation. For example, if the tip vortex is assumed to vary in strength, then the associated radial vortex filaments should also be taken into account. Neglecting one and not the other might yield results of comparable error with that obtained by taking the vortex strength to be constant. A further reason for neglecting this variation at this time was that nothing is known about the rotation of the vortex system about the axis of the wake. Thus a vortex segment of strength \propto shed at $\psi = 0^\circ$ could sometime later have rotated to a position $\pm \psi$. To have determined this rotation would be an investigation in itself. Finally, if the tip vortex strength is taken as constant, then the increments in velocity at a point that are associated with certain segments of the tip vortex will be too small while those increments associated with other segments will be too large and there will be a tendency for the errors to cancel each other.

Another approximation which was made was the use of an average value for the radius of the core of the tip vortex. This value was taken to be about one and one-half percent of the rotor radius. The smoke studies indicated that the radius of the core increased with distance down the wake, but again this area of the investigations was by-passed. However, it is of sufficient importance to warrant further investigations, because an error in the radius of the vortex core can lead to appre-

ciable errors in the calculated velocity components near the vortex. This is particularly important near the blade tip.

The approximate manner in which the vortex sheet was considered also introduces an appreciable error in the values of induced velocity particularly near the center of the rotor. However, since very little thrust is produced over the inboard portion of the blade, this should have little effect on the outer loading or the integrated loading.

Concluding Remarks

A new approach to the problem of the determination of the induced velocities about an isolated rotor in hovering and in forward flight has been investigated. It has been shown that a smoke study of the vortex pattern in the rotor wake can very clearly indicate the complexity of the flow and that from such studies, it is possible to determine the position in space of the tip vortex. Knowing this position and by taking into account the approximate strength and geometry of the vortex sheet shed from the inboard portion of the blade, it is then possible to calculate the blade spanwise aerodynamic loading. The integrated value of this loading curve compared very closely with the steady thrust component. It was concluded that the evaluation of the accuracy of the method must await comparisons with experimental pressure distributions or velocity measurements.

An unexpected forward flight phenomenon was observed at the higher speeds. This phenomenon, as interpreted from the smoke pictures, appeared to involve either a continuous annihilation of the tip vortex filament located at the front of the wake and a turn or two below the disk or a splitting of this filament at the longitudinal plane.

References

1. Gray, Robin B.: A Review of Rotor Induced Velocity Field Theory. Princeton University Aero. Eng. Dept. Report No. 248, Jan. 1954.
2. Gessow, Alfred: Review of Information on Induced Flow of a Lifting Rotor. NACA TN 3238, Aug. 1954.
3. Payne, P. R.: Induced Aerodynamics of Helicopters. Aircraft Engineering, Vol. XXVIII, Nos. 324-327, Feb. - May 1956.
4. Meyer, John R. Jr. and Falabella, Gaetano Jr.: An Investigation of the Experimental Aerodynamic Loading on a Model Helicopter Rotor Blade. NACA TN 2953, May 1953.
5. Nikolsky, A. A. and Gray, Robin B.: Determination of the Effective Axial Induced Flow Pattern through a Helicopter Rotor from Pressure Measurements. Princeton University Aero. Eng. Dept. Report No. 279, Oct. 1954.
6. Falabella, Gaetano Jr. and Meyer, John R. Jr.: Determination of Inflow Distributions from Experimental Aerodynamic Loading and Blade-Motion Data on a Model Helicopter Rotor in Hovering and Forward Flight. NACA TN 3492, Nov. 1955.
7. Rabbott, John P. Jr.: Static-Thrust Measurements of the Aerodynamic Loading on a Helicopter Rotor Blade. NACA TN 3688, July 1956.
8. Heyson, Harry H.: Preliminary Results from Flow-Field Measurements around Single and Tandem Rotors in the Langley Full-Scale Tunnel. NACA TN 3242, Nov. 1954.
9. Heysen, Harry H.: Analysis and Comparison with Theory of Flow-Field Measurements near a Lifting Rotor in the Langley Full-Scale Tunnel. NACA TN 3691, April 1956.
10. Castles, Walter Jr. and De Leeuw, Jacob Henri: The Normal Component of the Induced Velocity in the Vicinity of a Lifting Rotor and Some Examples of Its Applications. NACA TR 1184, 1954.
11. Heyson, Harry H. and Katzoff, S.: Normal Component of Induced Velocity in the Vicinity of a Lifting Rotor with a Nonuniform Disk Loading. NACA TN 3690, April 1956.
12. Goldstein, S.: On the Vortex Theory of Screw Propellers. Proc. Royal Society of London, Ser. A, Vol. 123, No. 792, April 6, 1929, pp 440-465.
13. Lock, C.N.H.: Application of Goldstein's Theory to the Practical Design of Airscrews. British ARC R&M 1377, Nov. 1930.

14. Levy, H. and Forsdyke, A. G.: The Steady Motion and Stability of a Helical Vortex. Proc. Royal Society of London, Ser. A, Vol. 120, 1928, pp 670-690.
15. Hirsch, René: Détermination et Calcul des Hélices D'Avions Optima, Simples, et Coaxiales. Tome I & II. Publications Scientifiques et Techniques du Ministère de L'Air, No. 220, 1944; No. 225, 1949.
16. Kawada, Sandi: Calculation of Induced Velocity by Helical Vortices and Its Application to Propeller Theory. Report of the Aeronautical Research Institute, Tokyo Imperial University, No. 172, Vol XIV, I, Jan. 1939.
17. Lamb, H.: Hydrodynamics. Sixth Edition, Dover Publications (by special arrangement with Cambridge University Press and the Macmillan Co.) 1945, Cap. VII.
18. Gray, Robin B.: On the Motion of the Helical Vortex Shed from a Single-Bladed Hovering Model Helicopter Rotor and Its Application to the Calculation of the Spanwise Aerodynamic Loading. Princeton University, Aero. Eng. Dept. Report No. 313, Sept. 1955.
19. Owen, T. B., Fail, R., and Eyre, R.C.W.: Wind Tunnel Tests on a 6 ft. Diameter Helicopter Rotor. British ARC CP No. 216, May 1955.

TABLE I.
SUMMARY OF DATA ON A SINGLE-BLADED ROTOR IN FORWARD FLIGHT

Date	Record Number	Rotor Number	P	Θ_0	α_{S_0}	Ω	V	μ_V	τ	c_T	Δ	λ_2	K_x	χ	K_{θ^*}	$K_{I_{\theta^*}}$	$K_{J_{\theta^*}}$	$K_{I_{\theta^*}}$	$K_{J_{\theta^*}}$
2/4/66	033534	VIA-1	0.00262	8°	-4.5°	24.6	16.53	0.168	—	0.39	3.6	0.183	78°	0.026	—	—	—	—	
	033535	-2	23.7	20.07	0.176	—	—	—	—	—	—	—	—	—	—	—	—	—	
	033535	-3	27.0	18.55	0.167	—	—	—	—	—	—	—	—	—	—	—	—	—	
	033536	-4	29.2	17.88	0.163	—	—	—	—	—	—	—	—	—	—	—	—	—	
	033536	-5	45.7	6.14	0.0361	—	—	—	—	—	0.61	0.66	37°	0.057	0.11	0.057	0.052	0.057	0.037
	033537	-6	45.8	9.38	0.0588	—	—	—	—	—	0.38	1.28	2.052	0.048	0.012	0.048	0.048	0.034	0.039
2/4/66	033534	-7	45.2	2.48	0.0142	—	—	—	—	—	0.32	0.32	0.0013	13°	0.048	0.014	0.045	0.057	0.058
	033536	-8	44.7	15.73	0.0739	—	—	—	—	—	0.87	1.35	0.098	65°	0.045	0.014	0.036	0.057	0.024
	033536	-9	46.7	17.18	0.0940	—	—	—	—	—	0.97	2.50	0.104	69°	0.018	—	—	—	—
	033547	-1	0.00262	8°	-4.5°	20.1	4.03	0.0632	—	—	0.84	1.68	0.046	83°	0.057	0.011	0.046	0.048	0.035
	033547	-2	28.4	9.89	0.0670	—	—	—	—	—	0.34	0.96	0.102	67°	0.018	—	—	—	—
	033547	-3	42.0	8.96	0.0510	—	—	—	—	—	0.66	4.99	0.067	0.016	0.035	0.015	0.035	0.035	0.032
2/4/66	033547	-4	46.8	6.20	0.0284	—	—	—	—	—	0.38	50°	0.004	0.014	0.043	0.050	0.053	0.053	—
	033548	-5	45.5	2.88	0.0168	—	—	—	—	—	0.81	0.19	0.021	17°	0.052	0.021	0.064	0.067	0.054
	033549	-6	45.3	11.63	0.0411	—	—	—	—	—	0.36	0.86	0.103	70°	0.048	0.016	0.040	0.050	—
	033549	-7	44.6	16.8	0.0941	—	—	—	—	—	0.95	0.86	0.029	—	0.029	—	—	—	—
	033550	-1	0.00262	10°	-4.5°	42.6	14.63	0.0870	—	—	0.85	2.06	0.103	66°	0.052	0.016	0.058	0.060	0.025
	033550	-2	29.9	4.51	0.0430	—	—	—	—	—	0.30	0.41	0.043	34°	0.065	0.013	0.067	0.060	0.041
2/4/66	033550	-3	29.4	9.42	0.0601	—	—	—	—	—	0.35	0.53	0.091	63°	0.037	0.019	0.038	0.038	0.033
	033552	-4	41.3	4.87	0.0283	—	—	—	—	—	0.84	0.25	0.037	50°	—	0.017	0.070	0.053	0.070
	033554	-5	43.0	2.60	0.0161	—	—	—	—	—	0.51	0.23	0.018	27°	0.065	0.022	0.064	0.064	0.048
	033555	-6	48.6	15.33	0.0636	—	—	—	—	—	0.95	0.98	0.018	47°	0.048	0.016	0.046	0.046	0.033
	033556	-7	45.9	8.53	0.0492	—	—	—	—	—	0.35	0.97	0.064	48°	0.060	0.018	0.053	0.050	—
	033571	-1	0.00248	10°	-4.5°	42.9	10.47	0.0610	14.1	0.0036	0.32	0.70	0.076	61°	0.068	0.013	0.064	0.064	0.030
2/6/66	033571	-2	6.01	0.0561	18.9	0.0038	0.91	0.46	0.046	0.046	31°	0.064	0.014	0.073	0.069	0.073	0.039	—	—
	033571	-3	3.11	0.0178	14.1	0.0037	0.80	0.20	0.019	0.019	18°	0.068	0.019	0.061	0.061	0.060	0.046	0.046	—
	033572	-4	6.91	0.0257	15.1	0.0030	0.91	0.56	0.051	0.051	38°	0.064	0.012	0.064	0.064	0.064	0.036	0.036	—
	033576	-1	0.00248	9°	-4.5°	36.9	12.5	0.0348	10.8	0.0040	1.00	1.88	0.119	69°	0.022	0.014	0.034	0.034	0.023
	033577	-2	39.9	3.90	0.0244	10.4	0.0033	0.85	0.20	0.028	23°	0.054	0.014	0.064	0.066	0.064	0.034	0.034	—
	033579	-3	40.4	6.95	0.0450	11.2	0.0034	0.92	0.29	0.047	48°	0.093	0.040	0.027	0.080	0.046	0.046	0.046	—
2/6/66	033581	-4	40.8	12.0	0.0735	12.8	0.0038	0.95	0.59	0.093	64°	0.040	0.017	0.036	0.036	0.036	0.031	0.031	—
	033586	-1	0.00248	8°	-4.5°	37.5	13.2	0.0371	9.8	0.0034	0.99	—	0.100	67°	0.018	0.014	0.036	0.036	—
	033587	-2	40.8	3.50	0.0214	9.8	0.0029	0.94	0.24	0.027	25°	0.046	0.013	0.036	0.036	0.036	0.036	0.036	—
	033589	-3	42.8	9.11	0.0552	11.5	0.0031	0.92	0.34	0.084	50°	0.047	0.013	0.046	0.046	0.046	0.046	0.046	—
	033591	-4	42.4	8.29	0.0508	20.3	0.0029	0.91	0.31	0.039	32°	0.059	0.010	0.040	0.040	0.040	0.040	0.040	—
	033593	-1	0.00248	8°	-4.5°	27.1	17.7	0.1632	6.3	0.0038	0.99	—	0.178	60°	0.018	0.018	0.036	0.036	—
2/6/66	033597	-2	27.6	17.6	0.160	—	—	—	—	—	—	—	—	—	—	—	—	—	
	033599	-3	25.4	17.5	0.170	—	—	—	—	—	—	—	—	—	—	—	—	—	
	033601	-4	23.7	18.80	0.198	—	—	—	—	—	—	—	—	—	—	—	—	—	

TABLE I.
(CONTINUED)

Date	Record Number	Star Number	ρ	θ_0	α_{J}	δ_{J}	γ	μ_{ν}	τ	η_{ν}	λ_2	κ_x	χ	κ_0	$K_{\eta_{\nu}}$	K_{λ_2}	K_{κ_x}	K_{χ}	K_{κ_0}	$K_{\eta_{\nu}}$	K_{λ_2}	K_{κ_x}	K_{χ}	
3/12/66	IHH-0	1	0.002418	8°	-4.5°	40.5	0.00	0.0000	6.3	0.0026	--	--	--	--	0.049	0.014	0.067	0.018	0.026	0.051	0.018	0.064	0.031	
		-1				39.8	3.39	0.0194	6.2	0.0036	0.31	0.23	0.020	21°	0.049	0.014	0.058	0.034	0.012	0.018	0.058	0.031	0.031	
		-2				63.0	6.36	0.0179	10.1	0.0037	0.68	0.42	0.044	57°	0.053	0.009	0.068	0.034	0.012	0.018	0.058	0.031	0.031	
		-3				42.6	10.14	0.0005	10.4	0.0039	0.68	0.73	0.072	64°	0.041	0.010	0.044	0.044	0.009	0.021	0.058	0.031	0.031	
3/12/66	IHH-0	-4				42.1	16.84	0.1060	11.4	0.0032	0.93	1.72	--	76°	0.017	0.017	--	0.017	--	--	0.022	--	--	
		-1	0.002418	9°	-4.5°	45.9	0.00	0.0000	11.6	0.0030	--	--	--	--	--	--	--	--	--	--	--	--	--	--
		-2				43.8	3.48	0.0199	11.6	0.0030	0.80	0.27	0.020	15°	0.061	0.016	0.066	0.016	0.017	0.024	0.057	0.035	0.035	
		-3				59.2	6.16	0.0348	10.0	0.0032	--	--	--	--	--	--	--	--	--	--	--	--	--	--
3/12/66	IHH-0	-4				58.8	13.62	0.0055	11.1	0.0035	0.95	3.26	0.089	68°	0.022	0.014	0.036	0.036	0.015	0.028	0.057	0.035	0.035	
		-1	0.002418	10°	-4.5°	39.2	0.00	0.0000	10.7	0.0036	--	--	--	--	--	--	--	--	--	--	--	--	--	--
		-2				36.1	3.19	0.0044	11.0	0.0036	0.80	0.26	0.027	23°	0.047	0.017	0.061	0.018	0.020	0.026	0.056	0.034	0.034	
		-3				40.0	8.00	0.0000	12.1	0.0039	0.88	0.64	0.056	42°	0.069	0.015	0.059	0.041	0.016	0.021	0.057	0.035	0.035	
4/6/66	IHH-0	-4				40.7	14.60	0.0896	15.3	0.0040	0.98	0.55	0.092	63°	0.018	0.039	--	--	--	--	--	--	--	--
		-1	0.002411	8°	-8.5°	39.2	0.00	0.0000	10.7	0.0036	--	--	--	--	--	--	--	--	--	--	--	--	--	--
		-2				37.4	3.57	0.0238	7.6	0.0023	0.81	0.22	0.024	25°	0.047	0.013	0.053	0.063	0.018	0.021	0.057	0.034	0.034	
		-3				35.6	4.58	0.0320	7.2	0.0028	0.83	0.30	0.037	51°	0.048	0.015	0.056	0.063	0.013	0.019	0.060	0.035	0.035	
4/6/66	IHH-0	-4				36.8	10.70	0.0726	7.6	0.0029	0.86	0.61	0.032	62°	0.033	0.014	0.034	0.034	0.012	0.018	0.059	0.035	0.035	
		-1	0.002411	9°	-8.5°	32.9	2.24	0.0170	6.5	0.0025	0.85	--	0.025	26°	0.042	0.017	0.050	0.050	0.020	0.025	0.063	0.035	0.035	
		-2				36.0	14.33	0.1024	7.6	0.0032	--	--	--	--	--	--	--	--	--	--	--	--	--	
		-3				36.0	14.33	0.1024	7.6	0.0032	--	--	--	--	--	--	--	--	--	--	--	--	--	
4/6/66	IHH-0	-4				36.4	0.00	0.0000	7.4	0.0026	--	--	--	--	--	--	--	--	--	--	--	--	--	
		-1	0.002411	8°	-8.5°	29.2	2.01	0.0172	6.0	0.0030	--	--	--	--	--	--	--	--	--	--	--	--	--	
		-2				34.9	5.55	0.0337	7.7	0.0033	--	--	--	--	--	--	--	--	--	--	--	--	--	
		-3				56.0	10.65	0.0760	6.2	0.0034	--	--	--	--	--	--	--	--	--	--	--	--	--	
4/6/66	IHH-0	-4				36.0	14.33	0.0332	7.6	0.0035	--	--	--	--	--	--	--	--	--	--	--	--	--	
		-1	0.002411	10°	-8.5°	33.7	0.00	0.0000	9.9	0.0031	--	--	--	--	--	--	--	--	--	--	--	--	--	
		-2				56.4	2.58	0.0180	9.5	0.0034	0.81	0.29	0.019	19°	0.053	0.034	0.054	0.054	0.019	0.023	0.061	0.035	0.035	
		-3				35.6	4.95	0.0210	9.7	0.0040	0.85	0.45	0.033	30°	0.054	0.038	0.055	0.055	0.021	0.026	0.060	0.035	0.035	
4/6/66	IHH-0	-4				37.1	9.20	0.0220	10.6	0.0040	0.89	0.68	0.032	52°	0.062	0.047	0.064	0.064	0.022	0.027	0.064	0.035	0.035	
		-1	0.002411	9°	-8.5°	57.2	13.18	0.0365	11.0	0.0041	0.87	0.66	0.034	65°	0.064	0.032	0.065	0.065	0.024	0.029	0.064	0.035	0.035	
		-2				36.6	3.88	0.0260	9.0	0.0035	0.82	--	0.025	22°	0.056	0.035	0.064	0.064	0.025	0.030	0.063	0.035	0.035	
		-3				40.4	18.32	0.1136	14.2	0.0045	--	--	--	--	--	--	--	--	--	--	--	--	--	
4/9/66	IHH-0	-4				38.2	0.00	0.0000	10.0	0.0036	--	--	--	--	--	--	--	--	--	--	--	--	--	
		-1	0.002411	10°	-8.5°	37.7	5.14	0.0208	9.9	0.0036	0.79	0.24	0.022	21°	0.062	0.030	0.063	0.063	0.020	0.025	0.064	0.035	0.035	
		-2				37.9	5.28	0.0348	10.4	0.0037	0.85	0.52	0.032	38°	0.062	0.038	0.064	0.064	0.021	0.026	0.063	0.035	0.035	
		-3				37.9	9.79	0.0245	11.2	0.0040	0.91	0.95	0.041	44°	0.064	0.038	0.065	0.065	0.023	0.028	0.064	0.035	0.035	
4/9/66	IHH-0	-4				37.6	13.20	0.0360	11.1	0.0041	0.87	1.97	0.045	67°	0.061	0.035	0.064	0.064	0.023	0.028	0.064	0.035	0.035	
		-1	0.002411	10°	-8.5°	40.4	18.32	0.1136	14.2	0.0045	--	--	--	--	--	--	--	--	--	--	--	--	--	

TABLE II.
UNREDUCED AND DUPLICATE DATA

Date	Record Number	Run Number	ρ	θ_0	α_s	Ω	V	μ_v	T
2/1/56	03292a	IA-0	0.00255	10°	0.0°	40.7	00.00	0.0000	10.9
	03292b	-1				41.0	5.20	0.0317	---
	03292c	-2				44.1	10.38	0.0588	---
	03292d	-3				39.4	14.43	0.0916	---
	03293	-4				43.8	15.92	0.0908	---
	03294	-5				41.8	2.52	0.0151	---
	03296	-6				44.1	16.50	0.0936	---
	03298	-7				43.3	5.76	0.0333	---
2/1/56	03301	IIA-0	0.00255	9°	0.0°	45.3	00.00	0.0000	11.9
	03302	-1				43.5	3.46	0.0199	---
	03304	-2				43.3	4.53	0.0262	---
	03306	-3				42.2	9.35	0.0654	---
	03309	-4				45.8	12.70	0.0692	---
	03311	-5				48.4	15.88	0.0821	---
2/1/56	03316	IIIA-0	0.00255	8°	0.0°	43.0	00.00	0.0000	9.4
	03318	-1				44.1	2.89	0.0164	---
	03320	-2				42.2	5.08	0.0301	---
	03322	-3				43.1	8.38	0.0485	---
	03324	-4				44.0	14.94	0.0849	---
	03326	-5				48.2	15.77	0.0818	---
3/5/56	03453	IC-0	0.00242	8°	-4.5°	37.4	00.00	0.0000	6.9
	03455	-1				34.9	7.39	0.0530	7.2
	03457	-2				34.6	4.35	0.0314	6.5
	03458	-3				35.2	16.18	0.1160	8.0
	03462	-4				34.4	2.63	0.0191	6.1
	03461	-5				16.2	18.32	0.282	1.2
3/5/56	03465	IIC-0	0.00242	9°	-4.5°	36.3	00.00	0.0000	7.7
	03466	-1				34.1	2.82	0.0206	7.1
	03468	-2				33.7	4.63	0.0344	7.3
	03470	-3				35.4	14.75	0.1042	8.8
3/5/56	03472	IIIC-0	0.00242	10°	-4.5°	39.0	00.00	0.0000	10.2
	03474	-1				37.7	4.95	0.0328	10.4
	03476	-2				34.7	3.91	0.0281	8.9
	03478	-3				36.2	16.45	0.1138	11.0
3/6/56	03487a	ID-0	0.00245	10°	-4.5°	45.0	00.00	0.0000	13.8
	03487b	-1				45.2	4.38	0.0242	14.2
	03487c	-2				43.2	3.60	0.0208	13.0
	03488	-3				46.0	14.17	0.0770	16.5
	03490	-4				45.0	9.44	0.0525	15.2

TABLE II.

(Continued.)

Date	Record Number	Run Number	ρ	θ_0	α_s	Ω	V	M_y	T
3/6/56	03491	IID-0	0.00245	9°	-4.5°	42.3	00.00	0.0000	10.6
	03493	-1				42.6	5.40	0.0316	11.2
	03495	-2				42.4	15.18	0.0895	12.5
	03497	-3				41.5	3.42	0.0206	10.5
	03499	-4				43.0	8.20	0.0476	11.9
3/6/56	03501	IIID-0	0.00245	8°	-4.5°	41.1	00.00	0.0000	8.8
	03503	-1				40.5	3.23	0.0199	9.0
	03504	-2				40.5	6.46	0.0399	9.4
	03506	-3				41.2	12.03	0.0730	10.2
	03508	-4				41.9	16.80	0.1004	10.9
3/8/56	03530	IE-0	0.00245	8°	-4.5°	44.1	00.00	0.0000	10.5
	03532	-1				39.6	3.82	0.0241	8.7
	03534	-2				42.3	5.54	0.0328	10.0
	03536	-3				42.0	11.60	0.0690	11.0
	03538	-4				42.6	15.20	0.0891	11.1
3/8/56	03540	IIE-0	0.00245	9°	-4.5°	41.4	00.00	0.0000	10.2
	03542	-1				41.1	4.61	0.0280	10.6
	03544	-2				41.0	6.77	0.0413	10.7
	03546	-3				41.6	14.20	0.0852	11.7
	03548	-4				42.0	17.28	0.1029	12.4
3/8/56	03550	IIIE-0	0.00245	10°	-4.5°	40.3	00.00	0.0000	11.0
	03552	-1				40.2	3.20	0.0199	10.8
	03554	-2				40.3	7.29	0.0452	11.3
	03556	-3				40.7	12.92	0.0794	12.2
	03558	-4				42.2	17.92	0.1062	13.5
	03567	-5				41.5	7.68	0.0463	11.8
3/9/56	---	IF-0	0.00246	11.5°	-4.5°	34.3	00.00	0.0000	9.3
	---	-1				32.9	4.13	0.0314	9.0
	---	-2				35.5	6.35	0.0447	10.4
	---	-3				35.6	12.43	0.0873	10.8
	---	-4				35.3	15.20	0.1076	9.9
3/9/56	---	IIF-I	0.00246	10°	-4.5°	36.8	4.11	0.0279	9.0
	---	-2				37.5	2.34	0.0156	9.0
	---	-3				39.0	12.39	0.0790	11.1
	---	-4				39.5	16.98	0.1074	11.6
3/9/56	---	IIIF-1	0.00246	9°	-4.5°	44.4	3.88	0.0218	10.0
	---	-2				41.4	7.82	0.0472	10.3
	---	-3				42.8	13.95	0.0815	10.8
	---	-4				40.0	17.98	0.1124	10.3

TABLE II.

(Continued.)

Date	Record Number	Run Number	ρ	θ_0	α_s	Ω	τ	μ_y	T
3/9/56	---	IVF-1	0.00246	8°	-4.5°	43.1	3.66	0.0212	8.8
	-2					43.5	9.46	0.0545	9.8
	-3					41.0	13.03	0.0795	9.5
3/10/56	---	IG-1	0.00240	8°	-4.5°	44.5	8.13	0.0456	---
	-2					42.8	3.12	0.0182	---
	-3					41.4	6.05	0.0366	---
	-4					41.1	12.77	0.0775	---
	-5					42.3	17.53	0.1037	---
3/10/56	---	IIG-1	0.00240	9°	-4.5°	40.7	3.24	0.0192	---
	-2					40.7	5.99	0.0368	---
	-3					34.4	9.54	0.0693	---
	-4					41.3	12.61	0.0763	---
	-5					38.3	17.42	0.1137	---
3/10/56	---	IIIG-1	0.00240	10°	-4.5°	39.9	4.29	0.0269	---
	-2					40.5	5.60	0.0346	---
	-3					41.1	9.68	0.0589	---
	-4					38.8	17.95	0.1157	---
	-5					40.9	13.52	0.0825	---
4/2/56	03919	II-0	0.00244	10°	-4.5°	39.9	00.00	0.0000	---
	03920	-1				43.0	3.36	0.0195	---
	03923	-2				38.6	4.97	0.0322	---
	03925	-3				39.8	9.12	0.0573	---
	03927	-4				38.7	15.61	0.1008	---
	03929	-5				40.5	6.81	0.0420	---
	03931	-6				39.8	3.46	0.0217	---
4/2/56	03933	III-1	0.00244	9°	-4.5°	35.8	15.00	0.1048	---
	03935	-2				38.6	2.92	0.0189	---
	03937	-3				39.1	4.62	0.0296	---
	03939	-4				39.4	7.48	0.0475	---
4/2/56	03941	IIII-1	0.00244	8°	-4.5°	38.2	16.00	0.1047	---
	03944	-2				36.6	3.55	0.0242	---
	03947	-3				37.1	4.73	0.0319	---
	03949	-4				37.2	8.34	0.0560	---
	03951	-5				36.9	6.73	0.0455	---
4/3/56	03967	IJ-0	0.00242	8°	-4.5°	41.5	00.00	0.0000	---
	03976	-1				39.8	2.65	0.0166	---
	03978	-2				38.7	4.31	0.0278	---
	03980	-3				41.4	8.80	0.0532	---
	03982	-4				38.6	12.52	0.0810	---

TABLE II.

(Continued.)

Date	Record Number	Run Number	ρ	θ_0	α_s	Ω	v	μ_y	T
4/3/56	03984	IIJ-1	0.00242	9°	-4.5°	40.6	3.32	0.0204	---
	03986	-2				41.1	5.32	0.0324	---
	03988	-3				40.8	7.61	0.0466	---
	03990	-4				41.7	14.72	0.0881	---
4/3/56	03992	IIIJ-1	0.00242	10°	-4.5°	35.7	3.04	0.0213	---
	03995	-2				37.8	6.22	0.0411	---
	03996	-3a				38.0	10.27	0.0675	---
	03997	-3b			+4.5°	36.4	43.81	0.0262	---
	03999	-4			-4.5°	39.4	16.93	0.1074	---
4/3/56	---	IVJ-1	0.00242	10°	-4.5°	--	--	--	---
	---	-2				--	--	--	---
	04009	-3				40.3	6.42	0.0398	---
4/4/56	04025	IK-0	0.00236	10°	-4.5°	42.4	00.00	0.0000	---
	04027	-1				14.3	19.61	0.343	1.7
	04028	-2				23.0	19.52	0.212	4.7
	04030	-3				28.1	20.87	0.1858	6.9
	04032	-4				34.2	18.24	0.1333	10.3
	04034	-5				32.4	3.09	0.0239	7.3
	04035	-6				36.5	11.45	0.0785	9.0
	04037	-7			+4.5°	35.4	6.08	0.0430	8.0
4/4/56	04039	IIK-1	0.00236	9°	-4.5°	34.4	7.31	0.0532	7.3
	04041	-2			+4.5°	37.4	5.43	0.0363	8.9
	04043	-3			-4.5°	18.0	22.23	0.309	2.5
	04045	-4				24.4	20.50	0.210	4.4
4/4/56	---	IIIK-1	0.00236	8°	-4.5°	35.3	8.68	0.0615	7.4
	---	-2			+4.5°	31.2	6.21	0.0496	7.2
	04051	-3			-4.5°	18.2	21.10	0.290	---
	04054	-4				27.3	20.74	0.1900	4.0
	04057	-5				34.8	2.86	0.0205	6.0
	04059	-6				36.4	21.2	0.1456	8.5
4/6/56	04161	IM-0	0.00240	10°	-8.5°	36.8	00.00	0.0000	9.1
	04164	-1				36.3	3.63	0.0250	9.2
	04166	-2				35.8	8.71	0.0610	9.8
	04168	-3				22.8	--	--	3.5
	04170	-4				27.5	--	--	5.3
4/6/56	04172	IIM-1	0.00240	9°	-8.5°	34.0	2.70	0.0199	6.8
	04175	-2				34.7	7.13	0.0514	7.5
	04177	-3				38.5	19.4	0.126	9.9
	04179	-4				22.2	20.8	0.244	2.8
	04182	-5				28.9	19.62	0.1700	5.0

TABLE II.

(Continued.)

Date	Record Number	Run Number	ρ	θ_0	α_S	Ω	v	μ_v	T
4/6/56	04184	IIIM-1	0.00240	8°	-8.5°	36.1	2.54	0.0176	7.0
	04186	-2				37.5	9.62	0.0641	7.8
	04188	-3				34.4	15.00	0.1089	6.8
	04190	-4				22.8	19.58	0.2143	2.8
	04192	-5				30.6	18.83	0.154	5.8
	04194	-6				36.9	5.30	0.0359	7.2
4/7/56	04218	IMa-0	0.00241	8°	-8.5°	40.6	00.00	0.0000	8.3
	04219	-1				40.8	4.20	0.0257	8.7
	04220	-2				39.7	2.05	0.0129	7.9
	04221	-3				41.7	6.23	0.0373	9.1
	04223	-4				38.6	11.89	0.0770	8.1
	04225	-5				41.5	16.00	0.0964	10.4
	04227	-6				38.2	17.30	0.1132	9.1
	04229	-7				26.0	19.60	0.1885	4.2
	04231	-8				34.6	20.00	0.1445	7.5
4/7/56	04233	IIMa-0	0.00241	9°	-8.5°	38.6	00.00	0.0000	8.7
	04234	-1				38.2	3.46	0.0220	8.6
	04235	-2				38.1	5.44	0.0357	9.1
	04236	-3				38.3	9.00	0.0588	9.7
	04238	-4				38.8	6.71	0.0433	9.9
	04239	-5				36.2	14.51	0.1002	9.3
	04240	-6				39.4	18.91	0.120	10.1
	04242	-7				24.0	18.69	0.1951	3.9
	04244	-8				31.6	19.90	0.1574	6.6
4/7/56	04247	IIIMa-0	0.00241	10°	-8.5°	37.7	00.00	0.0000	9.6
	04248	-1				39.6	2.36	0.0150	10.4
	04249	-2				39.7	5.05	0.0318	10.8
	04250	-3				39.8	6.61	0.0416	11.5
	04252	-4				43.6	8.05	0.0461	13.4
	04253	-5				43.9	13.34	0.0760	14.4
	04255	-6				40.8	19.20	0.1175	12.4
	04257	-7				23.4	19.87	0.2118	3.9
	04259	-8				32.6	18.80	0.1440	7.9
4/10/56	04350	10-0	0.00242	8°	-0.5°	38.9	00.00	0.0000	7.7
	04352	-1				38.6	12.06	0.0781	9.6
	04354	-2				35.4	14.38	0.1016	8.8
	04356	-3				35.9	19.92	0.1388	9.8
	04358	-4				18.2	21.60	0.297	2.7
	04360	-5				26.0	20.67	0.1847	6.2
4/10/56	04376	IIO-0	0.00242	9°	-0.5°	36.6	00.00	0.0000	7.9
	04362	-1				18.3	19.97	0.2727	3.6
	04365	-2				30.6	20.37	0.1662	7.9

TABLE II.
(Concluded.)

Date	Record Number	Run Number	ρ	θ_e	α_s	Ω	v	μ_v	T
4/10/56	04367	II0-3	0.00242	9°	-0.5°	36.8	21.28	0.1447	10.8
	04369	-4				17.9	22.2	0.310	2.3
	04372	-5				37.2	15.75	0.1058	10.1
4/10/56	04378	II10-0	0.00242	10°	-0.5°	38.8	00.00	0.0000	10.2
	04380	-1				15.5	20.97	0.338	2.7
	04382	-2				27.0	21.1	0.196	6.8
	04385	-3				36.3	21.6	0.148	11.3
	04387	-4				18.8	21.4	0.285	2.5
	04389	-5				36.6	16.21	0.1107	11.7
	04391	-6				35.8	7.29	0.0509	8.6
4/11/56	04416	IP-0	0.00244	10°	-0.5°	34.4	00.00	0.0000	8.0
	04418	-1				37.2	3.15	0.0212	10.2
	04420	-2				37.2	5.30	0.0356	9.8
	04422	-3				36.7	7.57	0.0516	9.8
	04424	-4				36.6	12.18	0.0831	10.5
	04426	-5				38.5	17.18	0.1115	12.3
4/11/56	04428	IIP-0	0.00244	9°	-0.5°	38.5	00.00	0.0000	9.3
	04429	-1				37.6	3.39	0.0225	8.9
	04431	-2				35.0	5.75	0.0410	7.8
	04433	-3				38.4	9.38	0.0610	9.9
	04435	-4				36.1	12.76	0.0883	9.3
	04437	-5				36.0	16.02	0.1115	9.6
4/13/56	04439	IIIP-0	0.00244	8°	-0.5°	34.0	00.00	0.0000	5.8
	04440	-1				32.6	2.73	0.0210	6.0
	04442	-2				35.6	4.70	0.0330	6.8
	04444	-3				36.1	8.99	0.0622	8.0
	04446	-4				37.1	13.36	0.0900	9.5
	04448	-5				36.9	17.22	0.1165	9.5
4/9/56	---	IIN-1	0.00241	9°	-0.5°	34.9	3.14	0.0225	7.6
	---	-2				38.2	4.72	0.0310	9.0
	---	-3				38.5	9.18	0.0596	10.0
	---	-4				39.0	12.80	0.0820	10.7
	---	-5				39.6	16.02	0.1012	11.5
4/9/56	---	IIIN-1	0.00241	8°	-0.5°	36.1	2.88	0.0200	7.1
	---	-2				36.4	4.59	0.0315	7.2
	---	-3				37.0	8.04	0.0543	8.2
	---	-4				37.6	13.07	0.0869	9.9
	---	-5				38.6	18.13	0.1174	11.3

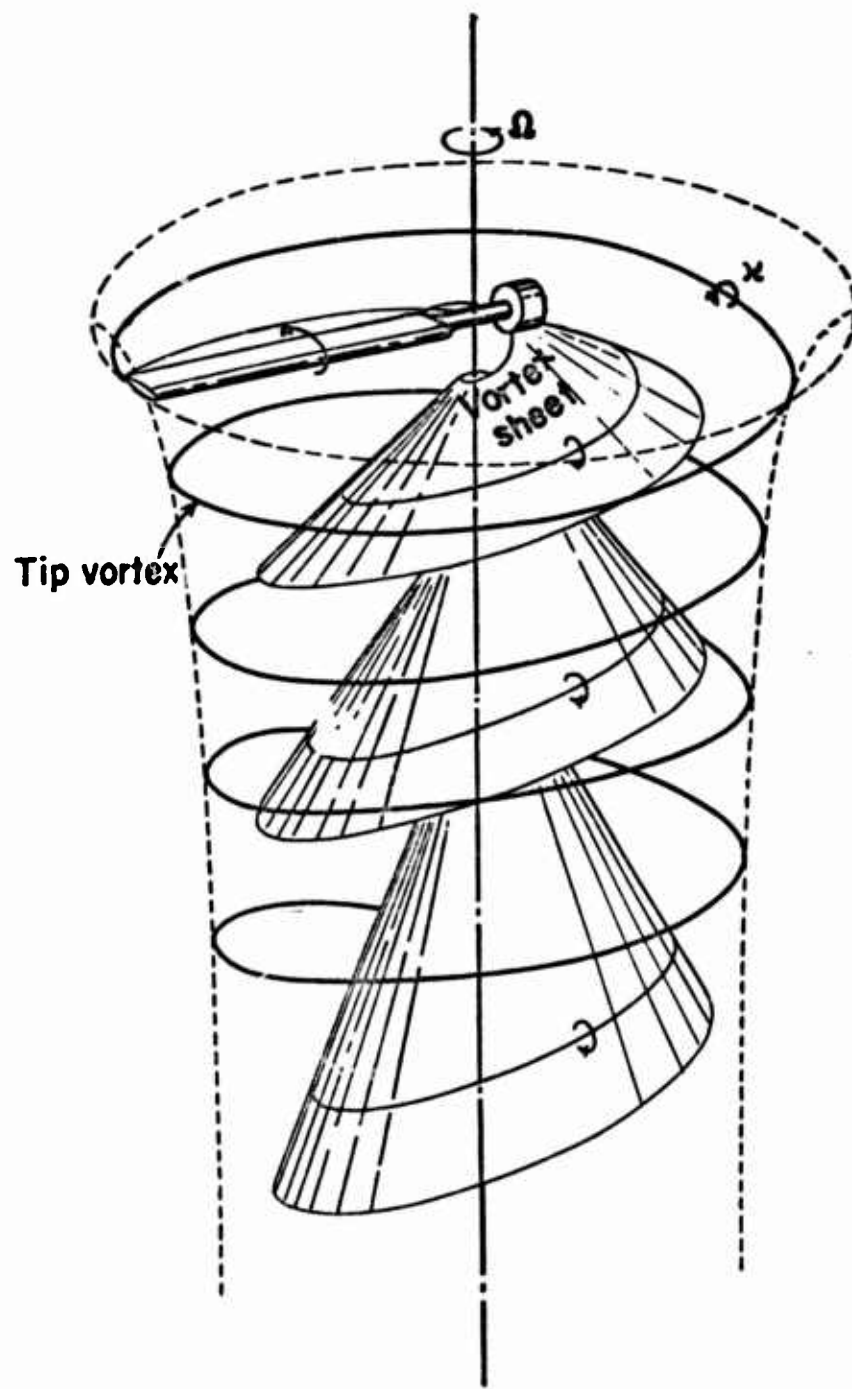


Figure 1. The vortex pattern in the wake of a single-bladed hovering helicopter rotor as obtained from smoke studies.

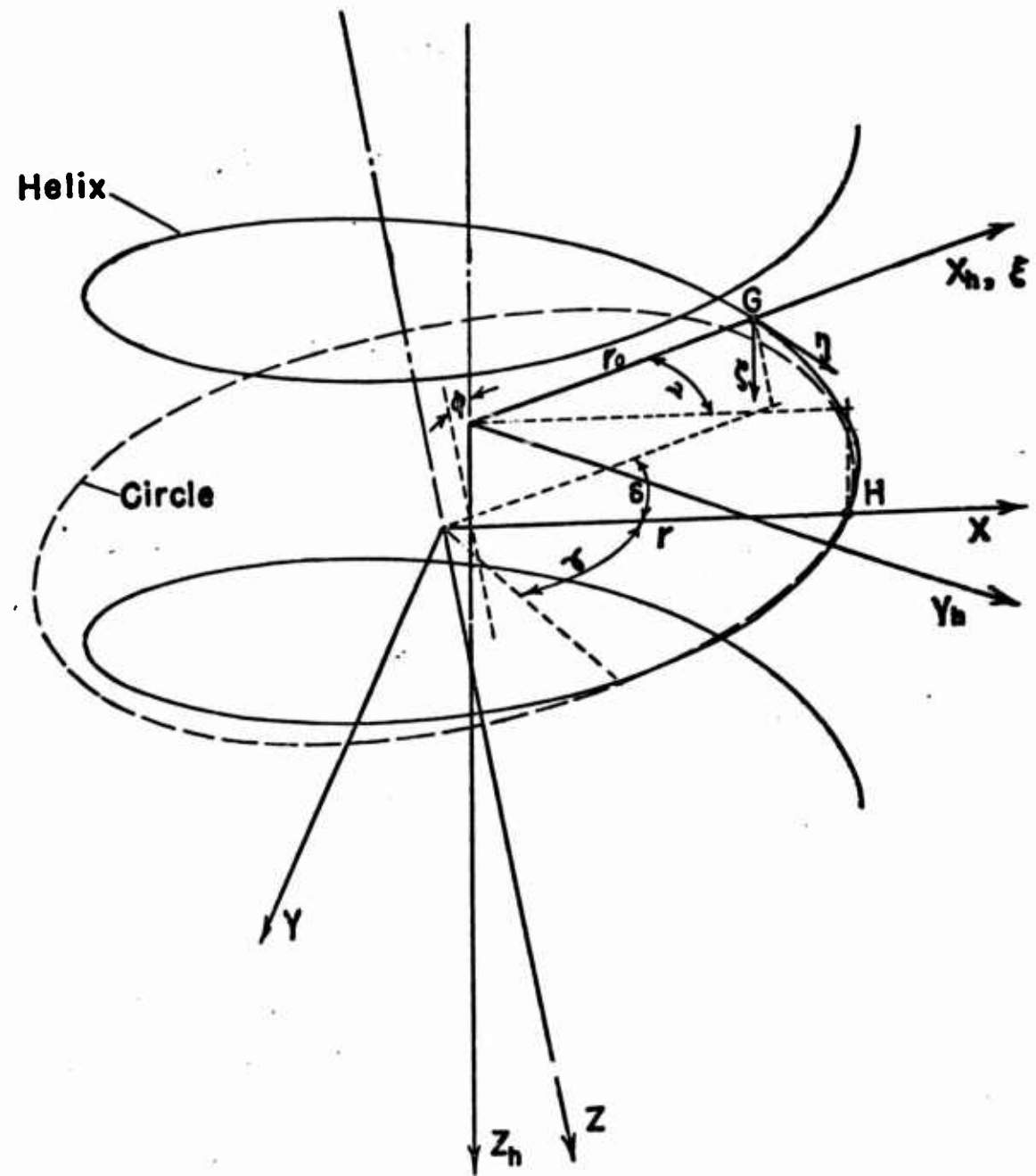


Figure 2. Coordinate system used in hovering flight analysis.

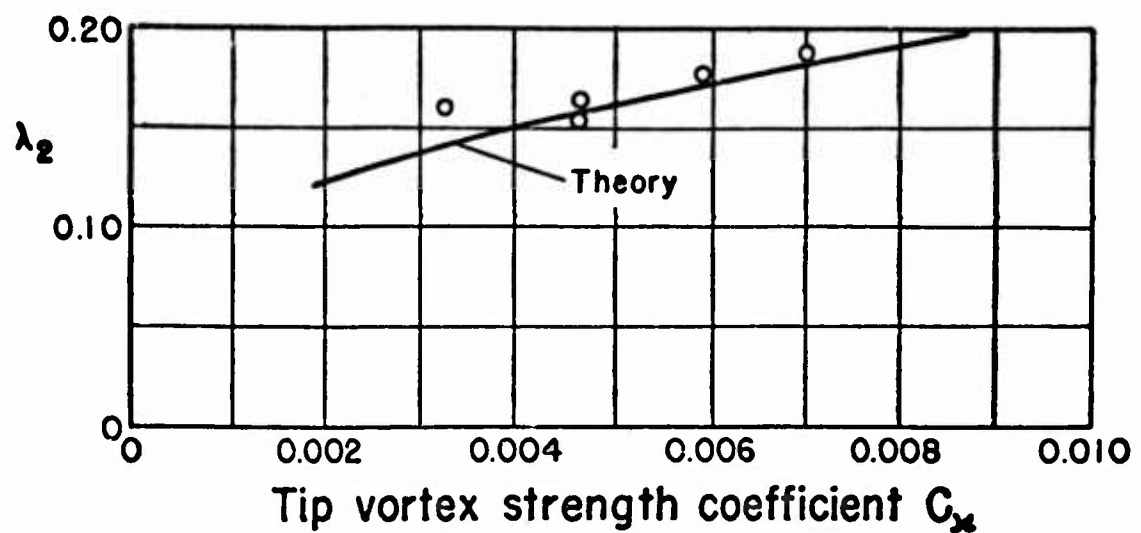


Figure 3. Comparison of the theoretical and experimental values of the wake contraction exponent, λ_2 , for a single-bladed hovering model rotor.

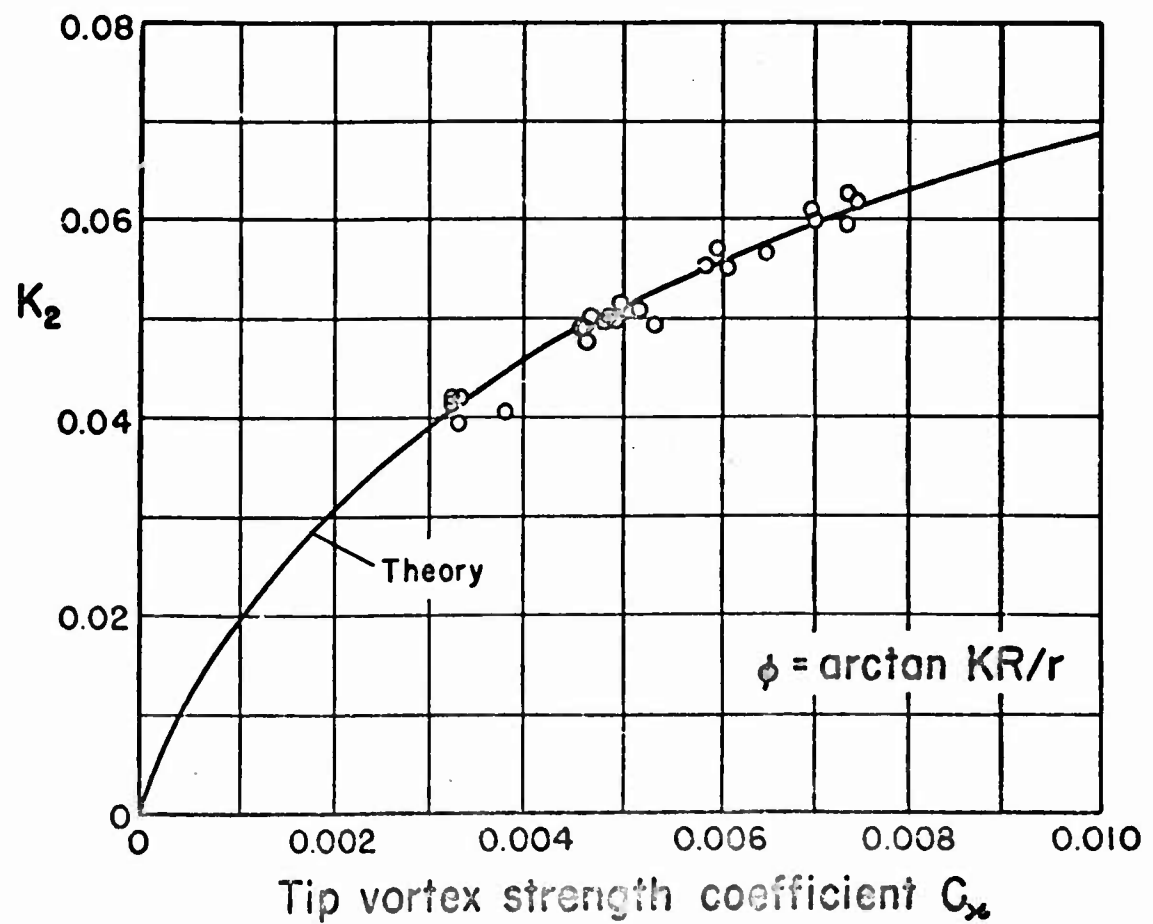


Figure 4. Comparison of the theoretical and experimental values of the ultimate wake helix pitch angle parameter, K_2 , for a single-bladed hovering model rotor.

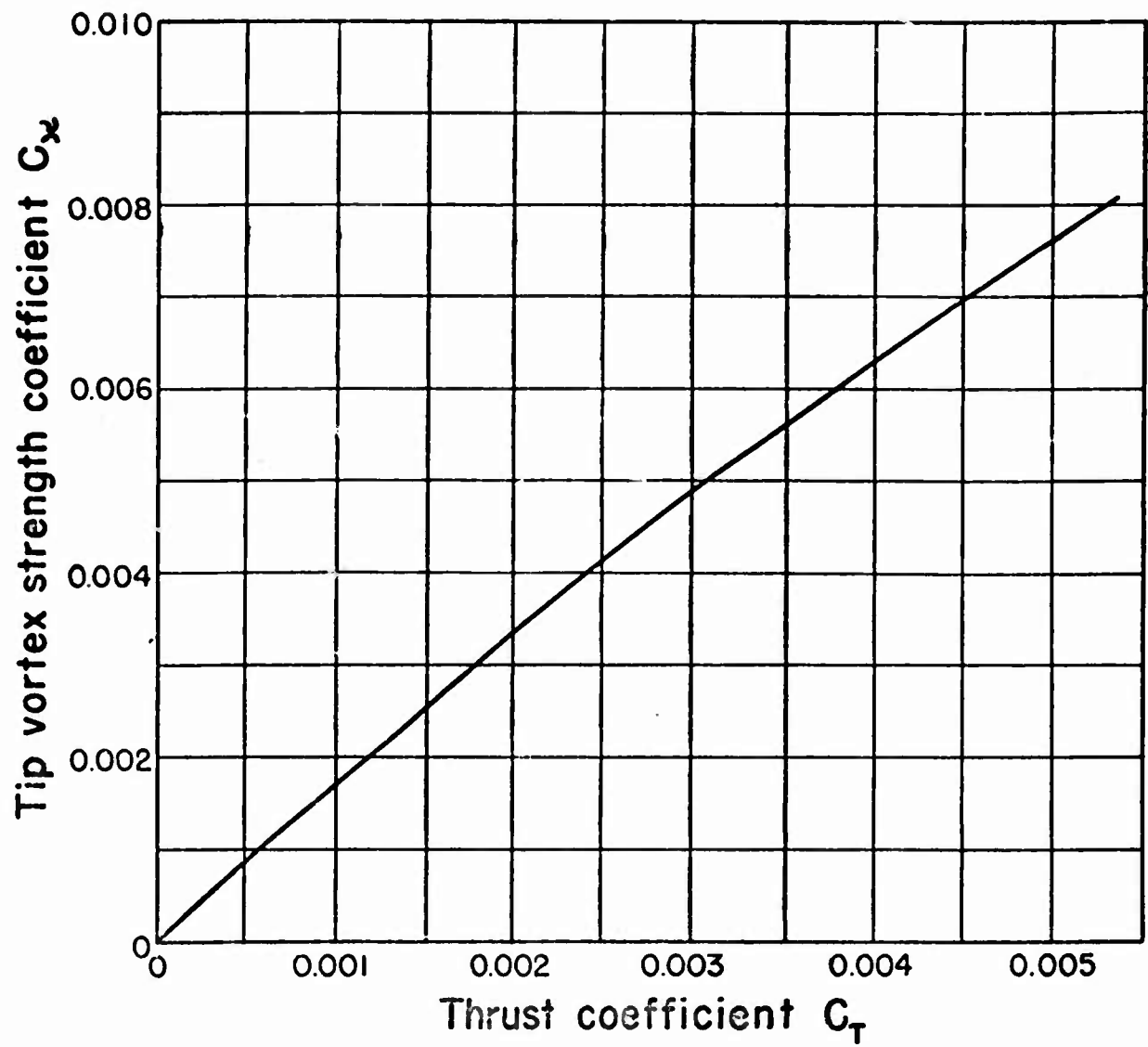


Figure 5. Theoretical variation of the tip vortex strength coefficient versus thrust coefficient of a single-bladed hovering model rotor.

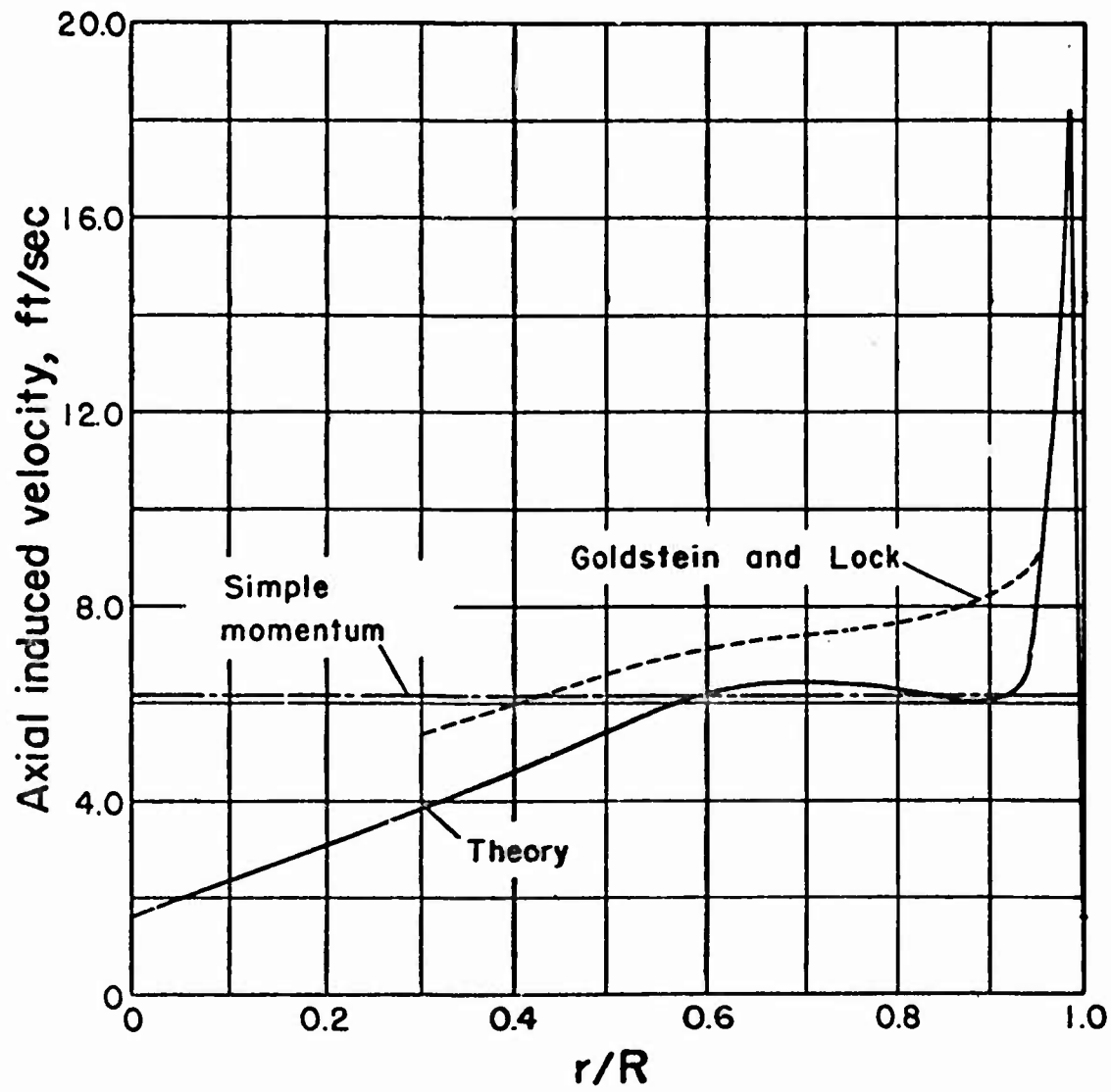


Figure 6. Calculated axial induced velocity at the blade feathering axis of a single-bladed hovering model rotor. $C_t = 0.00260$

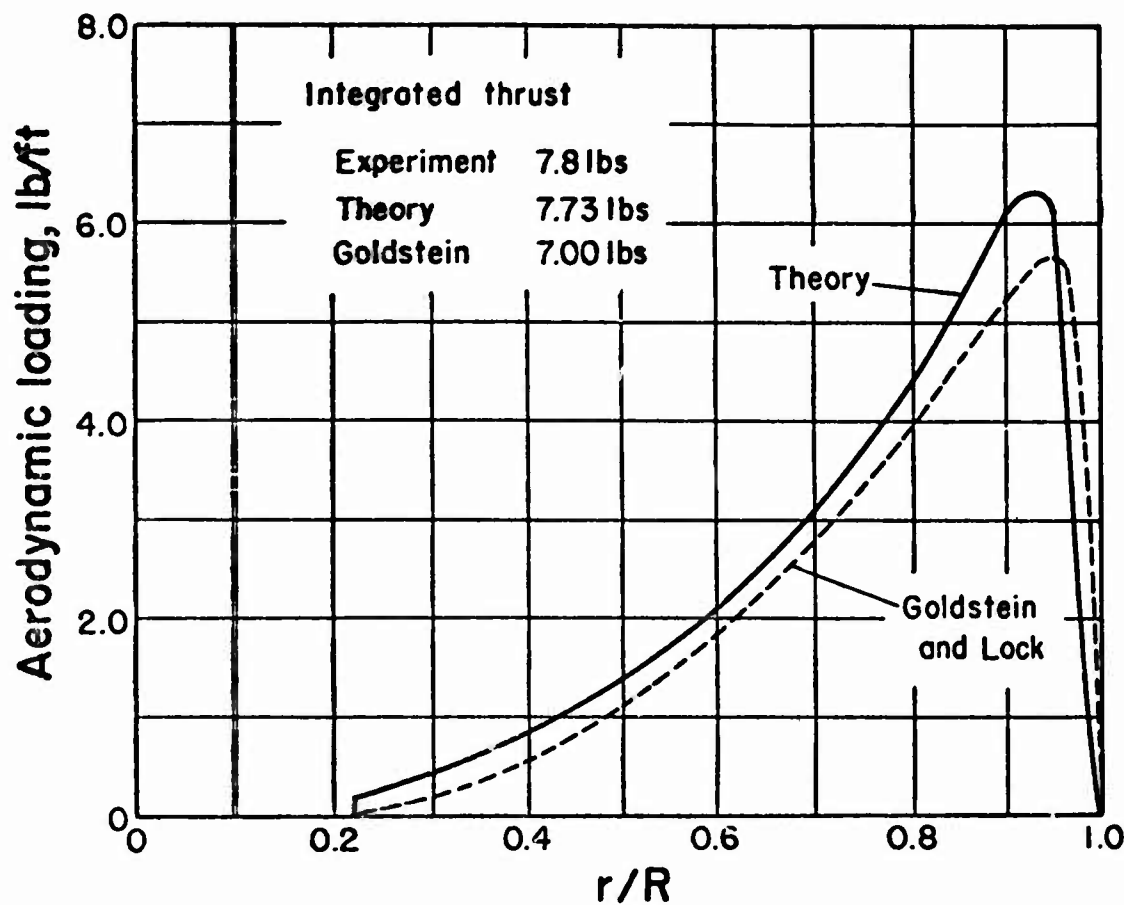


Figure 7. Calculated spanwise aerodynamic loading of a single-bladed hovering model rotor. $C_T = 0.00280$; $\theta_e = 8.5^\circ$

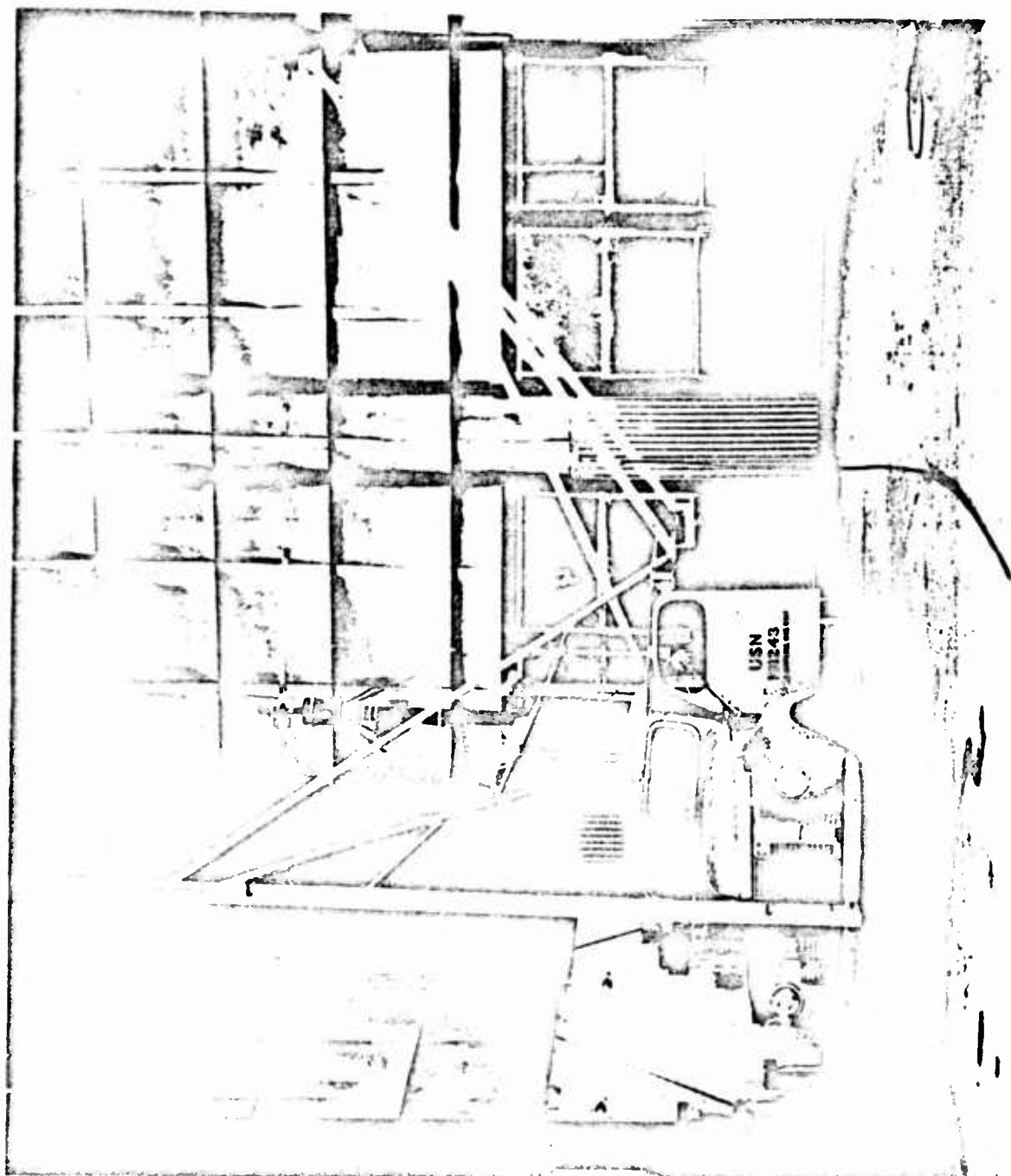


Figure 9. Apparatus used in the forward flight investigation.

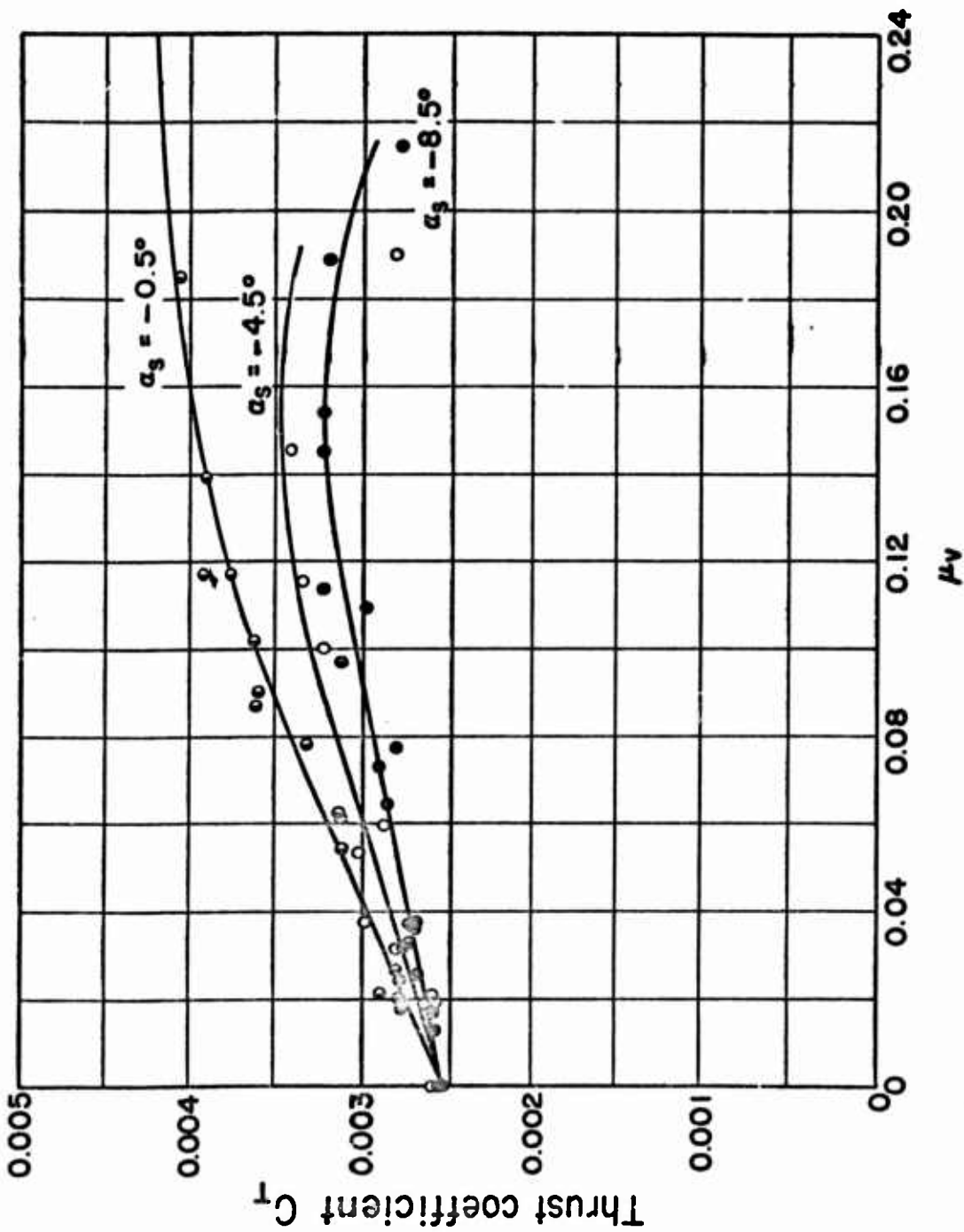


Figure 9. Experimental variation of thrust coefficient with advance ratio and shaft angle of attack for a single-bladed rotor in low speed forward flight. $\theta_0 = 8.0^\circ$.

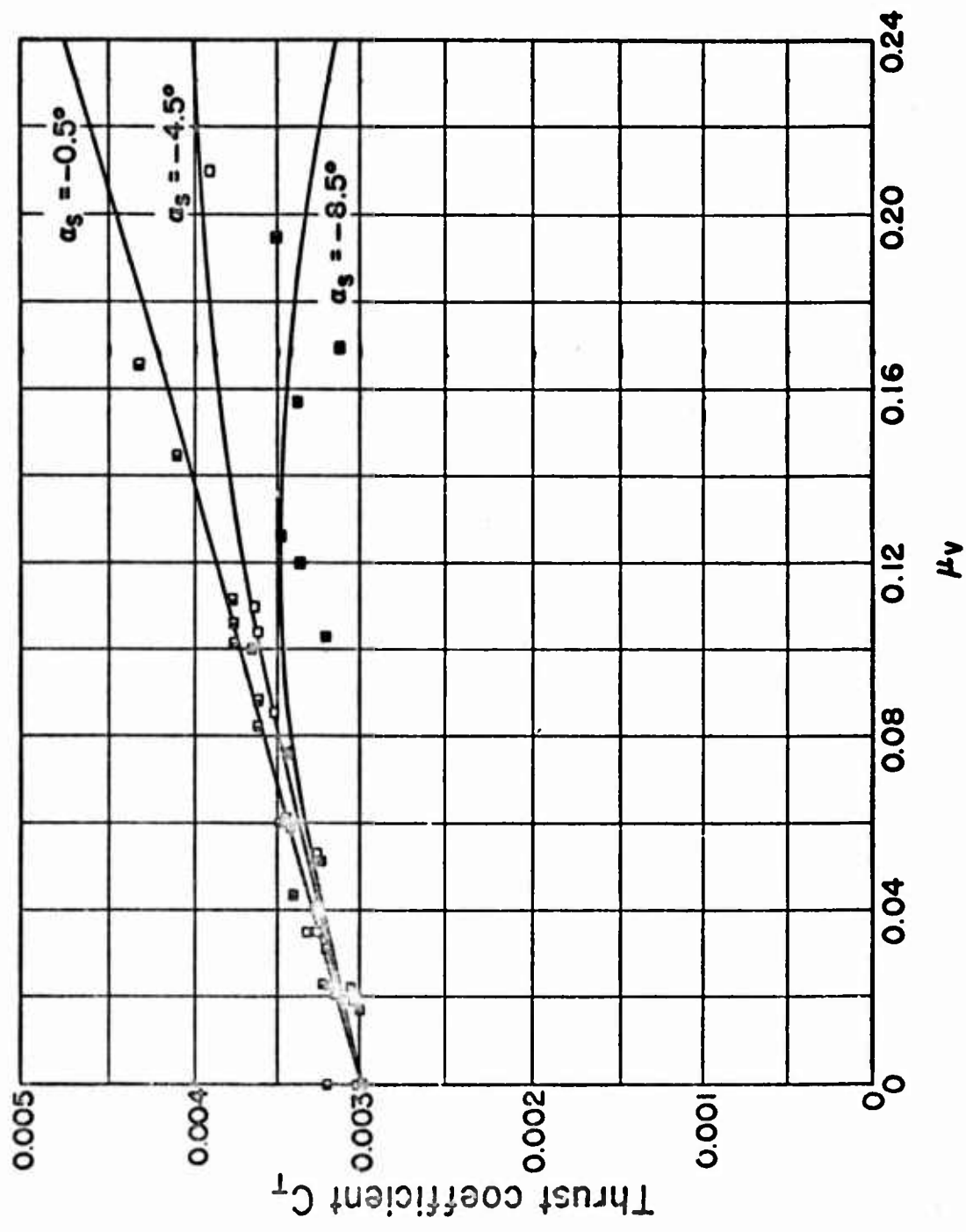


Figure 10. Experimental variation of thrust coefficient with advance ratio and shaft angle of attack for a single-bladed rotor in low speed forward flight. $\theta_0 = 9.0^\circ$

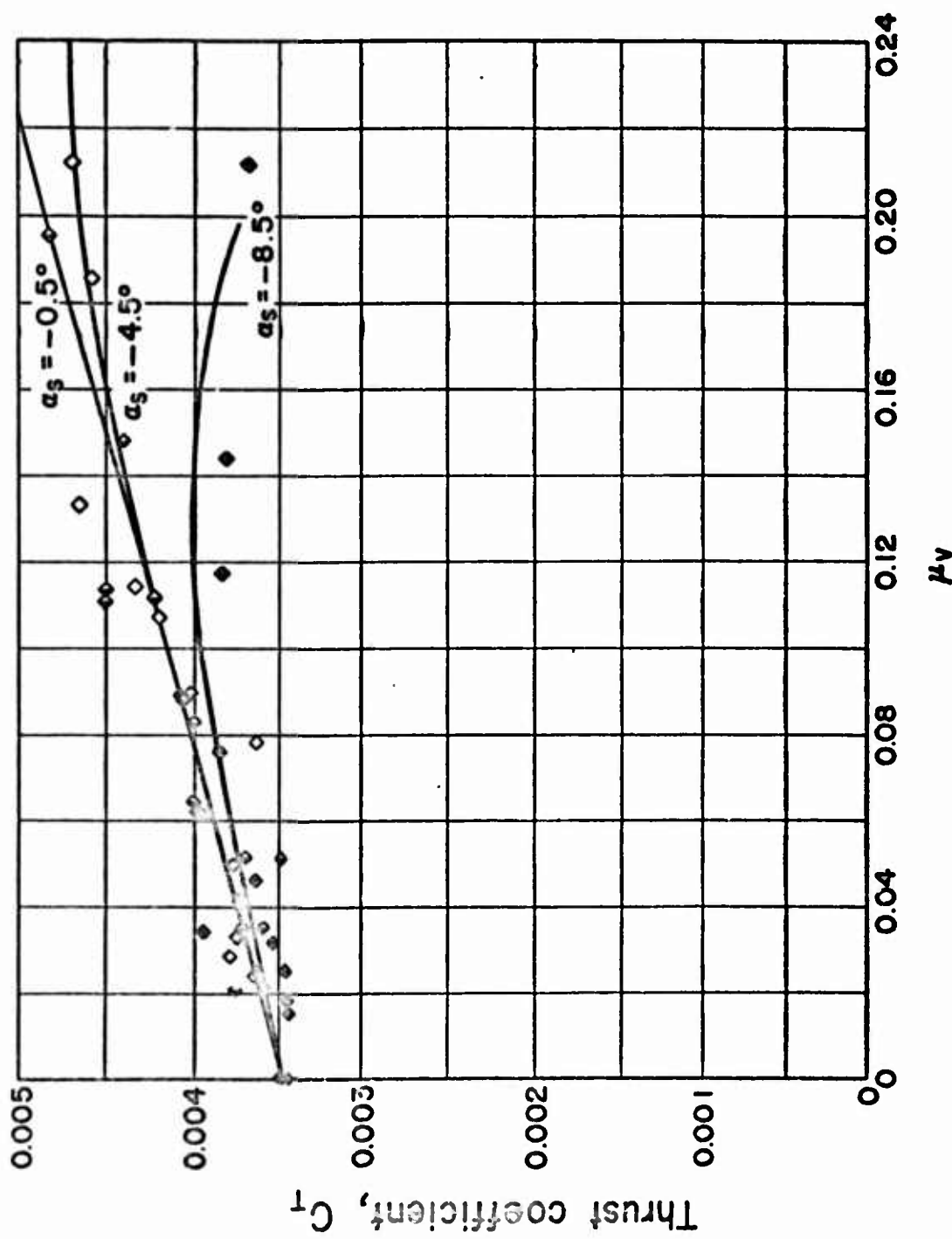


Figure 11. Experimental variation of thrust coefficient with advance ratio and shaft angle of attack for a single-bladed rotor in low speed forward flight. $\theta_0 = 10.0^\circ$

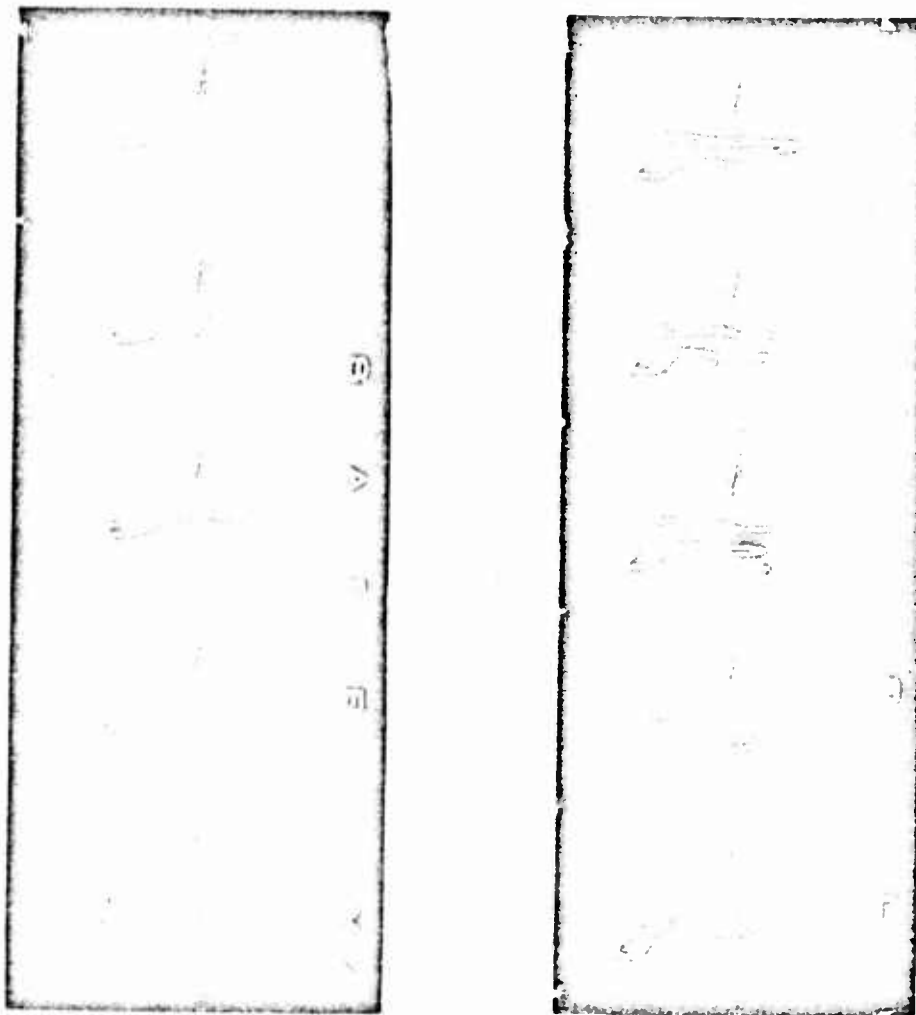


Figure 12. Typical side view of the vortex shed from the tip of a single-bladed rotor in low speed forward flight.
Time between frames about 0.0164 seconds. Run No. IH-3.
Blade moving out of picture in forward position.

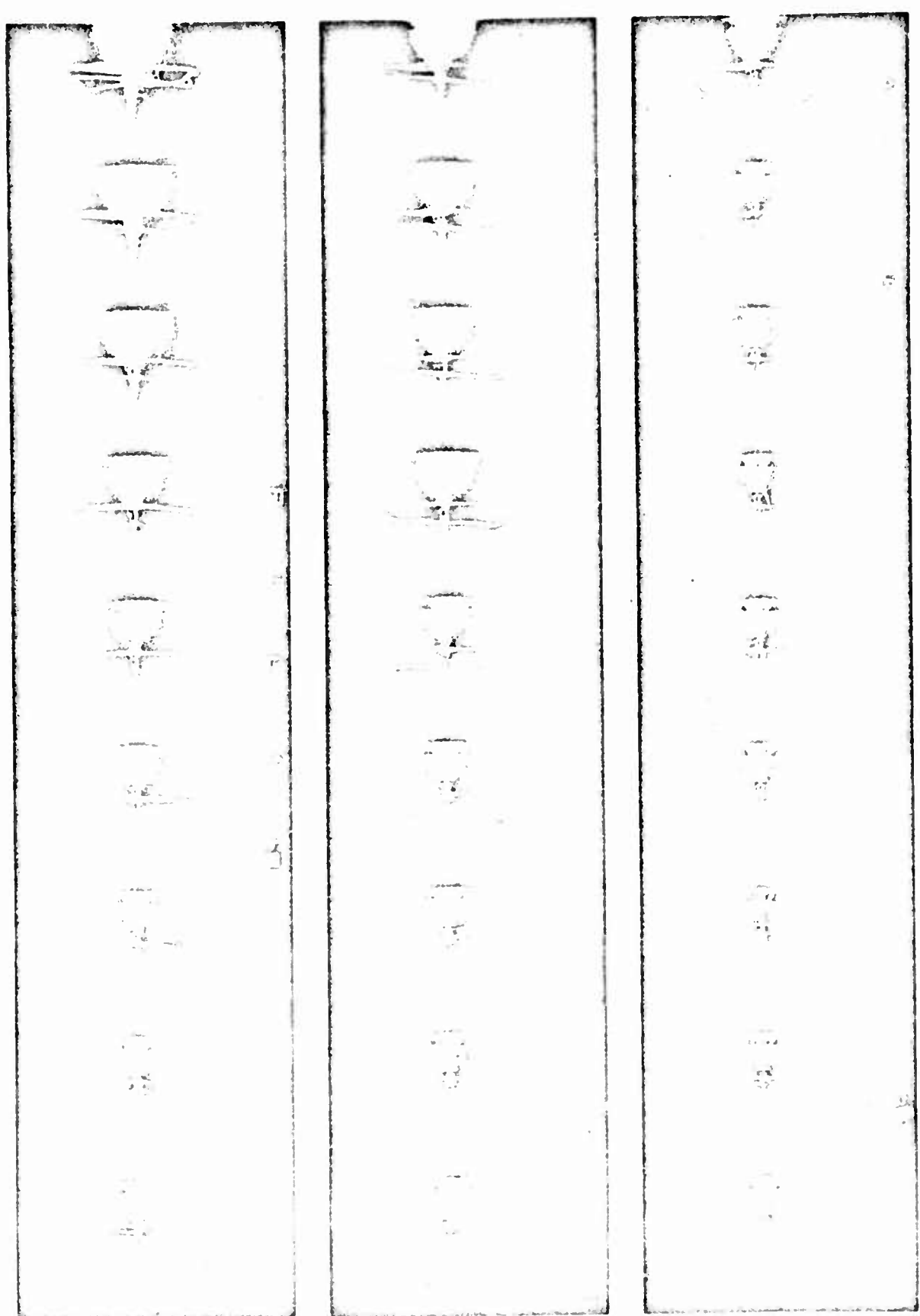


Figure 13. Typical front view of the vortex shed from the tip of a single-bladed rotor in low speed forward flight showing separation of the vortex at the forward longitudinal plane. Time between frames about 0.0164 seconds. Run No. 1F-3. Blade moving from right to left across front of picture.

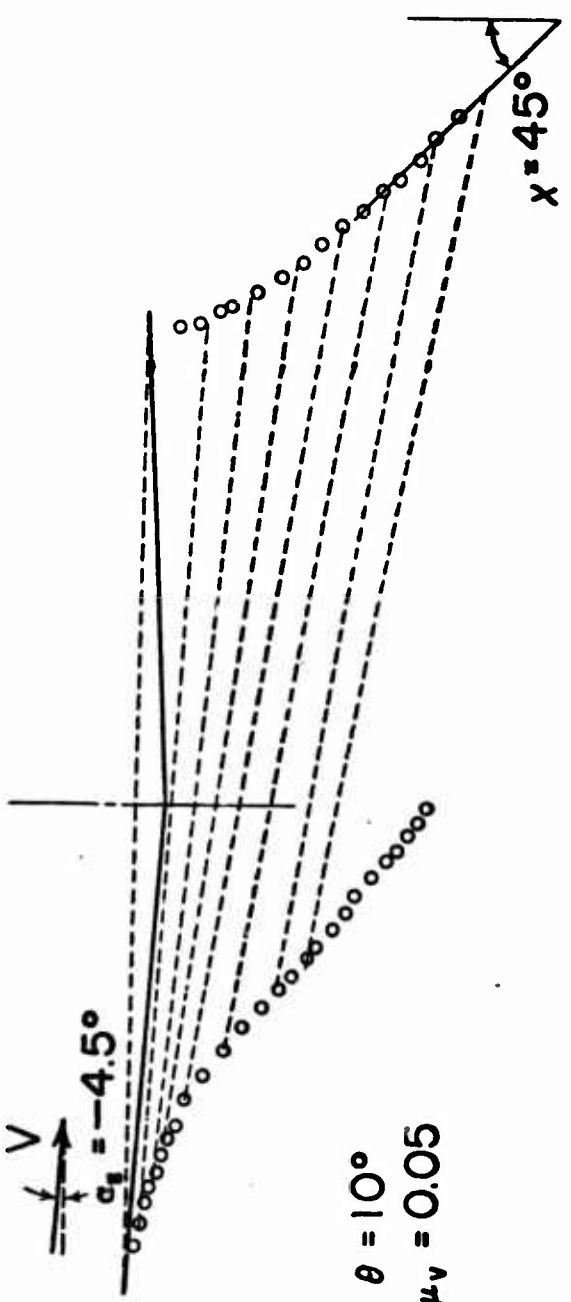


Figure 14. Longitudinal tilt back of the circular cross-sections of the wake of a single-bladed rotor in low speed forward flight. Dashed lines show the intersections of the circular cross-sections with the longitudinal plane.

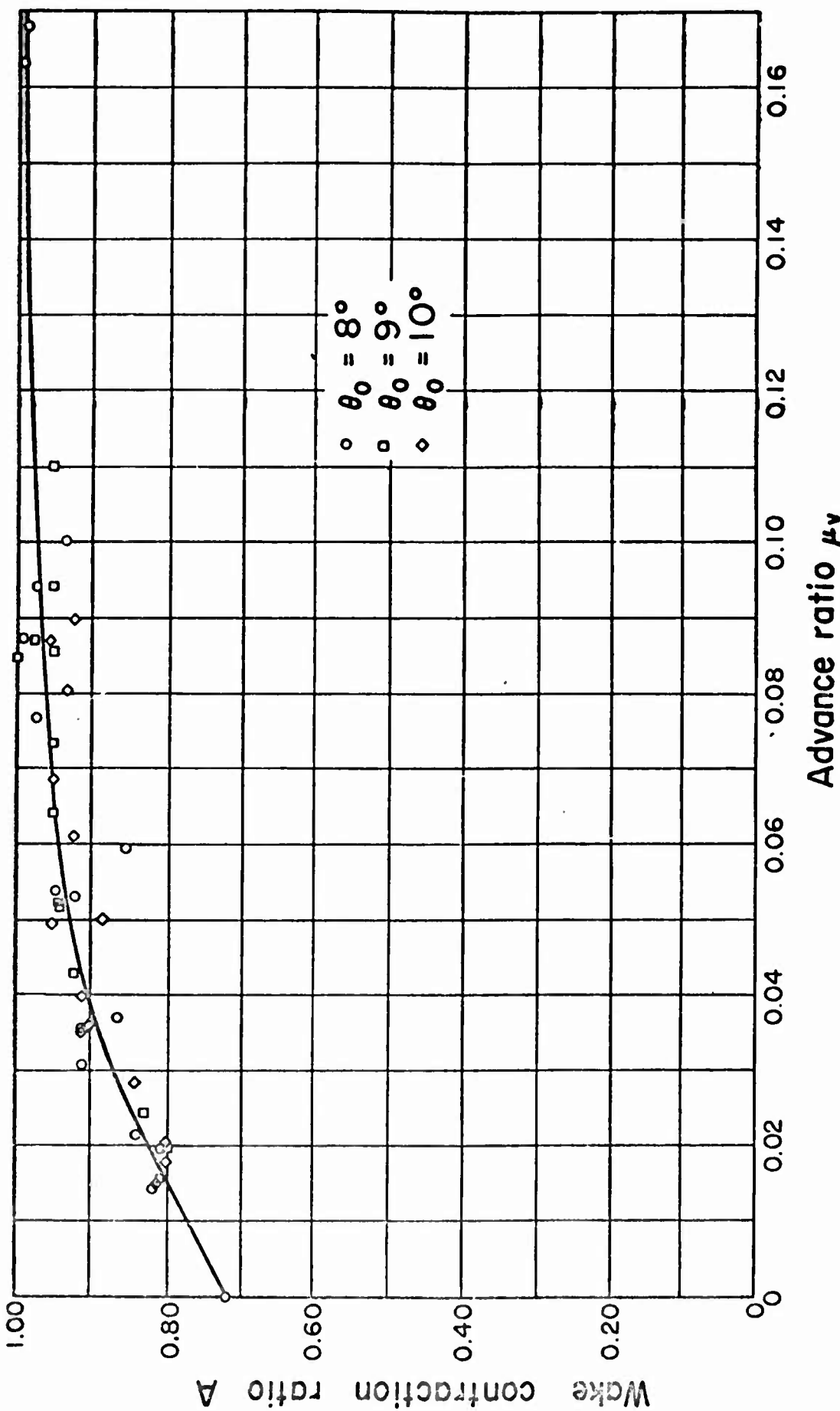


Figure 16. Experimentally determined wake contraction ratio of a single-bladed model rotor in low speed forward flight.

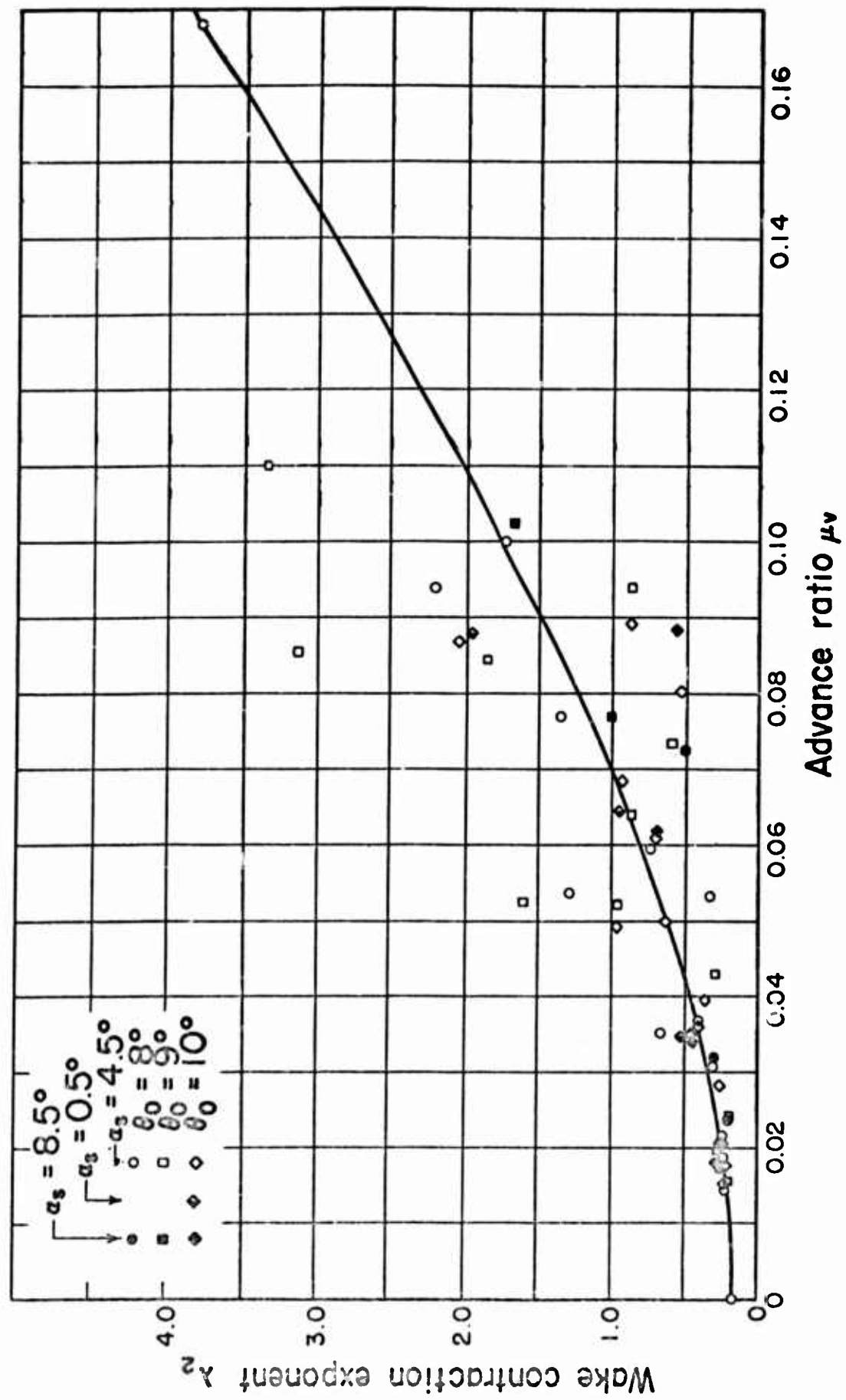


Figure 16. Experimentally determined wake contraction exponent of a single-bladed model rotor in low speed forward flight.

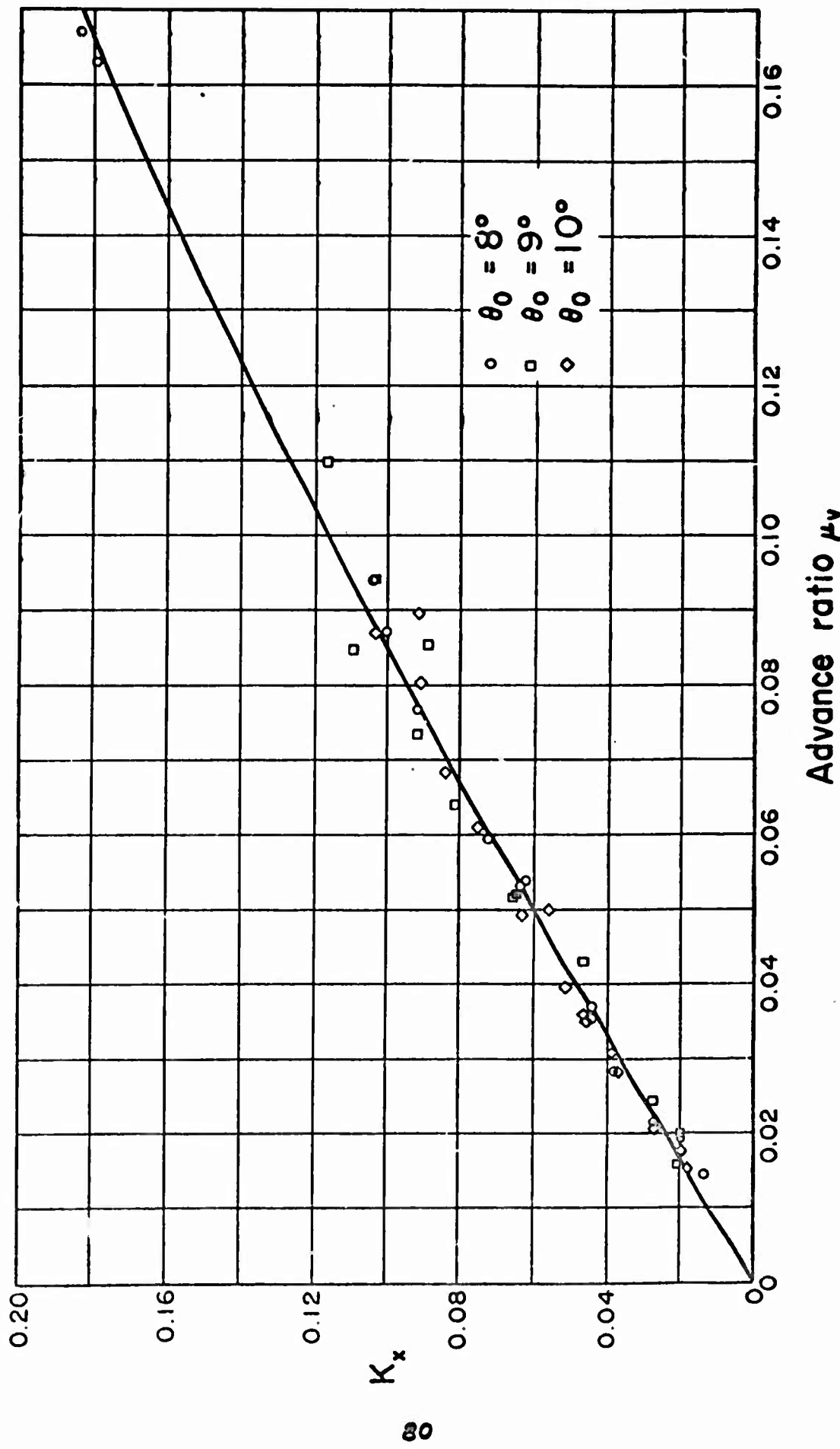


Figure 17. Variation of the parameter describing the longitudinal movement of the centers of the circular cross-sections of the wake with advance ratio for a single-bladed model rotor in low speed forward flight.

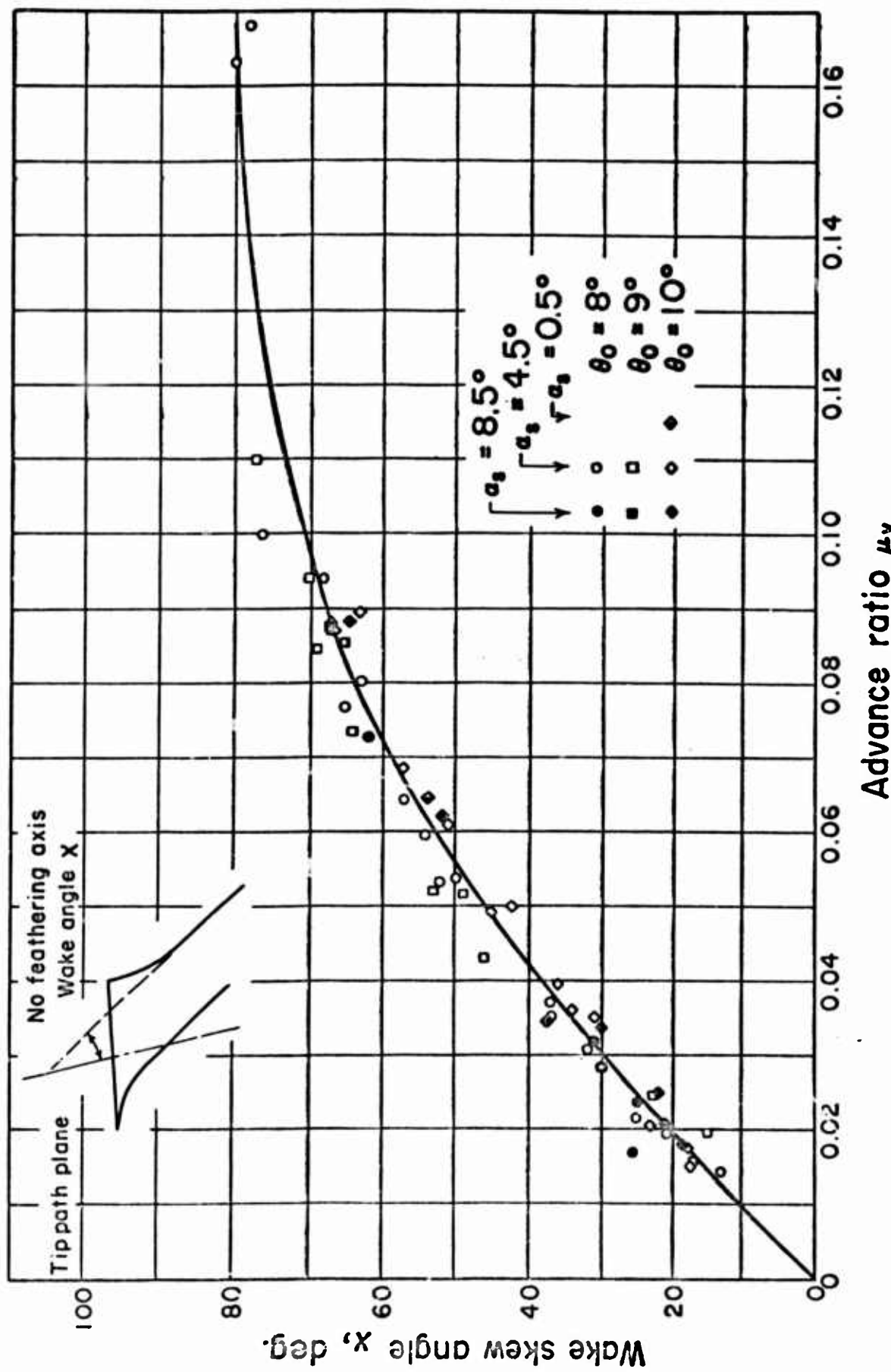


Figure 18. Experimental variation of the wake skew angle with advance ratio for a single-bladed model rotor in low speed forward flight.

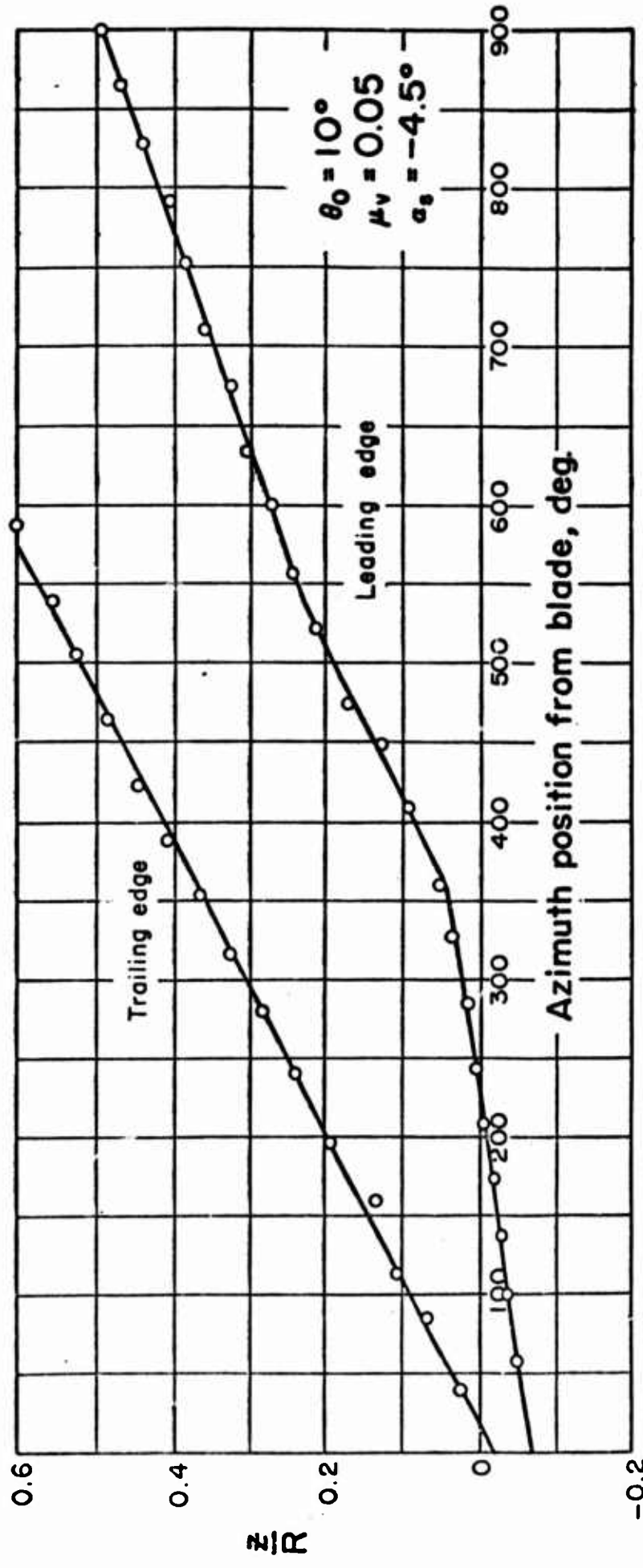


Figure 19. Plot of non-dimensional vertical displacement of the tip vortex in the longitudinal plane versus azimuth position from the blade feathering axis for a single-bladed model rotor in low speed forward flight.

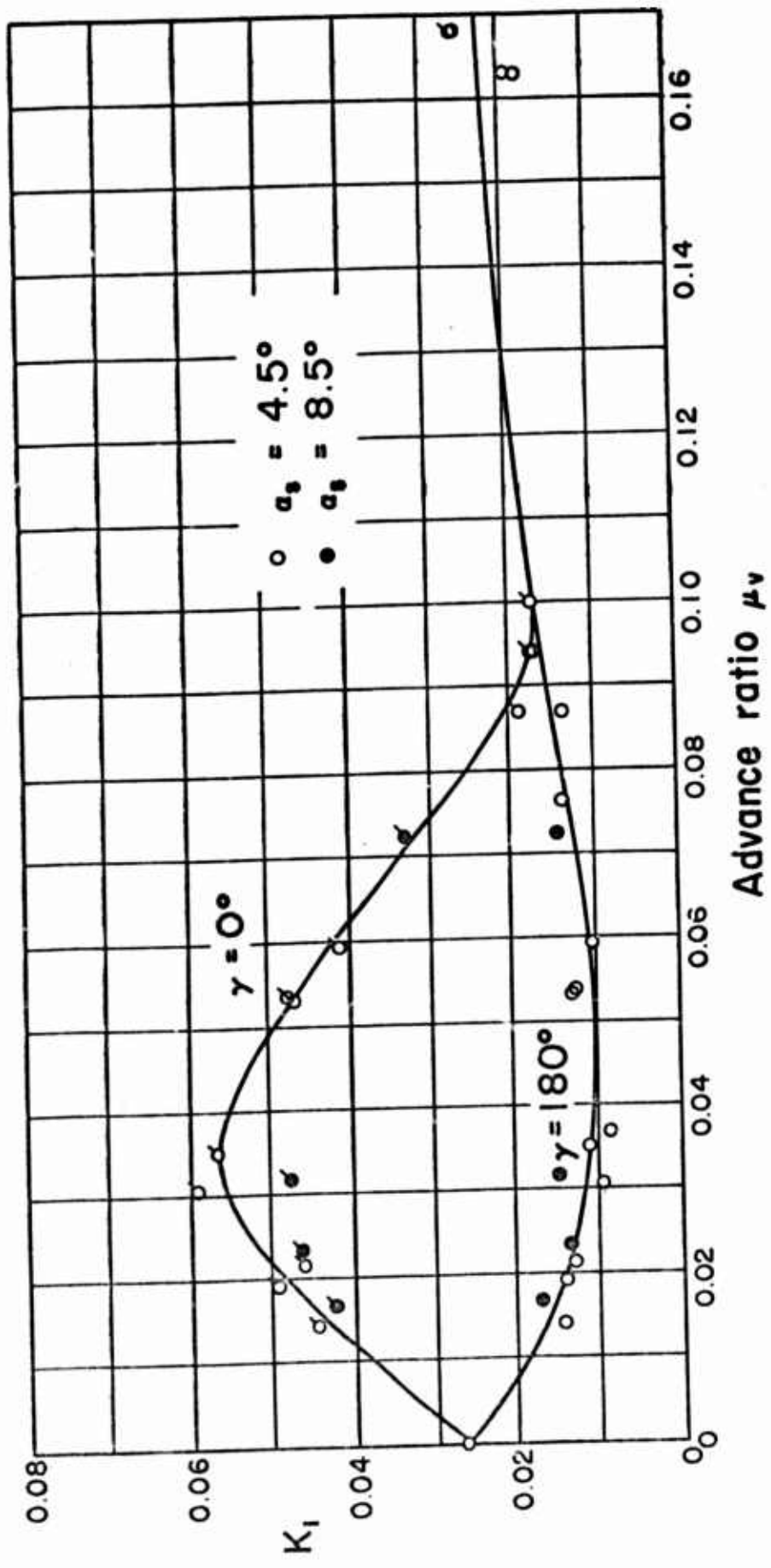


Figure 20a. Variation of the vertical motion parameter in the longitudinal plane with advance ratio for a single-bladed model rotor in low speed forward flight. $\theta_0 = 8.0^\circ$, $\gamma = 0^\circ$ and 180° .

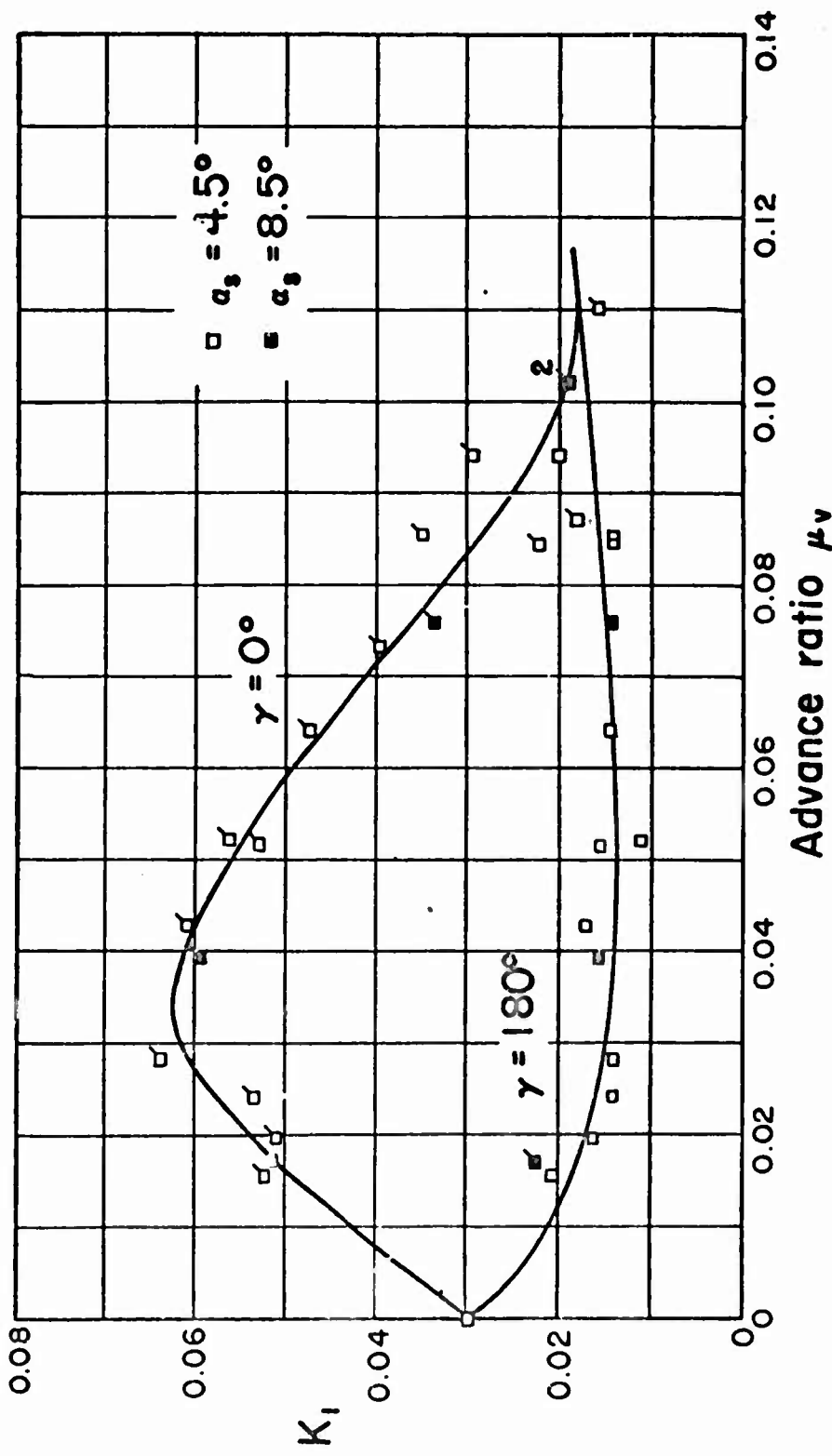


Figure 20b. Variation of the vertical motion parameter in the longitudinal plane with advance ratio for a single-bladed model rotor in low speed forward flight. $\theta_0 = 9.0^\circ$, $\gamma = 0^\circ$ and 180° .

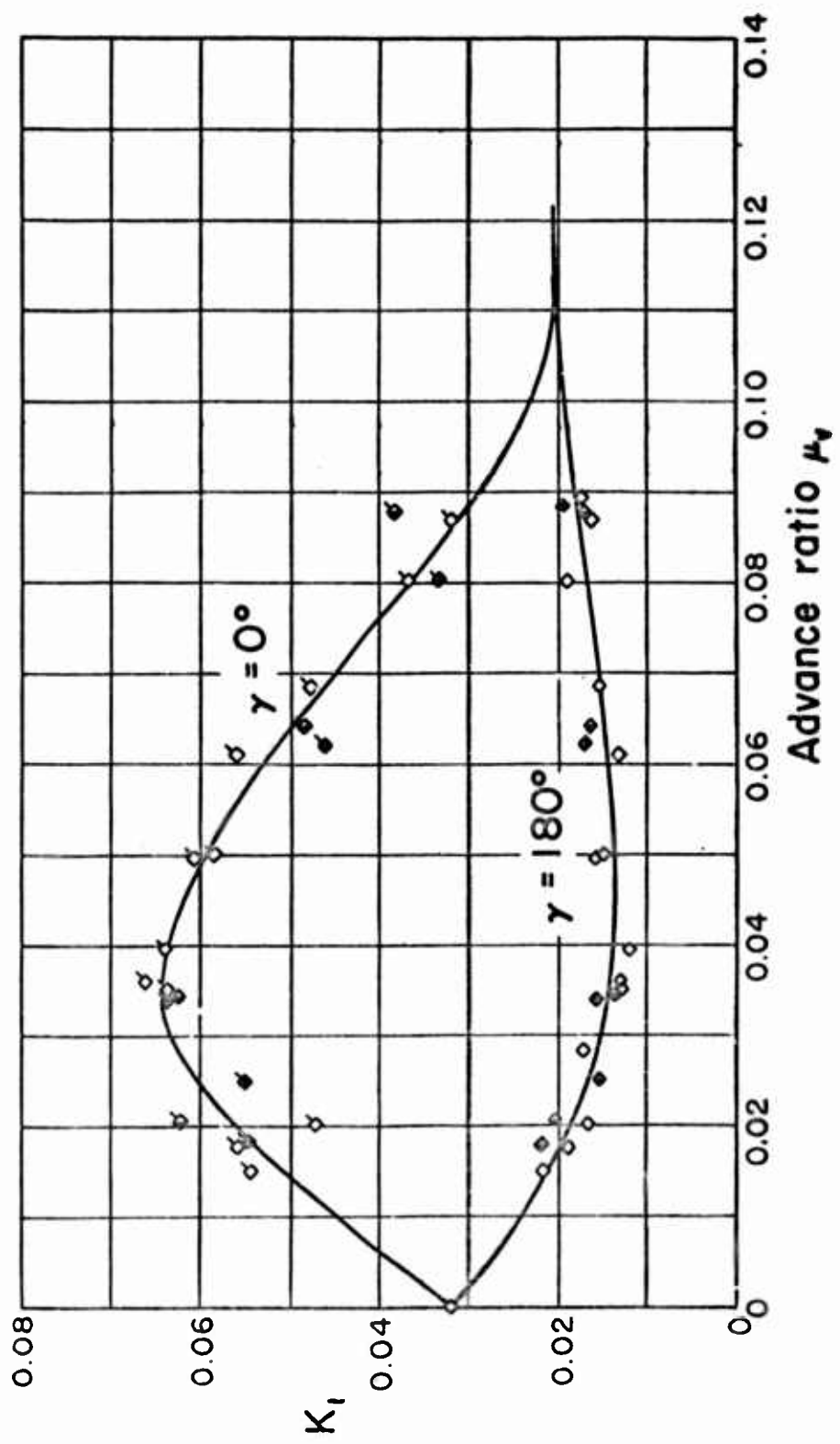


Figure 20c. Variation of the vertical motion parameter in the longitudinal plane with advance ratio for a single-bladed model rotor in low speed forward flight. $\theta_0 = 10.0^\circ$, $\gamma = 0^\circ$ and 180° .

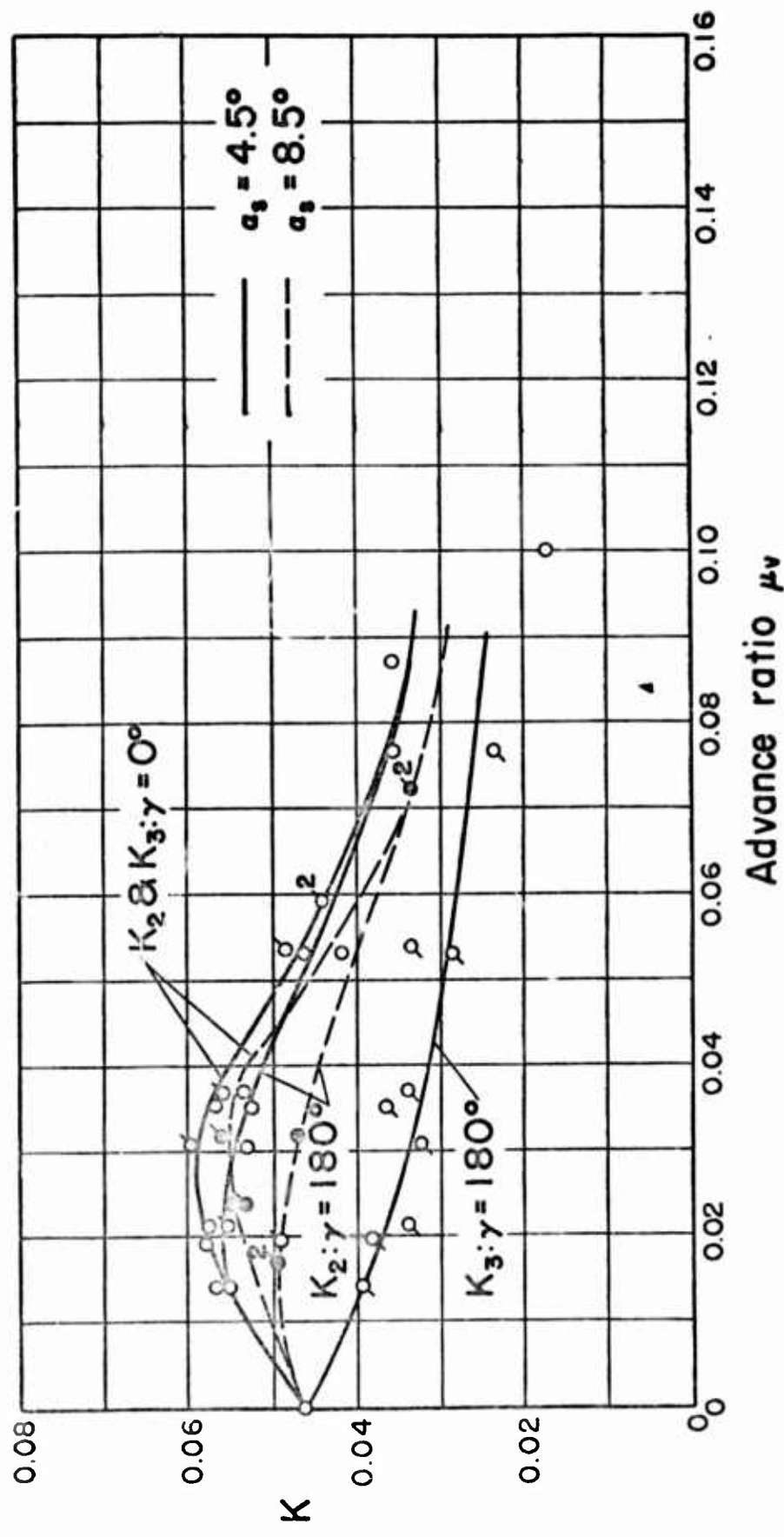


Figure 21a. Variation of the vertical motion parameters in the longitudinal plane with advance ratio for a single-bladed model rotor in low speed forward flight. $\theta_0 = 8.0^\circ$, $\gamma = 0^\circ$ and 180° .

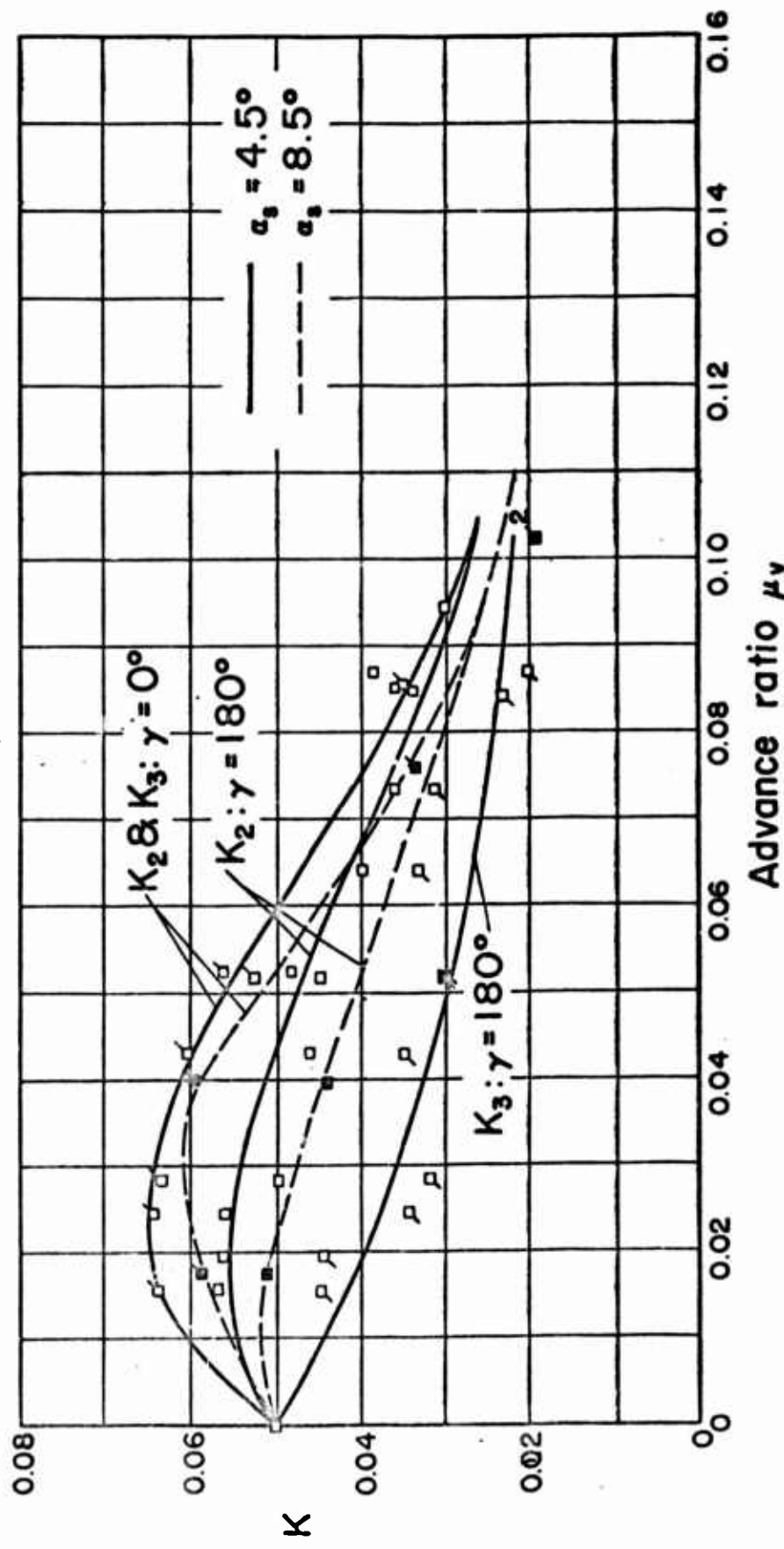


Figure 21b. Variation of the vertical motion parameters in the longitudinal plane with advance ratio for a single-bladed model rotor in low speed forward flight. $\theta_0 = 9.0^\circ$, $\gamma = 0^\circ$ and 180° .

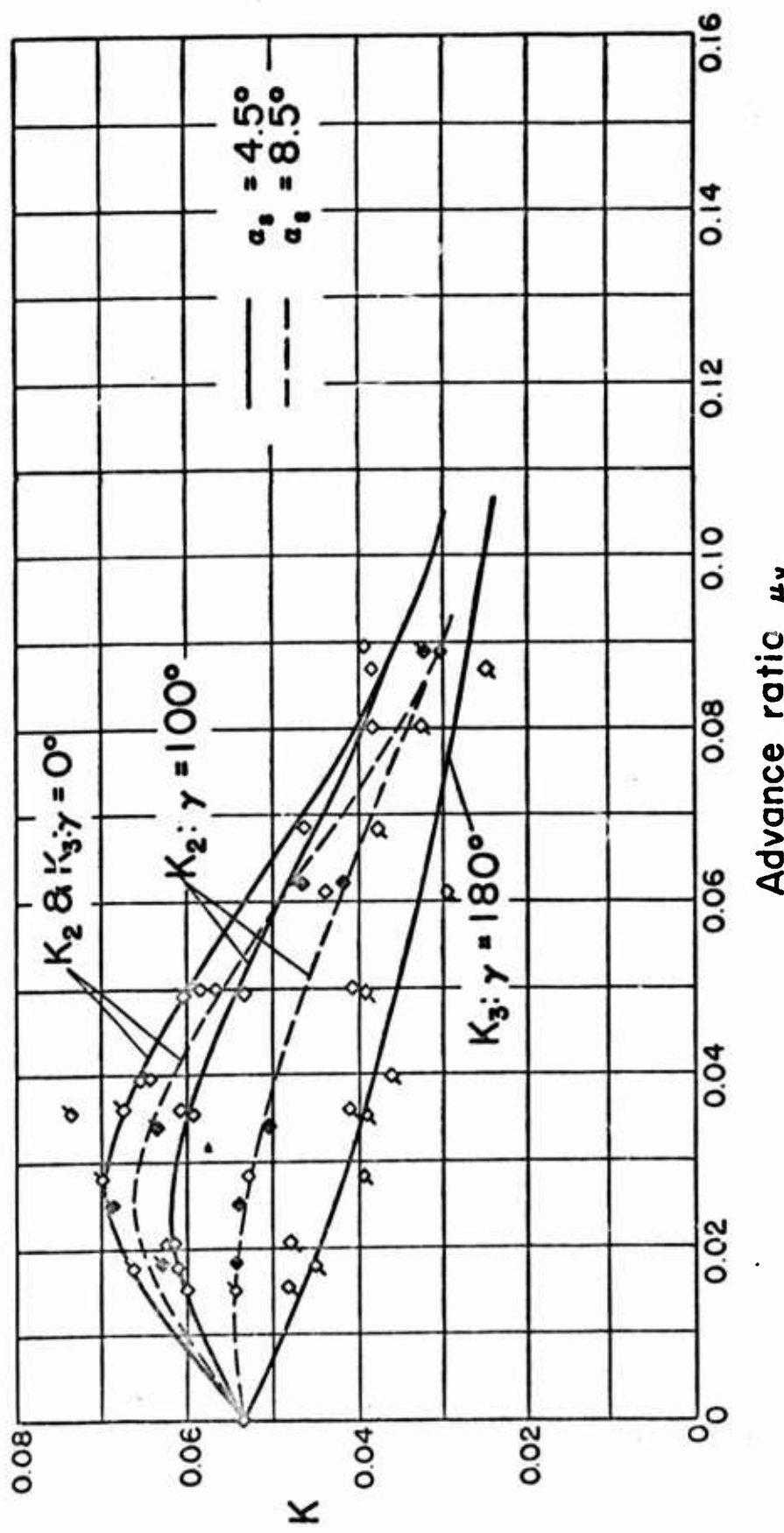


Figure 21c. Variation of the vertical motion parameters in the longitudinal plane with advance ratio for a single-bladed model rotor in low speed forward flight. $\theta_0 = 10.0^\circ$, $\gamma = 0^\circ$ and 180° .

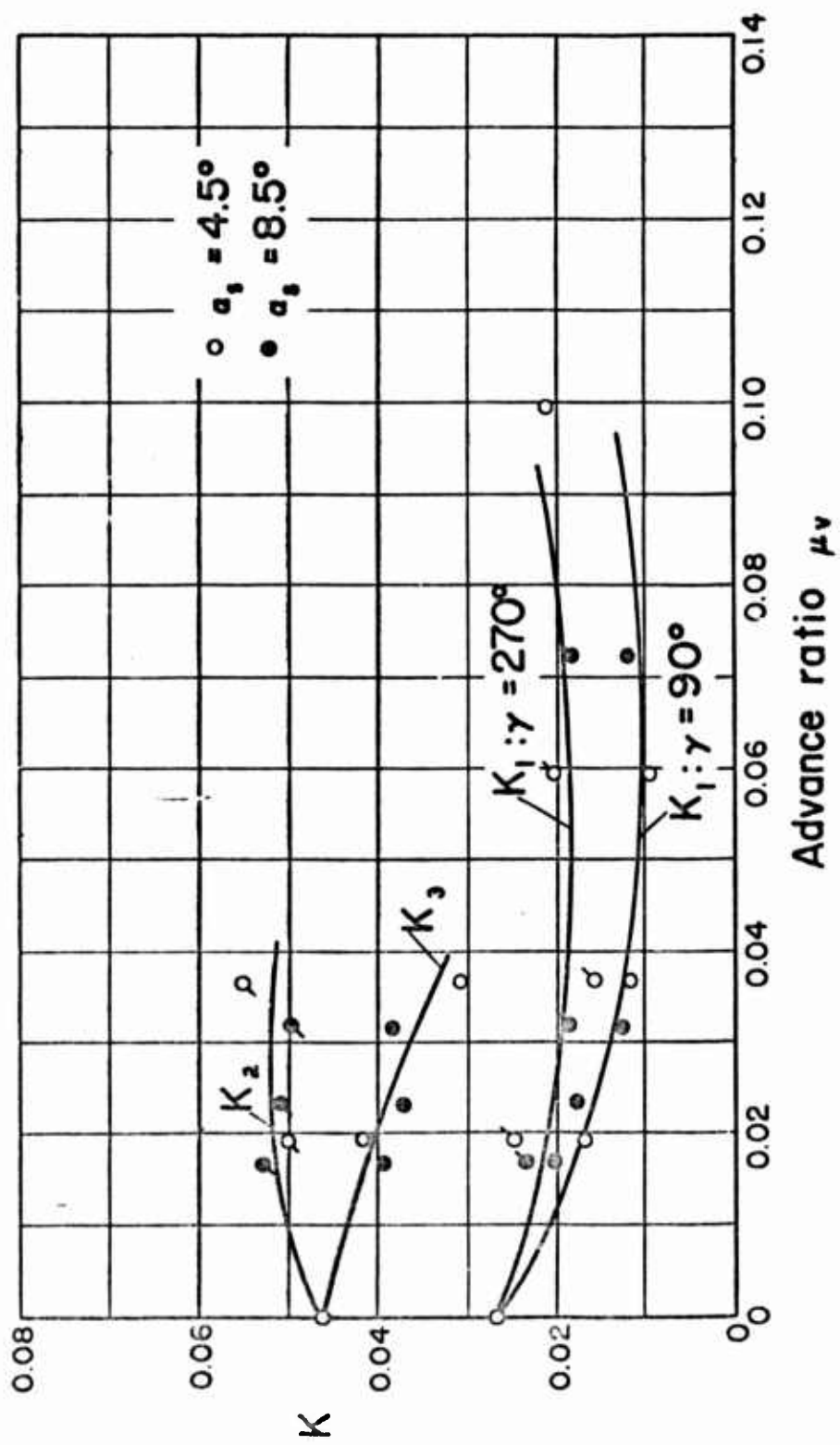


Figure 22a. Variation of the vertical motion parameters in the lateral plane with advance ratio for a single-bladed model rotor in low speed forward flight. $\theta_0 = 8.0^\circ$, $\beta = 90^\circ$ and 270° .

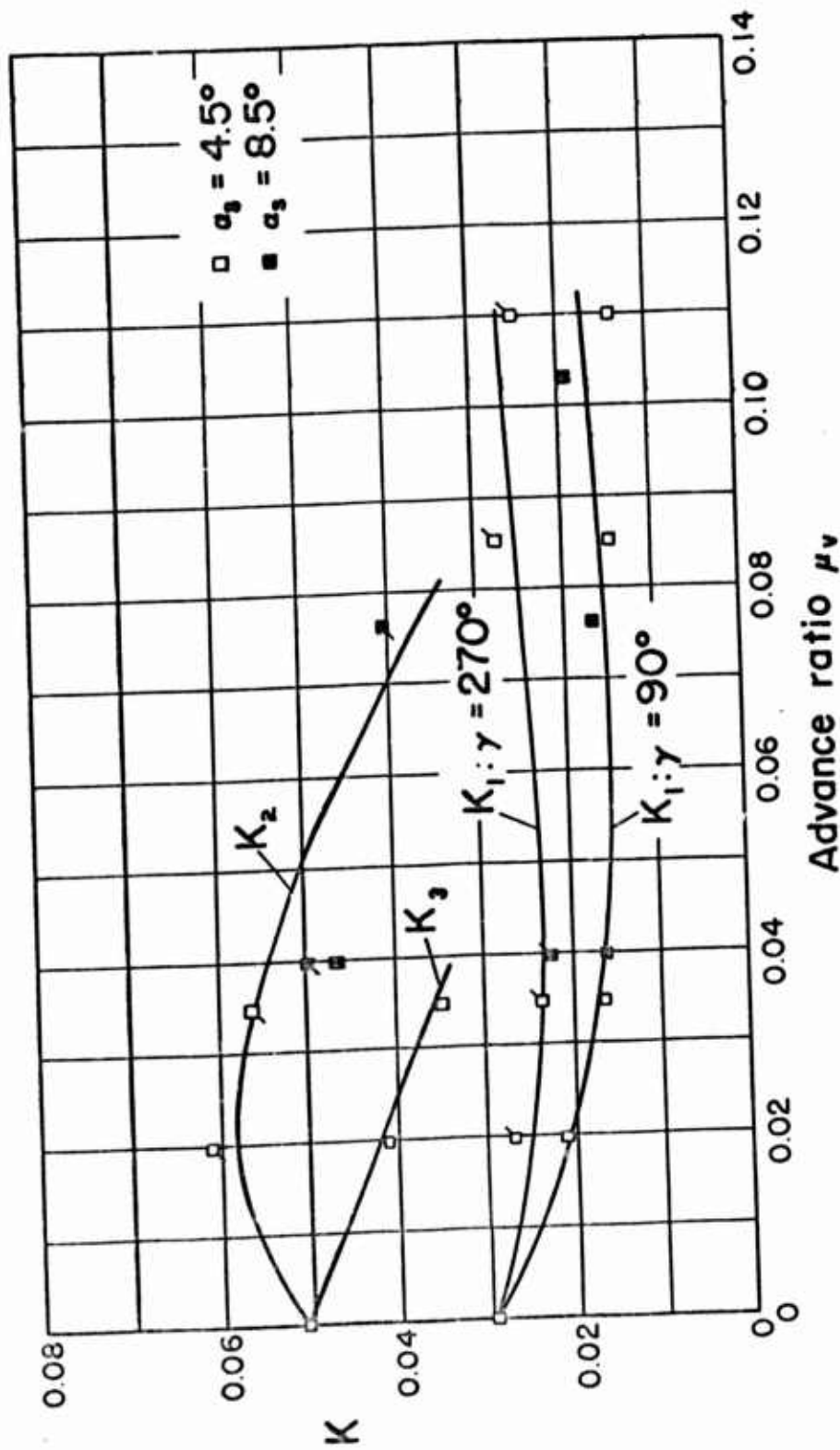


Figure 22b. Variation of the vertical motion parameters in the lateral plane with advance ratio for a single-bladed model rotor in low speed forward flight. $\theta_0 = 9.0^\circ$, $\gamma = 90^\circ$ and 270° .

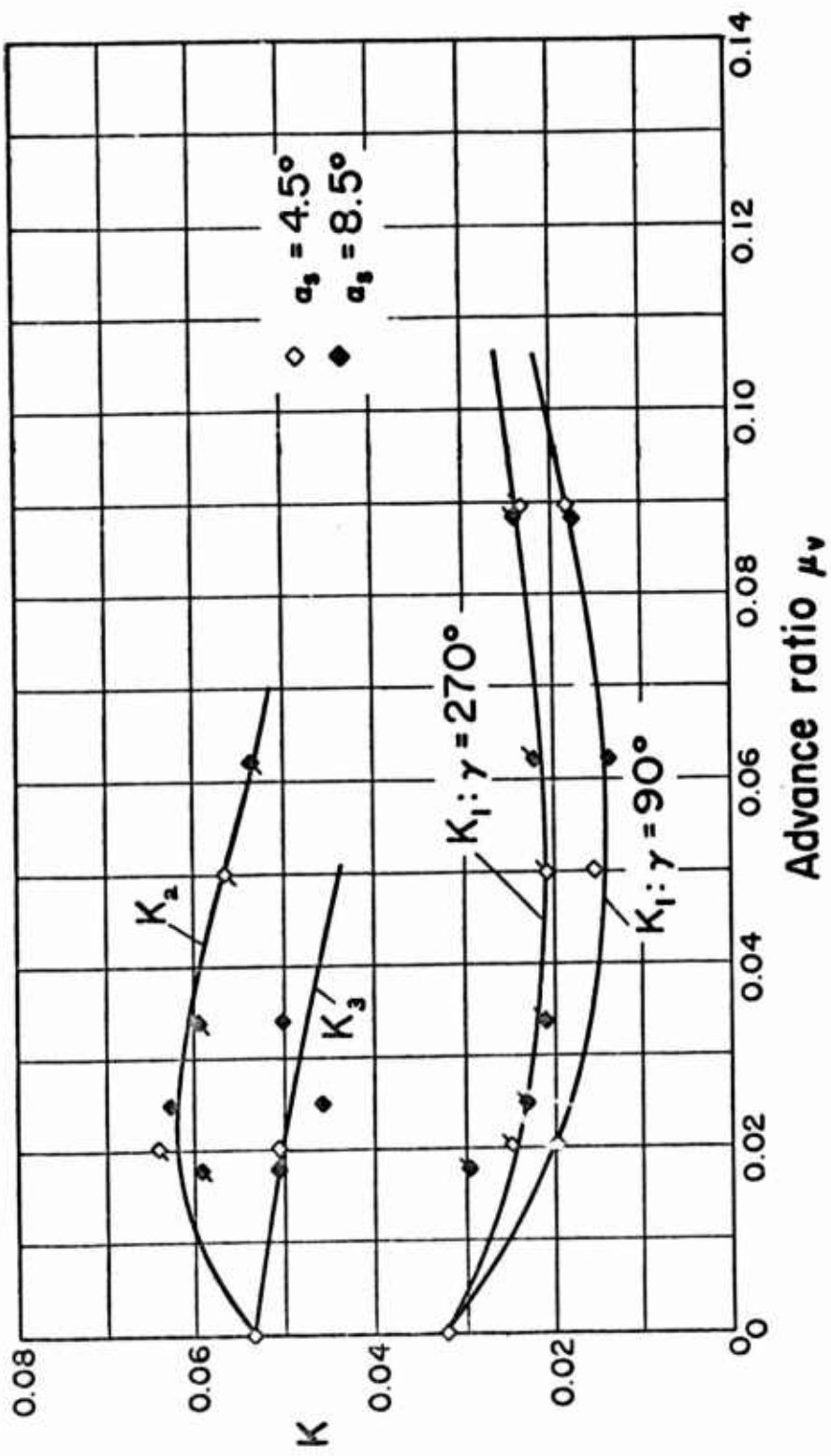


Figure 22c. Variation of the vertical motion parameters in the lateral plane with advance ratio for a single-bladed model rotor in low speed forward flight. $\theta_o = 10.0^\circ$, $\gamma = 90^\circ$ and 270° .

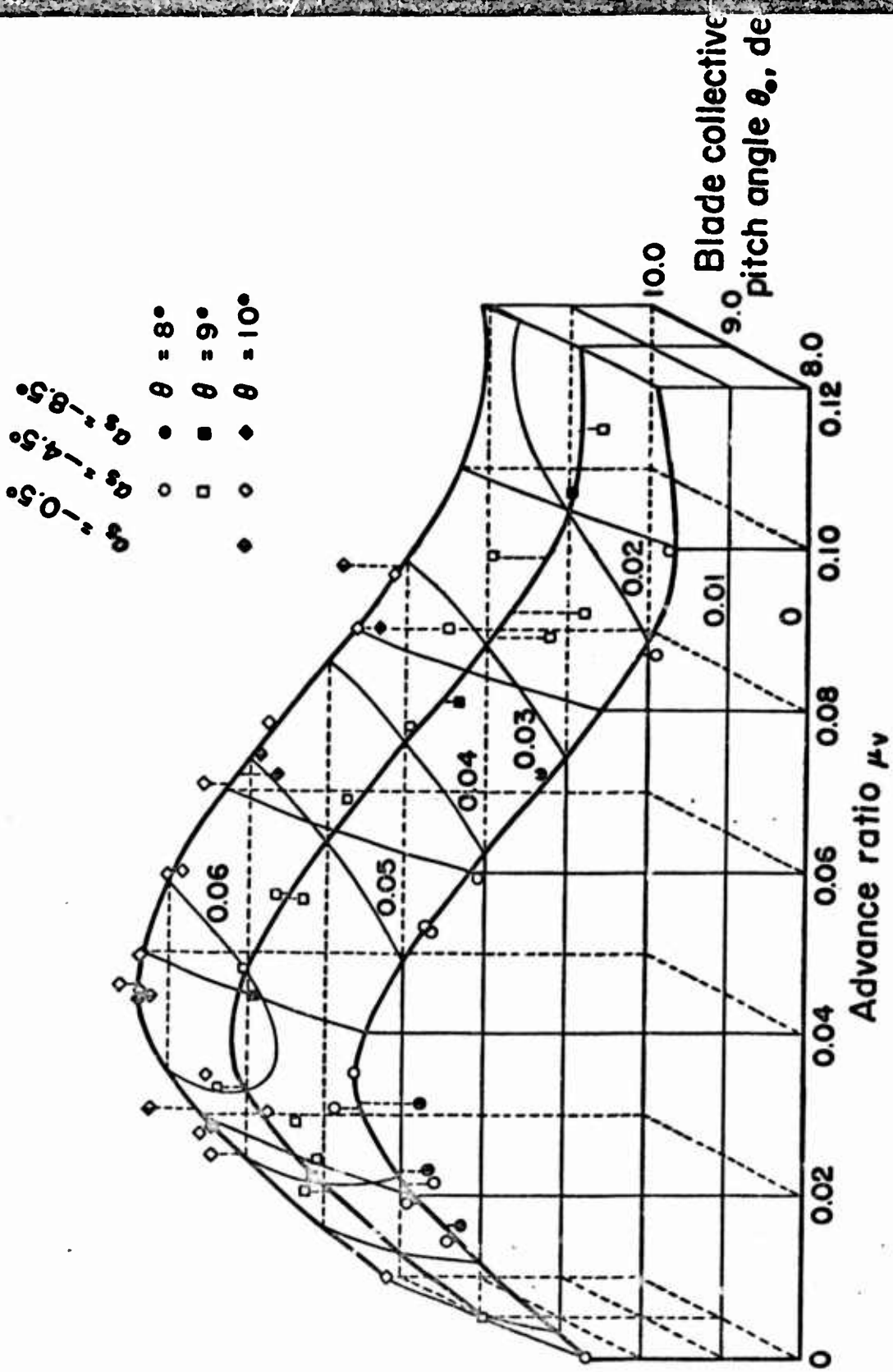


Figure 23. Experimental variation of K_{c0} with advance ratio, blade collective pitch angle, and shaft angle of attack for a single-bladed model rotor in low speed forward flight.

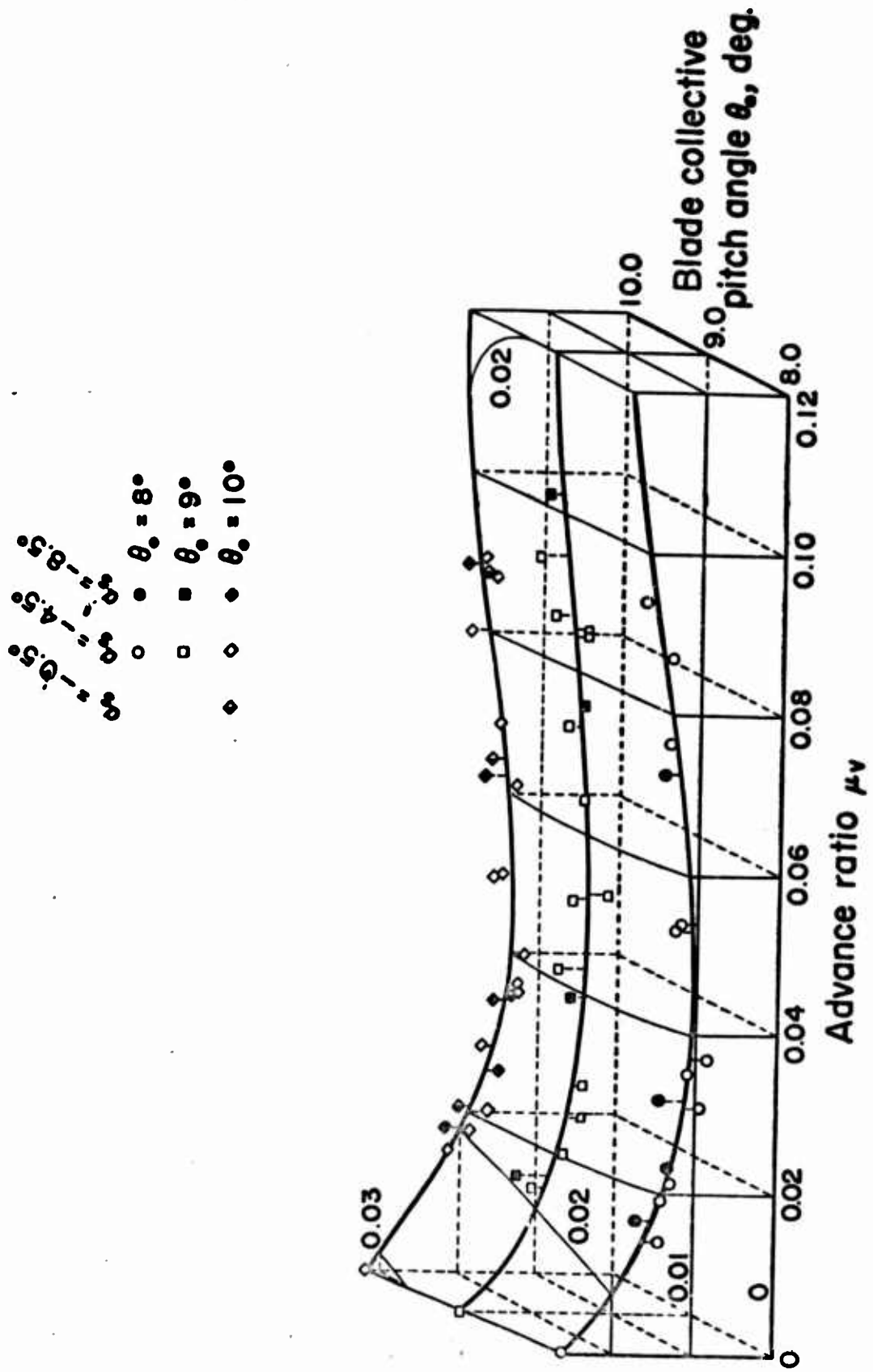


Figure 24. Experimental variation of $K_{1,go}$ with advance ratio, blade collective pitch angle, and shaft angle of attack for a single-bladed rotor in low speed forward flight.

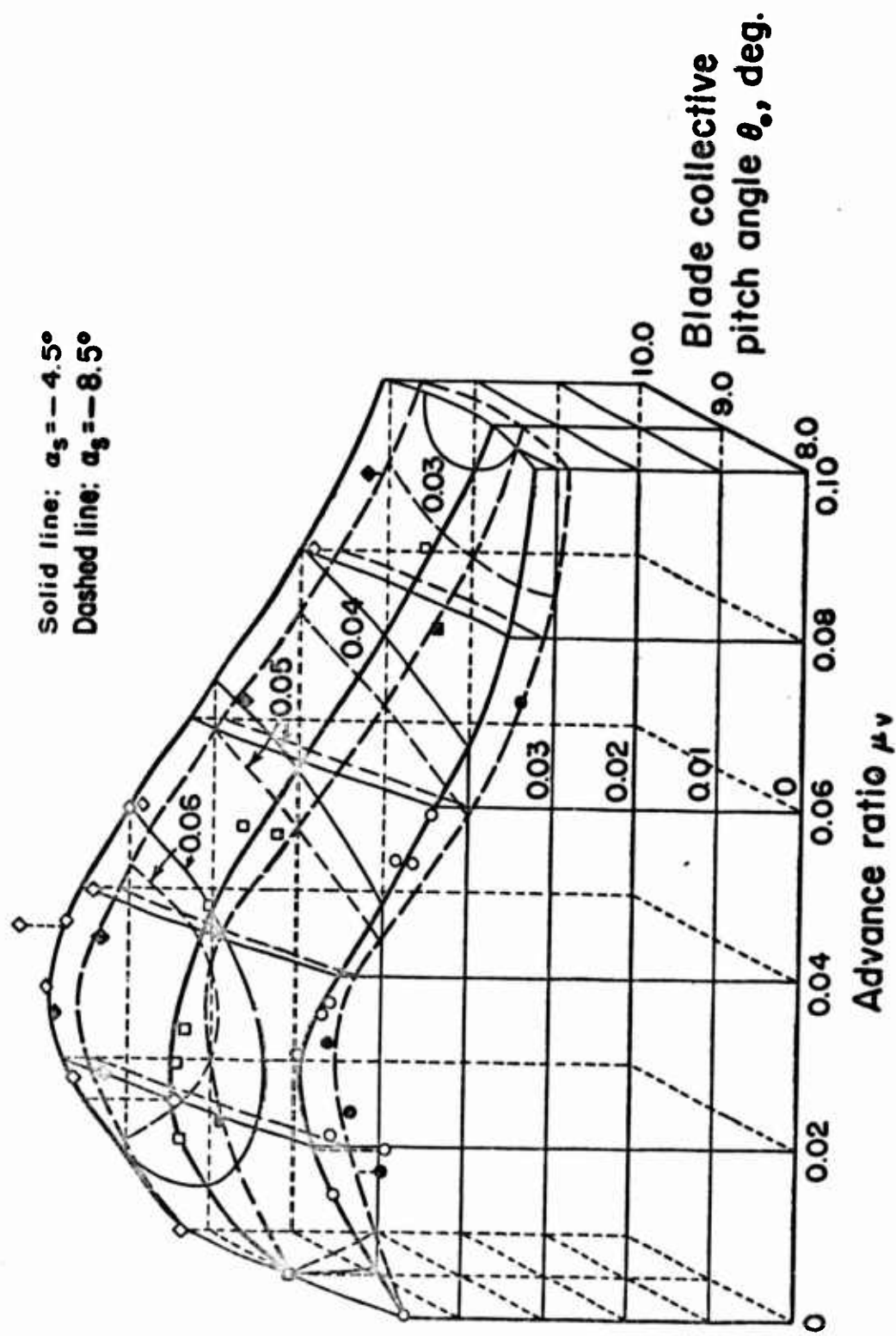


Figure 25. Experimental variation of K_{30} and K_{300} with advance ratio, blade collective pitch angle, and shaft angle of attack for a single-bladed rotor in low speed forward flight.

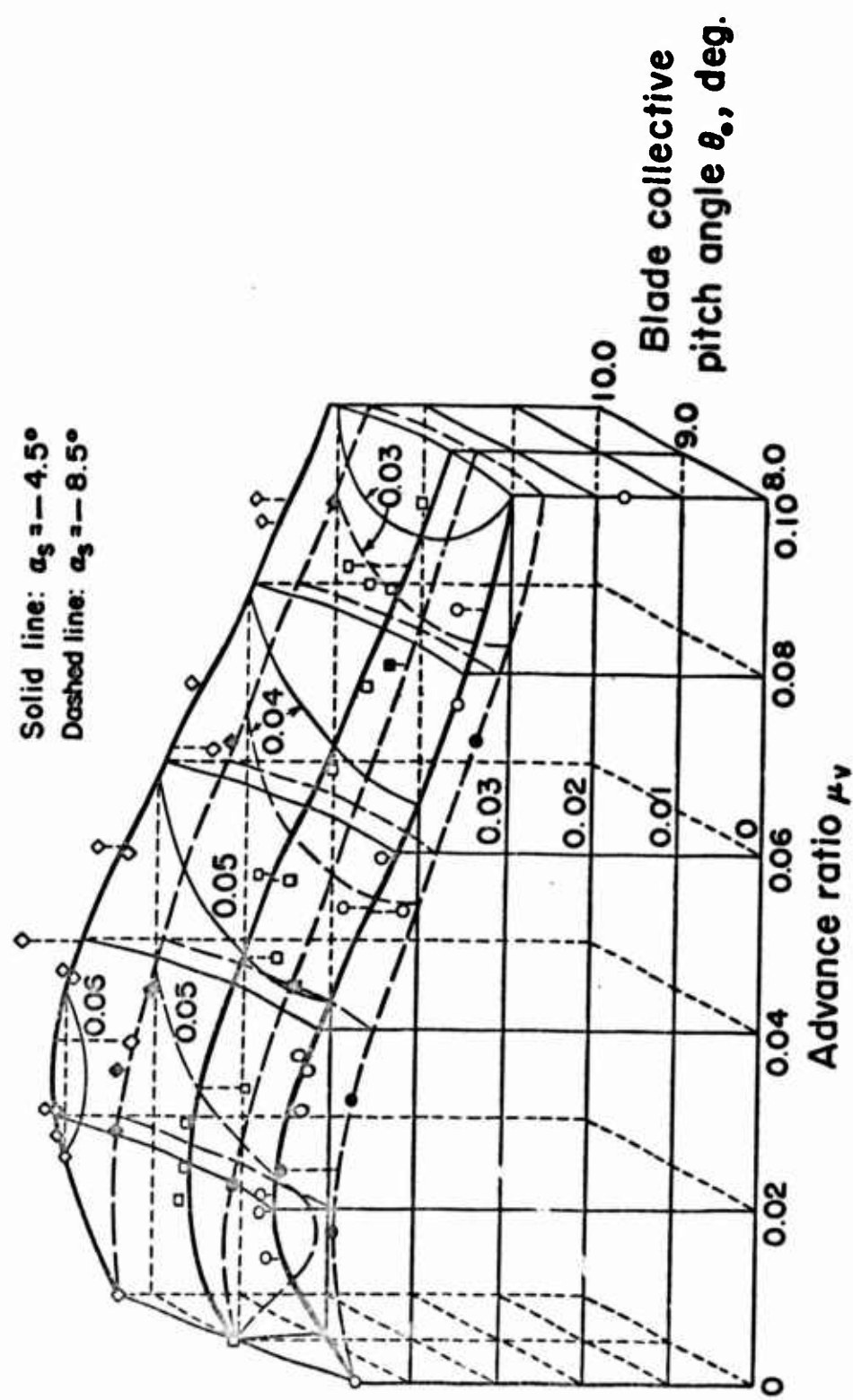


Figure 26. Experimental variation of $K_{2,100}$ with advance ratio, blade collective pitch angle, and shaft angle of attack for a single-bladed model rotor in low speed forward flight.

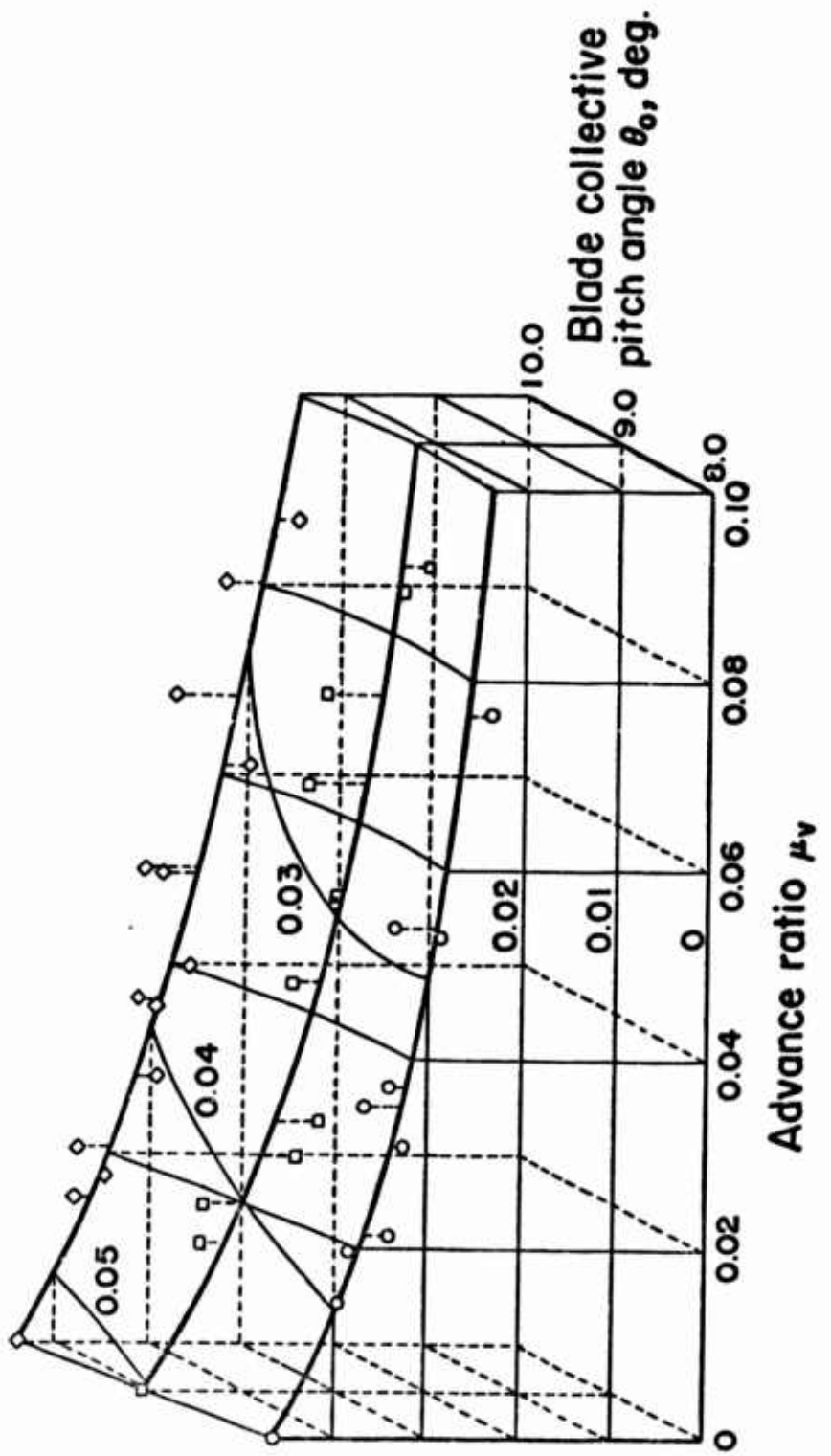


Figure 27. Experimental variation of $K_{3,00}^{\circ}$ with advance ratio, blade collective pitch angle, and shaft angle of attack for a single-bladed model rotor in low speed forward flight.

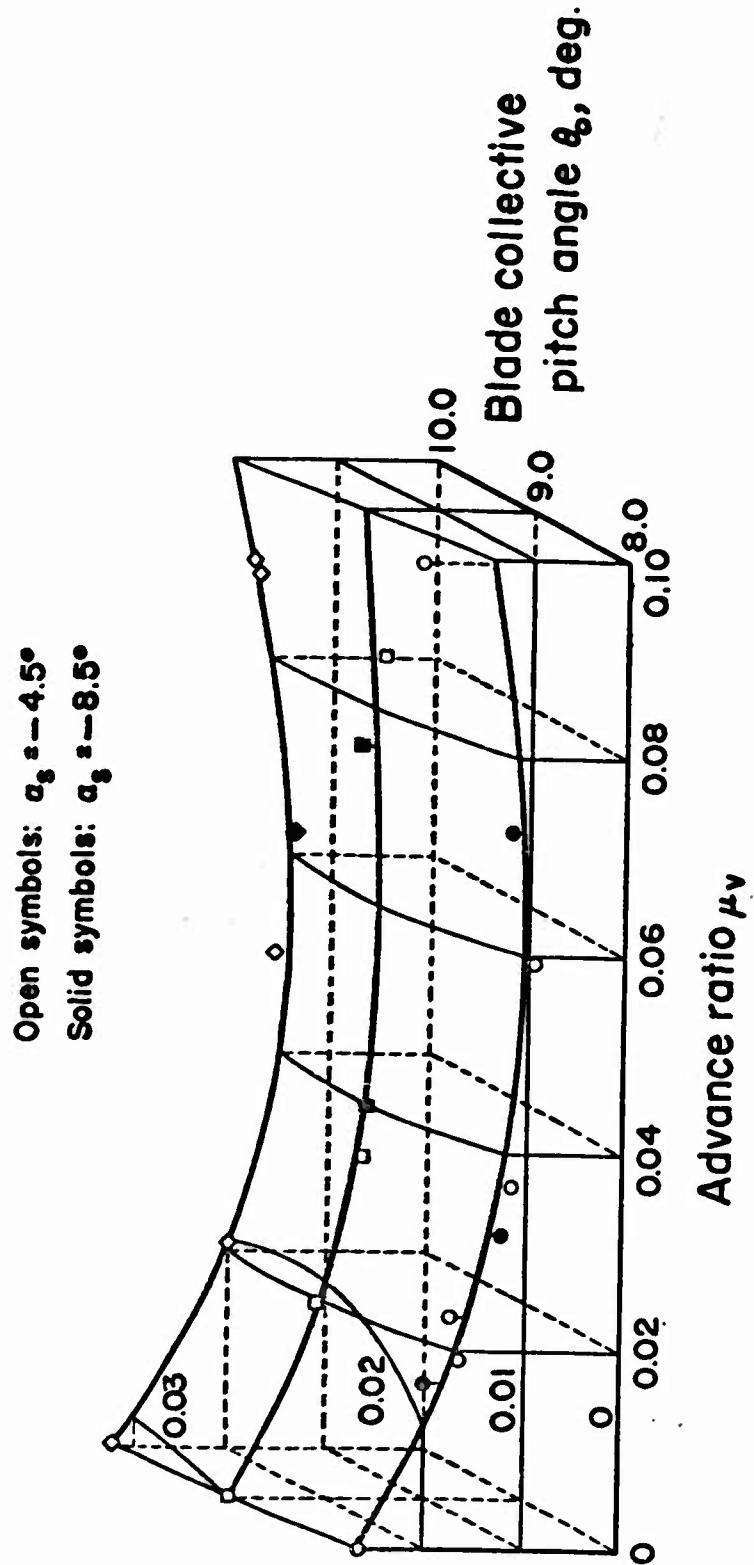


Figure 28. Experimental variation of K_{1q0} with advance ratio, blade collective pitch angle, and shaft angle of attack for a single-bladed model rotor in low speed forward flight.

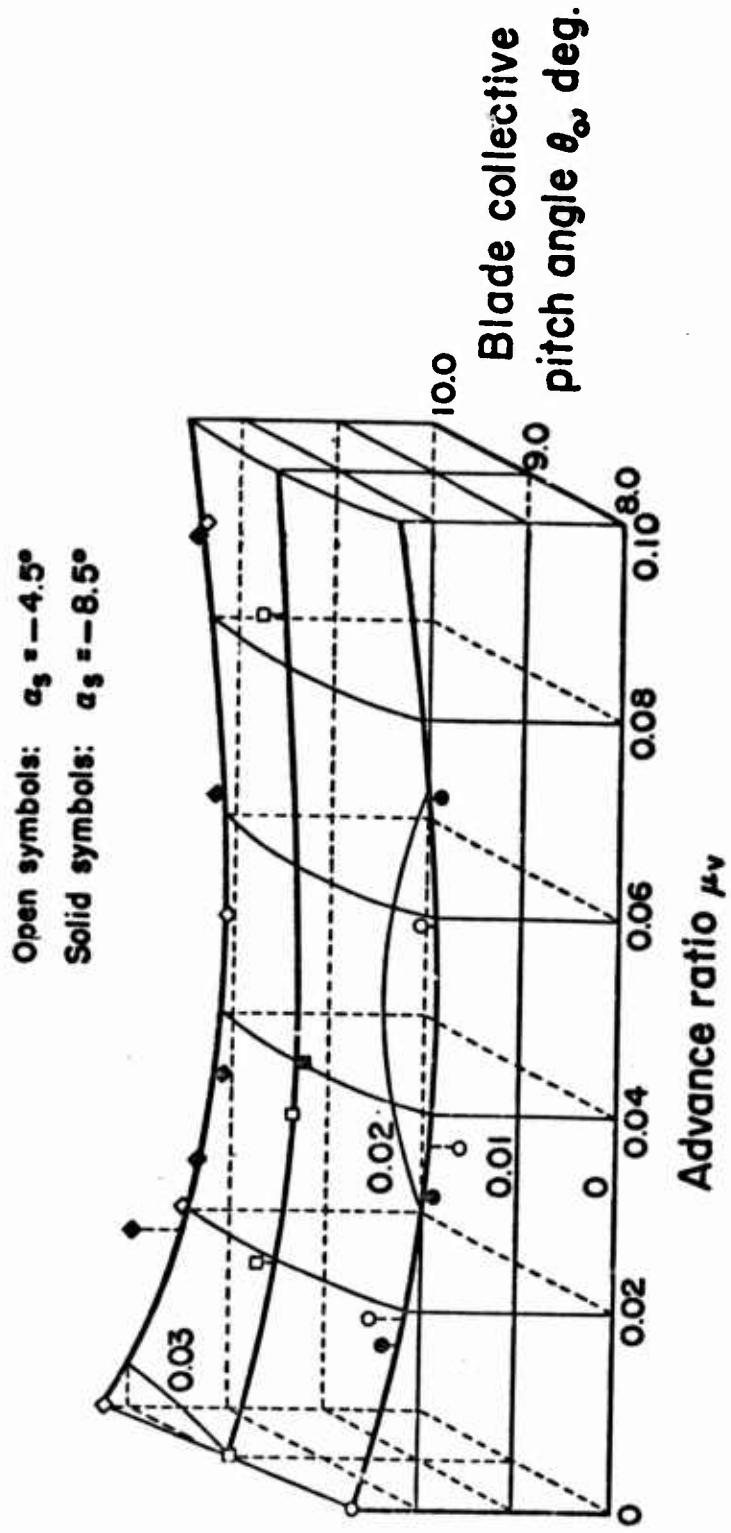
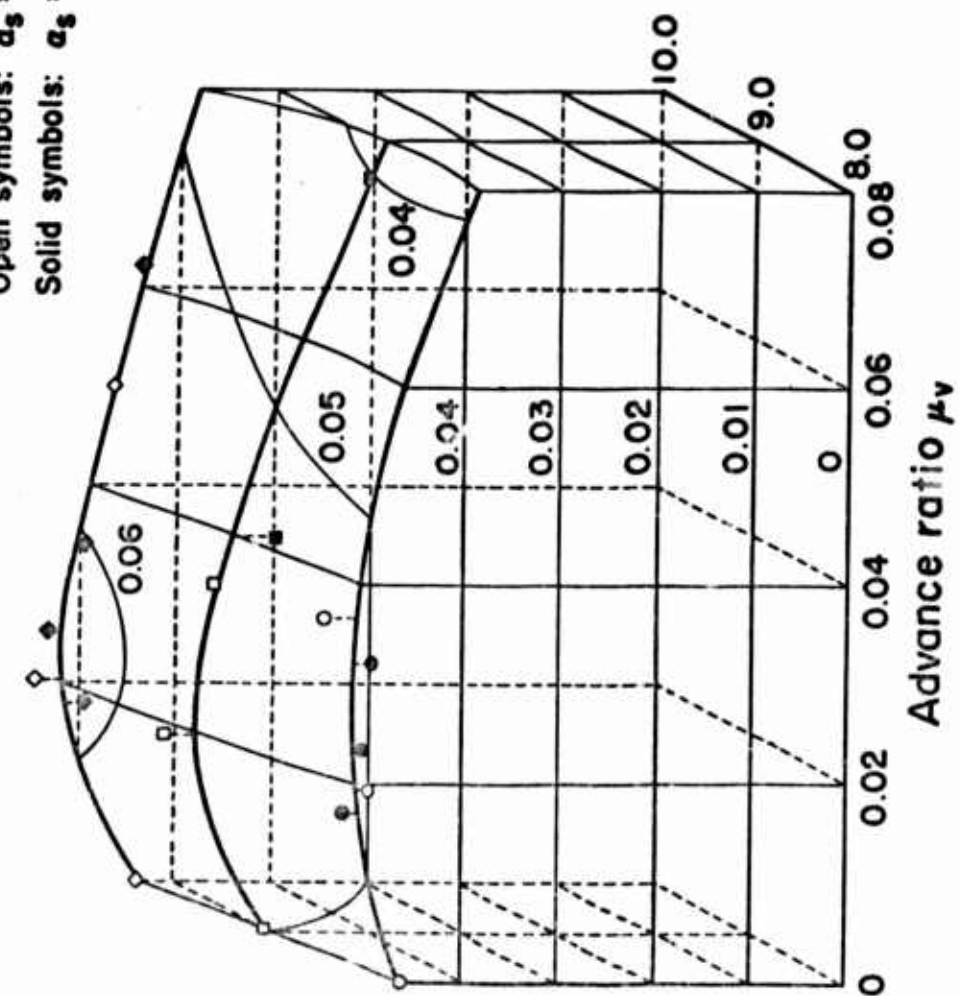


Figure 29. Experimental variation of K_{1270} with advance ratio, blade collective pitch angle, and shaft angle of attack for a single-bladed model rotor in low speed forward flight.

Open symbols: $\alpha_s = -4.5^\circ$
 Solid symbols: $\alpha_s = -8.5^\circ$



a) K_{290° and K_{2270°

b) K_{390° and K_{3270°

Figure 30. Experimental variation of K_{290° , K_{2270° , K_{390° , and K_{3270° with advance ratio, blade collective pitch angle, and shaft angle of attack for a single-bladed rotor in low speed forward flight.

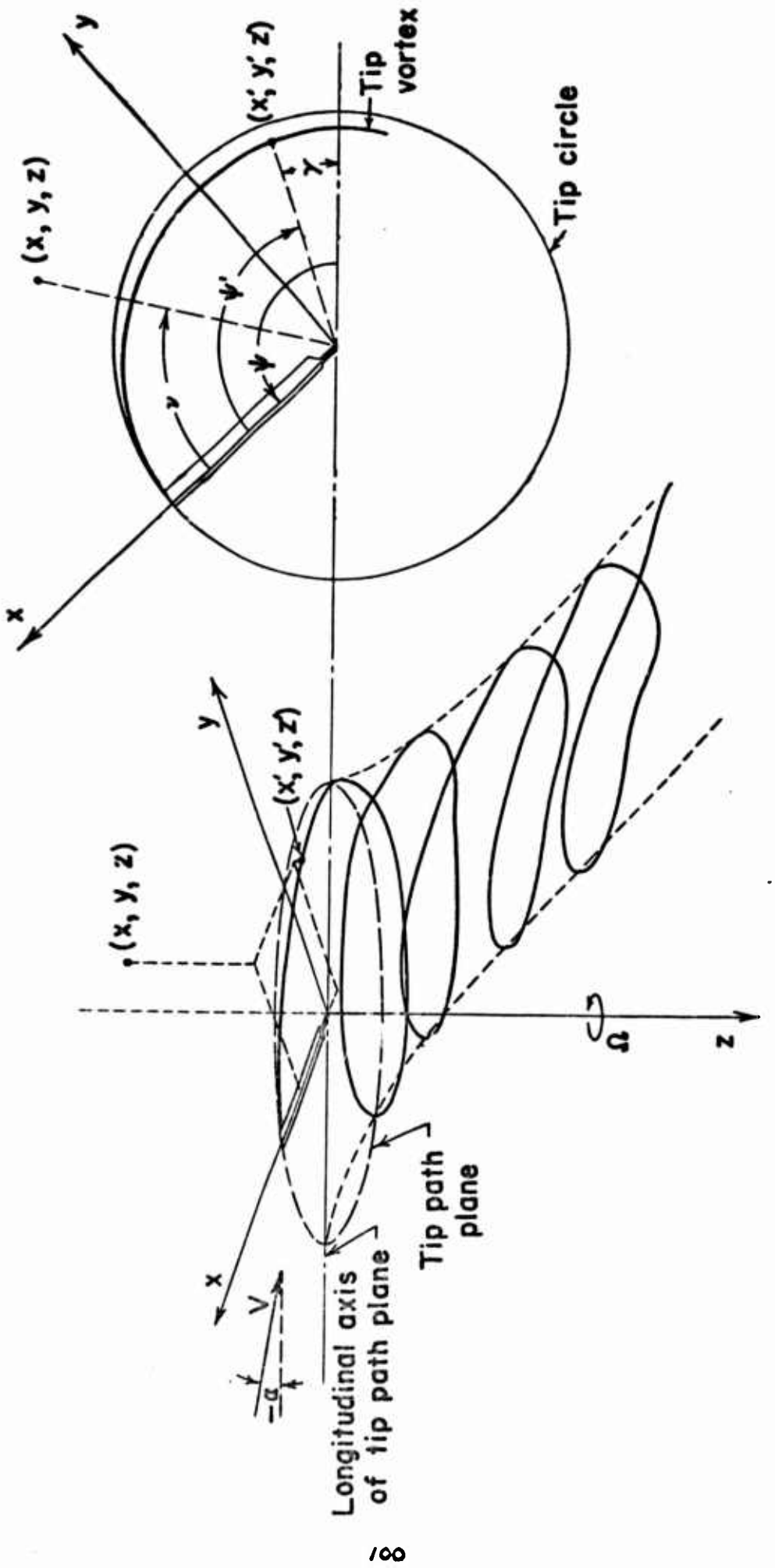


Figure 31. Coordinate system used in forward flight analysis.

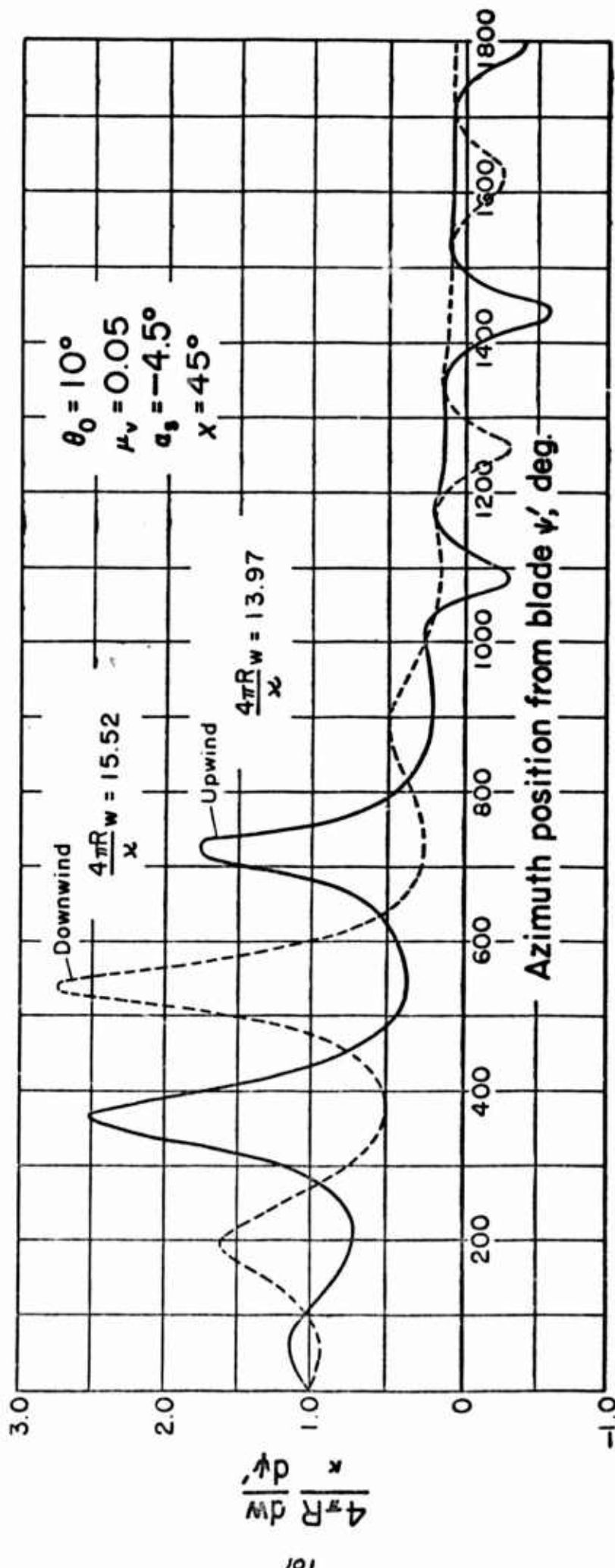


Figure 32. Evaluation of the integral for the non-dimensional normal component of induced velocity at the center of the tip path plane for the single blade in the upwind and downwind position. (Equation B-1C-c)

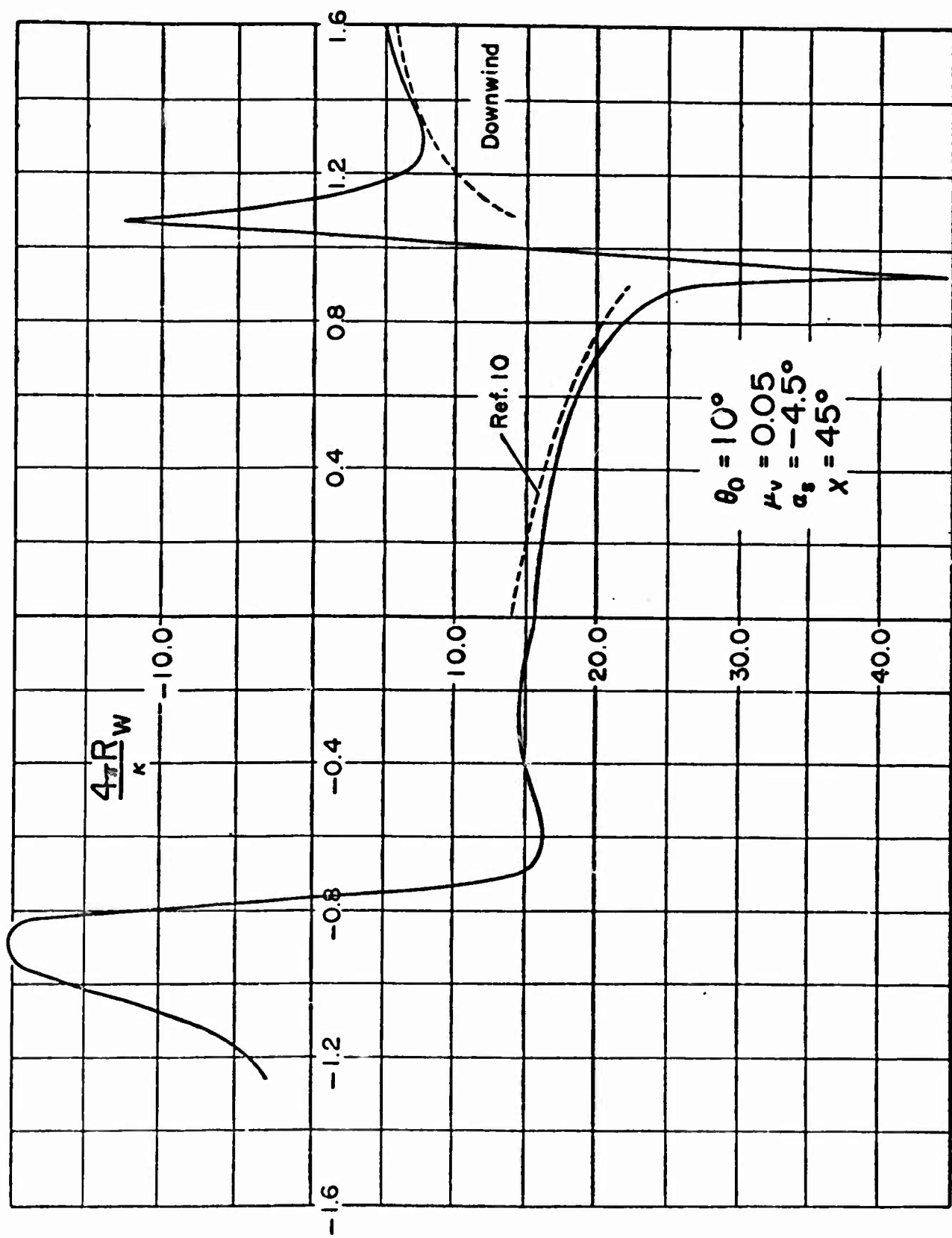


Figure 33. Calculated non-dimensional normal component of induced velocity across the longitudinal diameter of the tip path plane that is associated with the tip vortex when the single blade is in the downwind position.

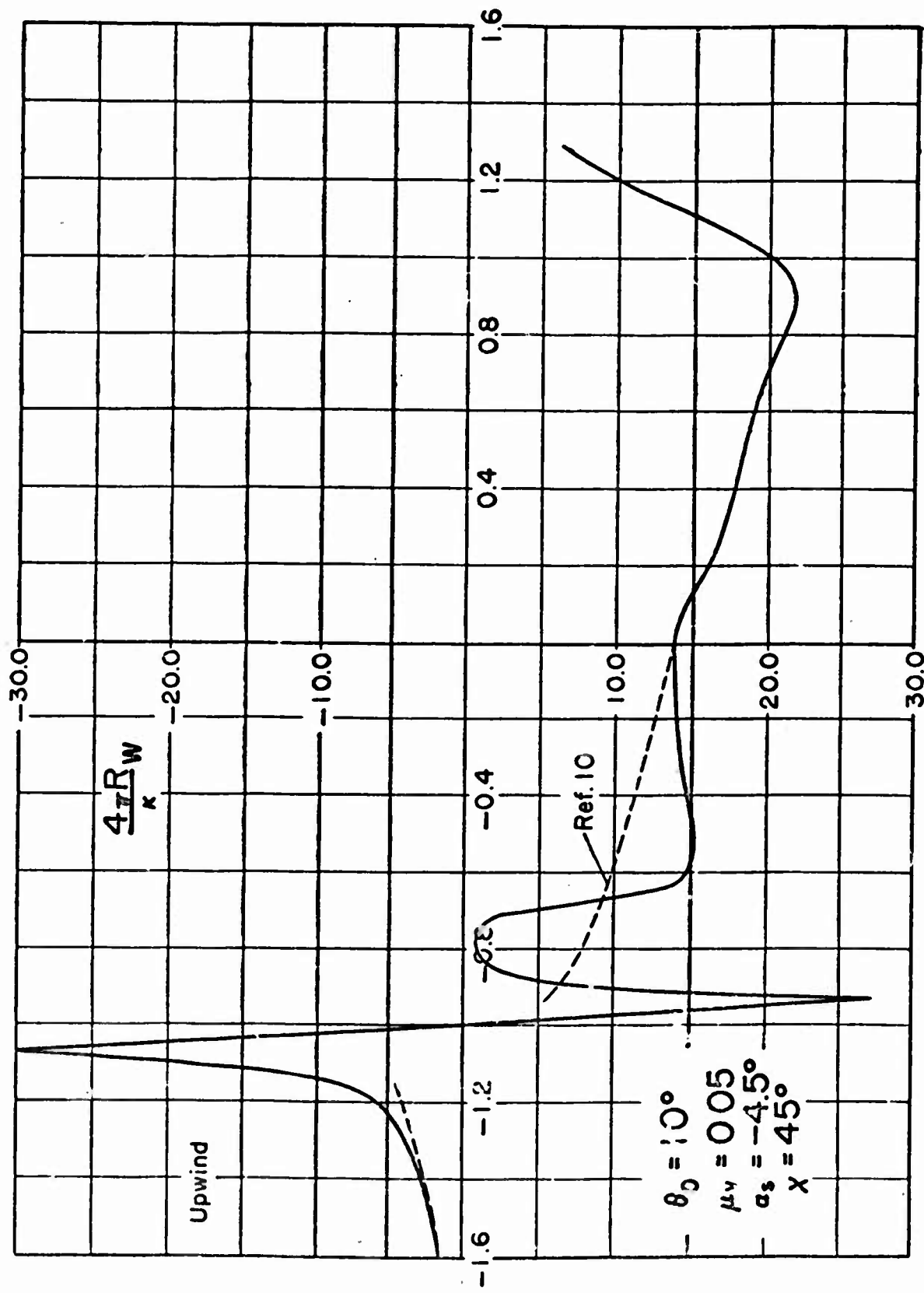


Figure 34. Calculated non-dimensional normal component of induced velocity across the longitudinal diameter of the tip path plane that is associated with the tip vortex when the single blade is in the upwind position.

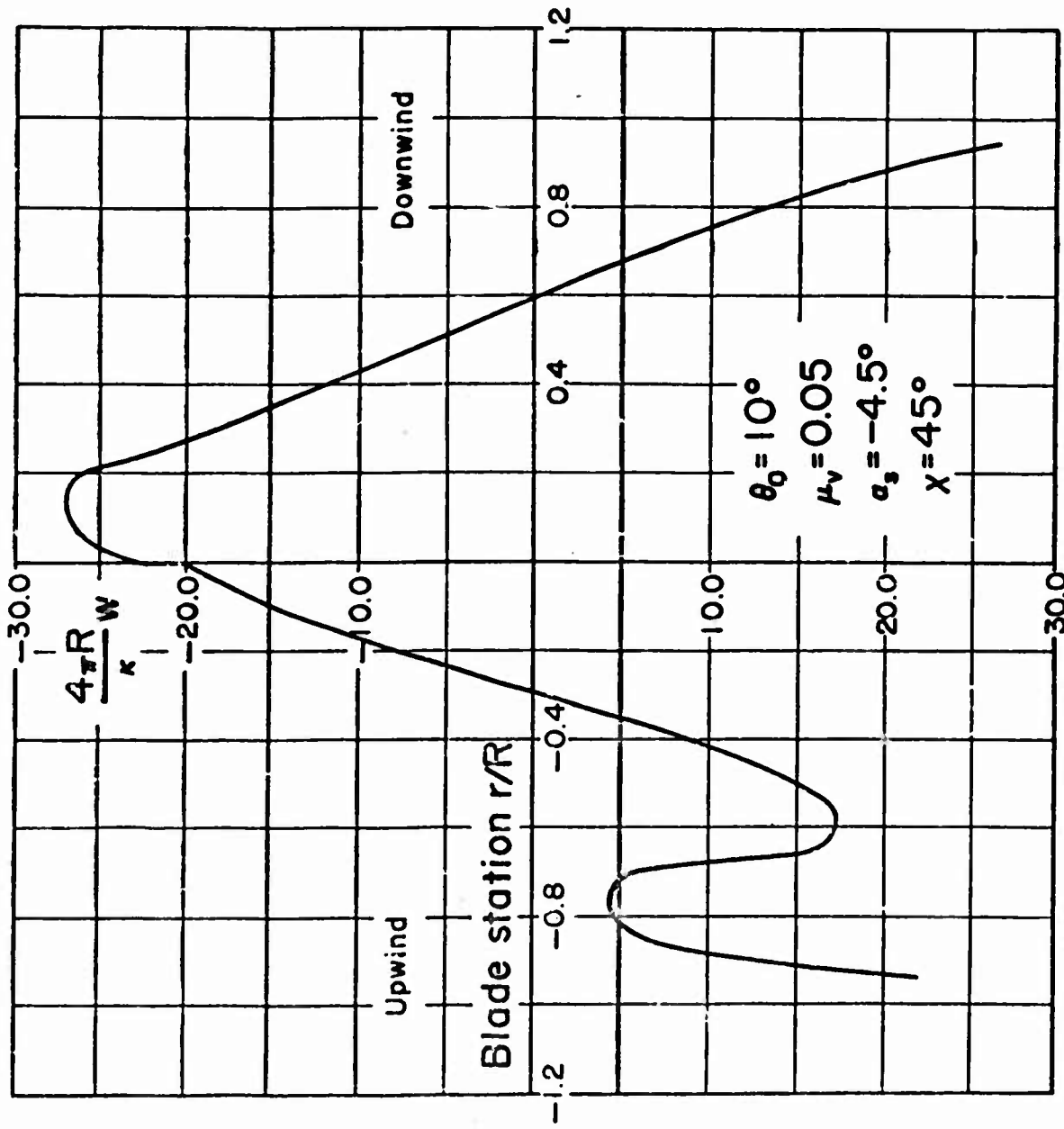


Figure 35. Calculated non-dimensional normal component of induced velocity at the blade feathering axis of a single-bladed rotor assuming that the vortex sheet and the tip vortex move down the wake together. Left side for blade in upwind position; right side, in downwind position.

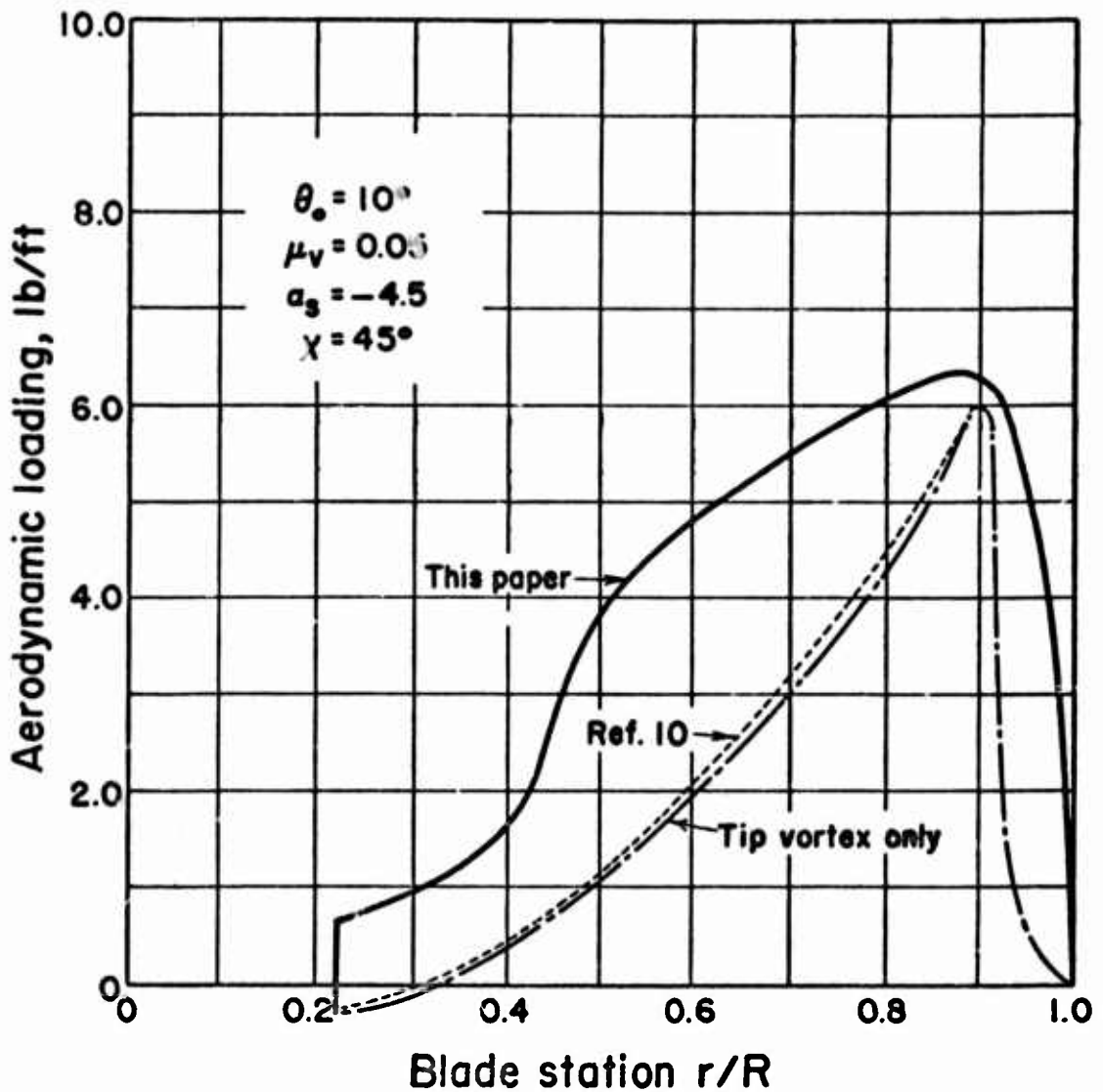


Figure 36. Calculated blade spanwise aerodynamic loading of a single bladed rotor using the induced velocities determined in this paper and in Reference 10 with the blade in the downwind position.

Measured steady state thrust component-----12.1 lbs
 Area under loading curve of this paper-----12.48 lbs
 First harmonic cosine component,
 calculated so that the first harmonic
 flapping moment is zero----- 0.32 lbs

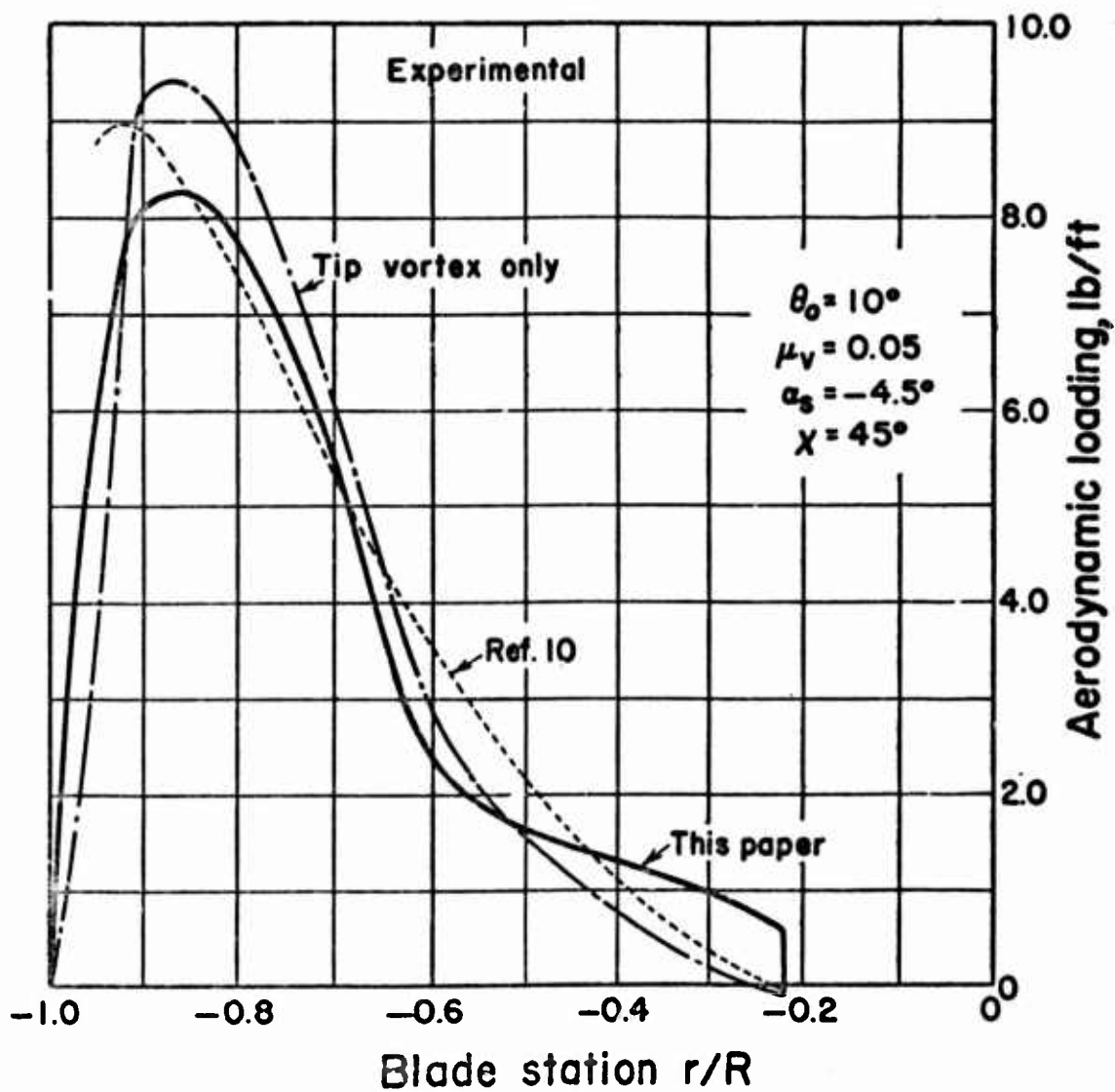


Figure 37. Calculated blade spanwise aerodynamic loading of a single bladed rotor using the induced velocities determined in this paper and in Reference 10 with the blade in the upwind position.

Measured steady state thrust component-----12.1 lbs
 Area under loading curve of this paper-----11.74 lbs
 First harmonic cosine component,
 calculated so that the first harmonic
 flapping moment is zero----- 0.32 lbs

HELICOPTER REPORT DISTRIBUTION LIST

INDUSTRY (One Copy Each)

1. Gyrodyne Corp. of America
2. McDonnell Aircraft Corp.
3. Bell Helicopter Corp.
4. Sikorsky Aircraft Division
United Aircraft Corp.
5. Kaman Aircraft Corp.
6. Kellett Aircraft Corp.
7. Doman Helicopters, Inc.
8. Fairchild Aircraft Division
9. Rotor Craft Corp.
10. Vertol Aircraft Corp.
11. Goodyear Aircraft Corp.
12. Helicopter Division
Hughes Aircraft Company
13. Piasecki Aircraft Corp.
14. Hiller Helicopters
15. Flettner Aircraft Corp.
16. Helicopter Division
Cessna Aircraft Company
17. E. Gluhareff Helicopters Inc.
18. Thieblot Aircraft Co., Inc.
19. Jacobs Aircraft Engine Co.
20. J. B. Rea Co., Inc.
21. Minneapolis-Honeywell
Regulator Co.
Aeronautical Division
22. Aviation Department
Westinghouse Electric Corp.
23. Flight Control Dept., P-32
Sperry Gyroscope Co.
24. Lear Inc.
25. Cornell Aero. Laboratory, Inc.
26. Director, Guggenheim School
of Aeronautics
Georgia Institute of Technology
27. Dept. of Aeronautical Eng.
Massachusetts Institute of
Technology

GOVERNMENT

1. Chief of Naval Research
Wash., D. C., Attn: Code 461
2. ONR Branch Office
New York 13, N. Y.
3. ONR Branch Office
Crerar Library Bldg.
Chicago, Illinois
4. ONR Branch Office
Pasadena 1, California
5. ONR Branch Office
American Embassy, London
6. Director, Naval Research
Laboratory, Wash., D. C.
7. U. S. Naval Training Device
Center, Port Washington, N. Y.
8. Chief, Bureau of Aeronautics
Wash., D. C., Attn: AC-4
9. Chief, Bureau of Aeronautics
Wash., D. C., Attn: AD-322
10. Chief, Bureau of Aeronautics
Wash., D. C., Attn: RS-91
11. Aerodynamics Laboratory
David Taylor Model Basin
Wash., D. C.
- (4) 12. Hq., ARDC, Dt. 1
Wright-Patterson AFB, Ohio (1)
- (1) 13. Comdr., Wright Air Development Center, Attn: WCLBE (1)
- (1) 14. Office Chief of Transportation L/A, Attn: Exec. for R & D (1)
- (1) 15. Office Chief of Transportation D/A, Attn: Army Av. Div. (1)
- (2) 16. CO, TRECUM (2)
- (2) 17. Ft. Eustis, Virginia (1)
- (6) 18. Office Chief R & D, D/A
Wash., D. C., Attn: OCRD/H (1)
- (1) 19. Ft. Monroe, Va., Attn: ATDEV-6 (1)
- (1) 20. President, Army Av. Board Mr6
CONARC, Fort Rucker, Alabama (1)
- (1) 21. Office Secretary of Defense, R&D
Wash., D. C., Attn: Dir. Aero. (1)
- (1) 22. National Advisory Committee for
Aeronautics, Wash., D. C. (1)
- (1) 23. National Advisory Committee for
Aeronautics, LAL, Attn: Fit.Res.Div.
Department of Commerce (1)
- (1) 24. ASTIA, Document Service Center (5)
Knott Bldg., Dayton 2, Ohio

Gray, Robin B.

An Aerodynamic Analysis of a Single-Bladed Rotor in Hovering and Low-Speed Forward Flight as Determined from Smoke Studies of the Vorticity Distribution in the Wake. Princeton University Aeronautical Engineering Department Report No. 356, Sept. 1956 pp 106

1. Rotor blades - load distribution - theoretical analysis.
2. Helicopter models - testing.

I Gray, Robin B. II Princeton University Department of Aeronautical Engineering Report No. 356.

Gray, Robin B.

An Aerodynamic Analysis of a Single-Bladed Rotor in Hovering and Low-Speed Forward Flight as Determined from Smoke Studies of the Vorticity Distribution in the Wake. Princeton University Aeronautical Engineering Department Report No. 356, Sept. 1956 pp 106

1. Rotor blades - load distribution - theoretical analysis.
2. Helicopter models - testing.

I Gray, Robin B. II Princeton University Department of Aeronautical Engineering Report No. 356.

Gray, Robin B.

An Aerodynamic Analysis of a Single-Bladed Rotor in Hovering and Low-Speed Forward Flight as Determined from Smoke Studies of the Vorticity Distribution in the Wake. Princeton University Aeronautical Engineering Department Report No. 356, Sept. 1956 pp 106

1. Rotor blades - load distribution - theoretical analysis.
2. Helicopter models - testing.

I Gray, Robin B. II Princeton University Department of Aeronautical Engineering Report No. 356.

Gray, Robin B.

An Aerodynamic Analysis of a Single-Bladed Rotor in Hovering and Low-Speed Forward Flight as Determined from Smoke Studies of the Vorticity Distribution in the Wake. Princeton University Aeronautical Engineering Department Report No. 356, Sept. 1956 pp 106

1. Rotor blades - load distribution - theoretical analysis.
2. Helicopter models - testing.

I Gray, Robin B. II Princeton University Department of Aeronautical Engineering Report No. 356.

An Aerodynamic Analysis of a Single-Bladed Rotor in Hovering and Low-Speed Forward Flight as Determined from Smoke Studies of the Vorticity Distribution in the Wake. Princeton University Aeronautical Engineering Department Report No. 356, Sept. 1956 pp 106

1. Rotor blades - load distribution - theoretical analysis.
2. Helicopter models - testing.

I Gray, Robin B. II Princeton University Department of Aeronautical Engineering Report No. 356.